CZECH TECHNICAL UNIVERSITY IN PRAGUE
Faculty of Nuclear Sciences and Physical Engineering
Department of Physics

Diploma thesis

High Harmonic Generation by an Elliptically Polarized IR-Radiation on Atomic and Molecular Targets

Jan Vábek

Supervisors: Ing. Jaroslav Nejdl, Ph.D.
Ing. Fabrice Catoire, Ph.D.

Praha, 2017

ČESKÉ VYSOKÉ UČENÍ TECHNICKÉ V PRAZE
FAKULTA JADERNÁ A FYZIKÁLNĚ INŽENÝRSKÁ
PRAHA 1 - STARÉ MĚSTO, BŘEHOVÁ 7 - PSČ 115 19

Katedra: fyziky *Akademický rok:* 2015/16

ZADÁNÍ DIPLOMOVÉ PRÁCE

Posluchač: Bc. Jan Vábek

Obor: Matematická fyzika

Název práce: Generace vysokých harmonických frekvencí prudukovaných elipticky polarizovaným IR zářením na atomárních a molekulárních terčích

Název práce (anglicky): High Harmonic Generation by an Elliptically Polarized IR-Radiation on Atomic and Molecular Targets

Osnova:

Model aproximace silného pole bude použit k simulaci interakce elipticky polarizovaného IR záření s komplexními terči.

Studium vlastností (polarizace, prostorová distribuce) vzniklého záření v závislosti na vlastnostech budícího pole a terče.

Implementace v jazyku FORTRAN.

Práce bude vypracována v anglickém jazyce.

Doporučená literatura:

[1] Catoire, F., Ferré, A., Hort, O., Quintard, L., Descamp, D., Petit, S., Fabre, B., Pons, B., Mével, E., Mairrese, Y. and Constant, E.: On the complex structure of spatially resolved High Order Harmonic spectra [Manuscript in preparation]

[2] Lewenstein, M., Balcou, Ph., Ivanov, M. Yu., L'Huillier, A. and Corkum, P. B.: Theory of high-harmonic generation by low-frequency laser fields; Phys. Rev. A 49, 2117, (1994)

[3] Gaarde, M. B., Tate , J. L., Schafer, K. J.: Macroscopic aspects of attosecond pulse generation; Journal of Physics B, 41, 132001, (2008)

[4] L'Huillier, A., Balcou, Ph., Candel, S., Schafer, K. J. and Kulander, K. C.: Calculations of high-order harmonic-generation processes in xenon at 1064 nm, Phys. Rev. A 46, 2778 (1992)

Jméno a pracoviště vedoucího diplomové práce:

Ing. Jaroslav Nejdl, Ph.D., Fyzikální ústav, AV ČR, v.v.i.

Součástí zadání diplomové práce je její uložení na webové stránky katedry fyziky a zaslání abstraktu a klíčových slov ve formátu WORD na e-mailovou adresu katedry fyziky: kf@fjfi.cvut.cz

Datum zadání diplomové práce: 26.02.2016

Termín odevzdání diplomové práce: 06.01.2017

.....
vedoucí katedry

ČESKÉ VYSOKÉ UČENÍ TECHNICKÉ V PRAZE
Fakulta jaderná a fyzikálně inženýrská
-1-

.....
děkan

V Praze dne 26.02.2016

Policy and Procedures for the supervision of student projects at the Faculty of Nuclear Sciences and Physical Engineering of the Czech Technical University in Prague for the students entering the international exchange programmes

Recognizing the benefits to be gained through the international exchange programmes guaranteed by the Czech Technical University in Prague, the below mentioned rules and procedures specify the details of the student project accomplishment abroad in case they are defined and subject to the accredited curricula at the Faculty of Nuclear Sciences and Physical Engineering of the Czech Technical University in Prague ("Faculty" below).

1. OBJECTIVES

This document relates to:

1.1. The supervision of the two-semester bachelor degree project defined and subject to the accredited bachelor degree curricula at the Faculty of Nuclear Sciences and Physical Engineering of the Czech Technical University in Prague in case when the student wishes to accomplish it partially or entirely during his stay within the international exchange programmes guaranteed by the Czech Technical University in Prague.

1.2. The supervision of the two-semester research project defined and subject to the accredited master degree curricula at the Faculty of Nuclear Sciences and Physical Engineering of the Czech Technical University in Prague in case when the student wishes to accomplish is partially or entirely during his stay within the international exchange programmes guaranteed by the Czech Technical University in Prague.

1.3. The supervision of the two-semester diploma degree project defined and subject to the accredited master degree curricula at the Faculty of Nuclear Sciences and Physical Engineering of the Czech Technical University in Prague in case when the student wishes to accomplish is partially or entirely during his stay within the international exchange programmes guaranteed by the Czech Technical University in Prague.

2. IMPLEMENTATION

2.1. This document follows the rules given by the Study and Examination Code for Students of the Czech Technical University in Prague, Policies and Procedures for the Bachelor and Master Courses at the Faculty of Nuclear Sciences and Physical Engineering of the Czech Technical University in Prague as well as by the Czech Law.

2.2. The supervisors for the projects described in paragraphs 1.1, 1.2, 1.3 are appointed by the Faculty in agreement with the principles of the accredited study programme.

2.3. In case the student wishes to accomplish one of projects listed in Section 1 partially or entirely during his stay within the international exchange programmes guaranteed by the Czech Technical University in Prague, a local co-supervisor at the host university must be found.

2.4 The local co-supervisor at the host university must be approved by the corresponding department and supervisor at the Faculty.

2.5 The local co-supervisor at the host university must be informed about the rules and workflow of the supervision applied at the Faculty. This information is provided by the supervisor at the Faculty.

2.6 The assignment of the student projects listed in Section 1 is issued according to the Policies and Procedures for the Bachelor and Master Courses at the Faculty of Nuclear Sciences and Physical Engineering of the Czech Technical University in Prague. The contents of this assignment written in English makes the attachment of this document.

2.7 The supervisor at the Faculty and the local co-supervisor at the host university together are responsible for maintaining the level of supervision required by the accredited study programme of the Faculty.

2.8 After each semester of the stay within the exchange programme, the local co-supervisor at the host university issues a written report on how the student fulfilled the project assignment issued by the Faculty. This report serves for the crediting of the student project after the student returns from abroad.

2.9 The student project defined in Section 1 is always presented and defended at the Faculty in the way given by the Policies and Procedures for the Bachelor and Master Courses at the Faculty of Nuclear Sciences and Physical Engineering of the Czech Technical University in Prague.

2.10 All particularities and complementary issues given by the specifics of the exchange programmes are handled by the decision of the Faculty dean.

	Ing. J. Nejdl, Ph. D. (Project Supervisor)
Department Head Faculty of Nuclear Sciences And Physical Engineering	
Date	Date
Co-supervisor Host University	Faculty vice-dean
Date 18/02/2016	Date

Attachment: The contents of the planned assignment of the student project.

Attachment:

The contents of the planned assignment of the student diploma degree project:

- Strong field approximation model will be used to simulate the intercation of an elliptically polarized IR radiation with complex targets
- Study of the generated-radiation properties (polarization, spatial distribution) as a function of the fundamental radiation properties and target
- Implementation in FORTRAN

In particular we would like to focus on the study of HHG when an elliptical IR radiation interacts with complex targets. This analysis will help in understanding all the optical properties of HHG such as polarization, energy range, coherence etc. which can then be used for experiments. To that purpose we will account for the individual atomic and molecular responses and include the propagation of the Harmonics through the medium by taking into account all the dimensionality of the problem.

Prohlášení:

Prohlašuji, že jsem svou diplomovou práci vypracoval samostatně a použil jsem pouze podklady (literaturu, software, atd.) uvedené v přiloženém seznamu.

Nemám závažný důvod proti použití tohoto školního díla ve smyslu § 60 Zákona č. 121/2000 Sb., o právu autorském, o právech souvisejících s právem autorským a o změně některých zákonů (autorský zákon).

V Praze dne 5. 5. 2017

Title: **High Harmonic Generation by an Elliptically Polarized IR-Radiation on Atomic and Molecular Targets**

Author: Jan Vábek

Specialization: Mathematical physics

Sort of project: Diploma thesis

Supervisor: Ing. Jaroslav Nejdl, Ph.D.

Co-Supervisor: Ing. Fabrice Catoire, Ph.D.

Abstract: The aim of the master thesis is to provide a theoretical study of the XUV-radiation production based on the High Harmonic Generation (HHG) in gaseous media. It focuses on two aspects: 1–temporal control using the so-called polarisation gating technique in order to reduce the pulse duration and control the spectral properties of the generated XUV and 2–studying the spatial distribution of the XUV in order to confine spatially the XUV pulse. First, the theory of HHG is explained. Concerning the temporal control, the highest XUV-photon energy under the polarisation gating is analysed and we show an extend of the cut-off as compared to the linear case. Then, we have simulated the case where two delayed counter-rotating elliptical pulses of different amplitudes are used and we demonstrate, for the first time, that it allows for controlling the XUV-photon frequency. The spatial distribution analysis of the harmonic spectra is motivated by recent experimental observations. We have developed a model for simulating spatially resolved XUV generation in thin media. In these simulations, several microscopic response models (starting with a simple microscopic phenomenological dipole up to a fully quantum description) have been accounted showing qualitative agreement with experiments. Both aspects of HHG are essential for providing a realistic model and their common output may provide a powerful and robust tool requested for the design of experiments and also for their physical interpretation.

Key words: High Harmonic Generation in Gases, Polarisation Gating, Strong Field Approximation, Spatially Resolved Harmonic Spectra

Název práce: **Generace vysokých harmonických frekvencí produkovaných elipticky polarizovaným IR zářením na atomárních a molekulárních terčích**

Autor: Jan Vábek

Obor: Matematická fyzika
Druh práce: Diplomová práce

Vedoucí práce: Ing. Jaroslav Nejdl, Ph.D.; Fyzikální ústav AV ČR, v. v. i./ ELI Beamlines

Konzultant: Ing. Fabrice Catoire, Ph.D.; laboratoř CELIA, Bordeaux

Abstrakt: Tato diplomová práce se zabývá teoretickým studiem produkce XUV záření založeném na principu generace vysokých harmonických frekvencí (HHG) v plynném médiu. Zaměřujeme se na dva aspekty: 1–kontrola časového průběhu generovaného záření pomocí tzv. polarizačního klíčování (v originále *polarisation gating*) za účelem zkrácení generovaných pulsů a kontrole jejich spektrálních vlastností; 2–prostorová distribuce XUV záření za účelem snížení prostorové divergence XUV svazku a zvýšením jeho maximální intenzity. V první části shrnujeme teorii HHG, v části o polarizačním klíčováním se zabýváme maximální možnou generovanou frekvencí a dále jsme poprvé ukázali metodu kontroly generovaných frekvencí pomocí použití impulzů s odlišnou maximální intenzitou v polarizačním klíčování. Studium prostorové distribuce je motivováno nedávnými experimentáními pozorováními. Vyvinuli jsme model pro simulaci prostorového rozložení XUV záření generovaného v tenkých terčích. V tomto modelu jsme použili a diskutovali různé modely mikroskopické odezvy (počínaje fenomenologickým dipólem až k plně kvantověmechanickému řešení) a dosáhli jsme kvalitativní shody s experimenty. Oba výše zmíněné aspekty HHG jsou klíčové k vytvoření realistického modelu HHG a jejich společný výstup může poskytnout nástroj pro návrh a fyzikální interpretaci experimentů.

Klíčová slova: generace vysokých harmonických v plynech, polarizační klíčování, aproximace silného pole, prostorové rozložení harmonického spektra

Titre: **Génération d'harmoniques d'ordre élevé utilisant rayonement infra-red avec une polarisation elliptique sur les cibles moléculaires et atomiques**

Auteur: Jan Vábek

Spécialisation: Physique mathématique

Le type du project: Mémoire de master

Superviseur: Ing. Jaroslav Nejdl, Ph.D.

Co-Superviseur: Ing. Fabrice Catoire, Ph.D.

Résumé: L'objectif de cette mémoire de master est de faire une étude théorique du mécanisme à l'origine de la production de rayonnement XUV sous forme d'harmoniques d'ordre élevé (HHG) dans les milieux gazeux interagissant avec un champ laser IR intense. Deux aspects sont étudiés : 1–la contrôle temporelle à l'aide de la technique ≪optical gating≫ qui permet de réduire la durée et de controler les propriétés spectrales des impulsions XUV et 2–la contrôle spatial pour confiner les impulsions XUV. En premier lieu, la théorie général d'HHG est expliquée. Dans le cadre du contrôle temporel, l'énergie maximale du photon XUV obtenu par optical gating est analysée et nous avons étudié l'évolution de la gamme spectrale comparé au cas de la théorie pour un champ polarisé linéairement. Ensuite, nous avons simulé les cas de deux impulsions IR retardées temporellement polarisées elliptiquement (respectivement droite et gauche) et d'amplitude différente. Nous avons montré, pour la premier fois, que cette approche permet le contrôle de la fréquence centrale du peigne de fréquence XUV. L'analyse de la distribution spatiale du spectre harmonique est motivée par les observations expérimentales récentes. Nous avons ensuite développé un modèle pour la simulation de la distribution spatiale du spectre XUV généré dans un milieu mince. Ces différents modèles ont été employés pour différents dipôles microscopiques en commençant par un dipôle basé sur une approche phénoménologique jusqu'à la description complètement quantique. Un bon accord entre simulations et expériences a été obtenu. Les deux aspects présentés sont essentiels pour fournir un modèle réaliste et les conclusions qui en ressortent nous permettent de créer un instrument théorique puissant et robuste nécessaire à l'interprétation des résultats expérimentaux et comme guide pour de futures expériences.

Mots clés: la génération d'harmoniques d'ordre élevé dans les gaz, polarisation gating, approximation du champ fort, spectre harmonique spatialement résolu

Acknowledgement

I would like to express my gratefulness to the CELIA staff where I was able of being a member of the HHG group during my internship, especially to my French supervisor Fabrice Catoire, who has provided me a great support and who allowed me to gain a deep understanding of the topic. As well, I would like thank my Czech supervisor Jaroslav Nejdl for valuable consultations and the support during both my stay abroad and the time spent at ELI. Next, the support from the Erasmus+ exchange programme and from my family who needs to be mentioned, because the part of the work done abroad could have not been realized without them.

This work was supported by the Grant Agency of the Czech Technical University in Prague, grant No. SGS16/239/OHK4/3T/14. Computing hours for running simulations were graciously provided by the MCIA Avakas cluster and the CELIA laboratory.

CONTENTS

LIST OF FIGURES

1. INTRODUCTION

High-order Harmonic Generation (HHG) is a source of radiation, in the UV-XUV range, that is becoming more and more popular. In particular it is a source that can produce ultra-short pulses (down to 67 as [1]) and also gives an access to the structure of the target by the so called tomography technique [2]. The experimental conditions for obtaining such properties require a precise temporal and frequency control of the generation.[1] Despite the considerable outcome of HHG, the efficiency of the process is quite low and it is still challenging to use it for probing non-linear processes such as two photon single or double ionization. A lot of efforts have been dedicated to the improvement of the fluence of HHG by discarding reflecting mirrors on the path of the XUV beam for example.

The HHG is the result of the interaction of an Infra-Red (IR) laser pulse with an atom and it can be described as follows: 1 – first ionization occurs and a portion of the electronic wave packet is released in the continuum 2 – the resulting wave packet gains kinetic energy in the presence of the oscillating laser 3 – part of the wave packet has a probability to return to in the vicinity of the nucleus and to recombine emitting a photon linked to the energy surplus gained in the IR laser. A semi-classical model has been introduced in the 90's [3, 4] in order to explain this process. Nowadays techniques that can solve outlined problems (the control of the XUV-beam intensity and temporal-frequency properties) are: i – A way of controlling the intensity of the HHG beam is to control the diameter of the XUV beam so that by reducing it keeping its total energy conserved, the intensity will be automatically increased. In the far field region, the problem reduces only to the control of the divergence of that beam. ii – Regarding the temporal-control problem, a trending topic is the generation by the mixing of more than one pulse, because it allows for a precise control of the IR-field in the moment of the XUV-field generation. This technique is called *the polarisation gating* when the two pulses with a common fundamental frequency are used.

Referring to these two aspects, this work shows that controlling the IR-pulses-temporal profile allows for the temporal and frequency control of the XUV and a way of controlling the fluence of the HHG beam is to control the focus point of this beam. The aim of that master thesis is to study theoretically how to effectively reduce the divergence of a given harmonic and how to control the time and frequency properties of the generated harmonics. Both is reached by controlling the IR-field-driven generation process.

The study is based on numerical simulations implementing derived theory. All the simulations are performed numerically using codes written in FORTRAN90. The simulations can be split in two aspects: i — The point of view of a single microscopic target is described, this is the microscopic model, the calculated dipole is then computed. ii – The whole macroscopic medium is treated as an assembly of microscopic emitters and their radiation is then coherently summed in order to obtain the output field.

This manuscript is organized as follows: 1 – First, the theory for calculating the HHG for a single microscopic target is described. These calculations are realised assuming that the target can be described in the *Single active electron approximation (SAE)*, namely the single electron is accounted and plunged in an average potential taking into account the presence of the nucleus and the other electrons. This theory is then applied to atomic targets and illustrated by examples. 2 – A special configuration of the IR-field, the so-called *polarisation gating*, based on a composition of two counter-rotating elliptical IR-pulses is studied from the general point of view. The general theory is then used for studying the temporal and frequency properties of the generated XUV-radiation. 3 – The spatial distribution of a harmonic field generated in a thin target is resolved in the far-field region. 4 – The results of the work are summarised and they are placed in a more broader present-day context of HHG physics. 5 – These main parts of the work are followed

[1] Time and frequency domains being Fourier-transform related, a control in time also means a control in frequency and vice-versa.

by the bibliography and several appendices explaining used conventions and mathematical tools in greater details.

The XUV-spatial-control part of the work is performed in a close relation with experiments that have been performed in the XUV-HHG group at CELIA on this topic by a Ph.D. student Ludovic Quintard under the supervision of Eric Constant. Experimentalists have measured spatially resolved harmonics spectra collected at 3 meters away from the gas jet. A far-field description of the experiments is then in principle correct. In this work, we will try to interpret the experimental results obtained in order to give more insight to the physics.

The atomic and SI units are used through all the work. The conventions for the Fourier transform is explained in Appendix A. All the simulations were made for an 800-nm laser ($\omega_0 = 0.057$ a.u.).

2. GENERAL THEORY OF SINGLE EMITTER RESPONSE–MICROSCOPIC MODEL

The problem to solve is formulated in the introduction above. The UV-XUV radiation is produced during the interaction of the single microscopic target (an atom or a molecule) with the intense external IR-field. This chapter gives the mathematical description of the process leading to the induced microscopic dipole. The generated radiation is then find using the dipole radiation. Most of the HHG features can be explained using only a single active electron picture. Only the active electron interacts with the field while the rest of the target stays unchanged. The Hamiltonian of the system under consideration is then split into two parts

$$\hat{H}(t) = \hat{H}_0 + \hat{V}_{\boldsymbol{\mathcal{E}}}(t)\,, \qquad\qquad \hat{H}_0 = \frac{\hat{\boldsymbol{p}}^2}{2} + \hat{V}_C\,. \tag{2.1}$$

$\hat{H}_0$ is the field-free Hamiltonian where $\hat{V}_C$ is the operator describing the interaction of one electron with nuclei and the other electrons of the target. It is not influenced by the external field in our model. The external-field interaction operator is given by $\hat{V}_{\boldsymbol{\mathcal{E}}}(t) = \boldsymbol{\mathcal{E}}(t)\cdot\hat{\boldsymbol{r}}$ in the length gauge, where the dipole approximation has been used.[1] In the case of the Hydrogen atom, $V_C(\boldsymbol{r}) = -\frac{1}{r}$. In the two next section, an approximate solution of the time-dependent Schrödinger equation (TDSE) will be retrieved and used for calculating the harmonic spectra.

2.1 HHG in the Strong Field Approximation

In order to solve the TDSE

$$\mathbf{i}\partial_t\,|\psi(t)\rangle = \hat{H}(t)\,|\psi(t)\rangle\ , \tag{2.2}$$

the following ansatz [2]

$$|\psi(t)\rangle = \mathrm{e}^{-\mathbf{i}E_g t}\left(|g\rangle + \int \mathrm{d}^3p\; b(\boldsymbol{p},t)\,|\boldsymbol{p}\rangle\right)\,, \qquad\qquad b(\boldsymbol{p},0) = 0\,, \tag{2.3}$$

is used as introduced for the first time by Lewenstein [4]. $|g\rangle$ is the ground state of $\hat{H}_0$, E_g is the lowest eigenenergy of the Hamiltonian under our consideration and the second term of the wave function is an expansion of the continuum part on plane waves $|\boldsymbol{p}\rangle$. Introducing Eq. (2.3) into Eq. (2.2) leads to

$$\mathbf{i}\partial_t b(\boldsymbol{p},t) = \int \mathrm{d}^3p'\; b(\boldsymbol{p}',t)\,\langle\boldsymbol{p}'|\hat{H}_0|\boldsymbol{p}\rangle + \boldsymbol{\mathcal{E}}(t)\cdot\boldsymbol{d}(\boldsymbol{p}) + \boldsymbol{\mathcal{E}}(t)\int \mathrm{d}^3p'\; b(\boldsymbol{p}',t)\,\langle\boldsymbol{p}'|\hat{\boldsymbol{r}}|\boldsymbol{p}\rangle - E_g b(\boldsymbol{p},t)\,, \tag{2.4}$$

where $\boldsymbol{d}(\boldsymbol{p}) = \langle\boldsymbol{p}|\hat{\boldsymbol{r}}|g\rangle$ is the *dipole-transition-matrix element* between the continuum state $|\boldsymbol{p}\rangle$ and the ground state $|g\rangle$. $\boldsymbol{d}(\boldsymbol{p}) = \langle\boldsymbol{p}|\hat{\boldsymbol{r}}|g\rangle$ is the p-representation of $\hat{\boldsymbol{r}}\,|g\rangle$. Thus,

$$\boldsymbol{d}(\boldsymbol{p}) = \mathbf{i}\bigtriangledown_{\boldsymbol{p}}\,\tilde{\psi}_g(\boldsymbol{p})\,, \tag{2.5}$$

where $\tilde{\psi}_g(\boldsymbol{p})$ is the ground-state eigenfunction in the p-representation (see Appendices A.2 and B.5 for details about different representations). As an example for the Hydrogen atom, the ground state is $\langle\boldsymbol{r}|100\rangle =$

[1] The dipole approximation uses only the value of the external field at the position of the nucleus. This is valid if the wavelength of the field is much larger than the area of the motion of the electron.

[2] A problem from the theoretical point of view is that this ansatz violates the wave-function-norm conservation. However for little ionization, the norm approximately remains all the time.

$2\mathrm{e}^{-r}\,Y_0^0\,(\Omega_{\boldsymbol{r}})$. The change of the representation gives $\langle \boldsymbol{p}|100\rangle = \frac{2\sqrt{2}}{\pi}\frac{1}{(1+p^2)^2}$ and its gradient leads to the final result

$$\boldsymbol{d}(\boldsymbol{p}) = -\mathbf{i}\frac{8\sqrt{2}}{\pi}\frac{\boldsymbol{p}}{(1+p^2)^3}\,, \tag{2.6}$$

further details about the matrix elements are in Appendix B.6. Using the previous remarks, $\langle \boldsymbol{p}' \,|\, \hat{\boldsymbol{r}} \,|\, \boldsymbol{p}\rangle$ can be analytically calculated and becomes $\mathbf{i} \bigtriangledown_{\boldsymbol{p}} \delta(\boldsymbol{p}-\boldsymbol{p}')$, where $\langle \boldsymbol{p}|\boldsymbol{p}'\rangle = \delta(\boldsymbol{p}-\boldsymbol{p}')$ has been used. Calculating the matrix element of the kinetic component of the field-free Hamiltonian leads to a similar expression. On the other hand, calculating $\langle \boldsymbol{p}'|\hat{V}_C|\boldsymbol{p}\rangle$ does not present any difficulties but it leads to a non-local term. From the physical point of view this term represents the free-free transitions induced by the Coulomb potential, or in other words a re-scattering term that is known to be negligible [4]. That is the reason why this term will be discarded in this work. Equation (2.2) is now reduced to

$$\mathbf{i}\partial_t \tilde{b}(\boldsymbol{k},t) = \left(\frac{(\boldsymbol{k}+\boldsymbol{A}(t))^2}{2} - E_g\right)\tilde{b}(\boldsymbol{k},t) + \boldsymbol{\mathcal{E}}(t)\cdot\boldsymbol{d}(\boldsymbol{k}+\boldsymbol{A}(t))\,, \tag{2.7}$$

where the change of variables $\boldsymbol{k} = \boldsymbol{p} - \boldsymbol{A}(t)$, $\tilde{b}(\boldsymbol{k},t) = b(\boldsymbol{k}+\boldsymbol{A}(t),t)$ has been used. The electric field $\boldsymbol{\mathcal{E}}(t)$ and the vector potential $\boldsymbol{A}(t)$ are related by the equation $\boldsymbol{\mathcal{E}}(t) = -\partial_t \boldsymbol{A}(t)$. Using the boundary condition Eq. (2.3), the solution of Eq. (2.7) is

$$b(\boldsymbol{p},t) = -\mathbf{i}\int_0^t \left(\boldsymbol{\mathcal{E}}(t)\cdot\boldsymbol{d}(\boldsymbol{q}_{t,t'})\right)\mathrm{e}^{-\mathbf{i}\int_{t'}^t\left(\frac{\boldsymbol{q}_{t,t''}^2}{2}-E_g\right)\mathrm{d}t''}\,\mathrm{d}t'\,, \qquad \boldsymbol{q}_{t,t'} = \boldsymbol{p}+\boldsymbol{A}(t')-\boldsymbol{A}(t)\,. \tag{2.8}$$

Knowing the wave function $|\psi(t)\rangle$, one can obtain the dipole $\boldsymbol{d}(t) = -\langle\psi(t)|\hat{\boldsymbol{r}}|\psi(t)\rangle$.[3] Three terms can be distinguished in the expression of the dipole. The first one is $\langle g|\hat{\boldsymbol{r}}|g\rangle$ that is zero for symmetry reasons. A second one contains $\langle \boldsymbol{p}'|\hat{\boldsymbol{r}}|\boldsymbol{p}\rangle$ (primed variables are used in the expansion of $\langle\psi(t)|$, see Eq. (2.3)) that can be neglected since it corresponds to a next free-free contribution in the dipole and is known to be small [5]. The remaining part is responsible for the HHG and it is given by

$$\int \mathrm{d}^3p\; b(\boldsymbol{p},t)\,\langle g|\hat{\boldsymbol{r}}|\boldsymbol{p}\rangle = \mathbf{i}\int_0^t \mathrm{d}t'\int \mathrm{d}^3k\;\left[\boldsymbol{\mathcal{E}}(t')\cdot\boldsymbol{d}(\boldsymbol{k}+\boldsymbol{A}(t'))\mathrm{e}^{-\mathbf{i}\mathcal{S}(t',t,\boldsymbol{k})}\right]\boldsymbol{d}^*(\boldsymbol{k}+\boldsymbol{A}(t))\,, \tag{2.9}$$

$$\mathcal{S}(t',t,\boldsymbol{k}) = \int_{t'}^t\left(\frac{(\boldsymbol{k}+\boldsymbol{A}(t''))^2}{2} - E_g\right)\mathrm{d}t''\,. \tag{2.10}$$

The dipole can be written in a closed form both in the time and frequency domain,

$$\boldsymbol{d}(t) = -\mathbf{i}\int_0^t \mathrm{d}t'\int_{\mathbb{R}^3}\mathrm{d}^3k\;\left[\boldsymbol{\mathcal{E}}(t')\cdot\boldsymbol{d}(\boldsymbol{k}+\boldsymbol{A}(t'))\mathrm{e}^{-\mathbf{i}\mathcal{S}(t',t,\boldsymbol{k})}\right]\boldsymbol{d}^*(\boldsymbol{k}+\boldsymbol{A}(t)) + \mathsf{c.c.}\,, \tag{2.11}$$

$$\tilde{\boldsymbol{d}}(\omega) = -\frac{\mathbf{i}}{\sqrt{2\pi}}\int_{-\infty}^{+\infty}\left(\int_0^t \mathrm{d}t'\int \mathrm{d}^3k\;\left[\boldsymbol{\mathcal{E}}(t')\cdot\boldsymbol{d}(\boldsymbol{k}+\boldsymbol{A}(t'))\mathrm{e}^{\mathbf{i}\left(\omega t-\mathcal{S}(t',t,\boldsymbol{k})\right)}\right]\boldsymbol{d}^*(\boldsymbol{k}+\boldsymbol{A}(t))\right)\mathrm{d}t + \mathsf{c.c.}\,. \tag{2.12}$$

2.2 General properties of HHG and its spectra

Based on the previous solution,[4] the mechanism of HHG can be understood from a simple qualitative analysis, that is called the three step model. In the first step, the electron is liberated from the atom. It

[3] The correspondence between the expected value obtained from the QM and classical result is supposed. This problem is little bit subtle, especially because the generated field is given by its second derivative. However, the results from our choice are sufficient for the purposes of this work.

[4] This model can be also seen from the purely classical point of view [3]. However, this theory does not predict the probability of ionization as a function of time.

propagates during the second step and due to the periodicity of the field, it returns back to the parent ion accumulating kinetic energy from the field. In the last step, the electron recombines back and the gained energy is emitted in the form of photons. The emitted radiation is exactly what we are looking for. The physical interpretations of the quantum description will be discussed in the following sections.

An energy balance in the three step model allows to find the maximal photon energy E_{cutoff} that can be reached by this process [3]

$$E_{\text{cutoff}} \approx 3.2\, U_p + I_P\,, \qquad U_p = \frac{I_{\text{IR}}}{4\omega_0^2}\,, \tag{2.13}$$

I_{IR} is the intensity of the IR-field, ω_0 its frequency and I_P is the ionization potential of the target.[5] For energies $E < E_{\text{cutoff}}$, there are two possible electron trajectories that produce a photon corresponding to the same produced-photon energy E. They are called *short-* and *long-trajectories* according to the time spent in the continuum. However this model does not predict the probability of ionization as a function of time.

Next, we can examine the HHG spectra that is given by the modulus of Eq. (2.12). A typical HHG spectrum is shown in Fig. 2.1. Three main regions can be distinguished, for the energies below I_p when the generation is described by perturbation theory. It is followed by the plateau, where the response is almost constant, up to the cut-off. Above the cut-off, the dipole yield exponentially decreases with frequency.

A next notable issue is the order of generated harmonics. Using a simple analysis of a XUV-field generated by an infinite fundamental field with a period T_0. The generated dipole is periodic and also it has the opposite sign in the second half-cycle than in the first one, i.e. $d(t+T_0) = d(t)$ and $d\left(t+\frac{T_0}{2}\right) = -d(t)$. If one expands the dipole in the Fourier basis

$$d(t) = \sum_{k\in\mathbb{Z}} a_k \mathrm{e}^{\mathrm{i}\frac{2\pi k t}{T_0}}\,, \tag{2.14}$$

[5] $I_P = -E_g$, both quantities are used, I_P has a clear meaning as the energy that is required for ionizing the target while E_g is the eigenenergy in the quantum formalism.

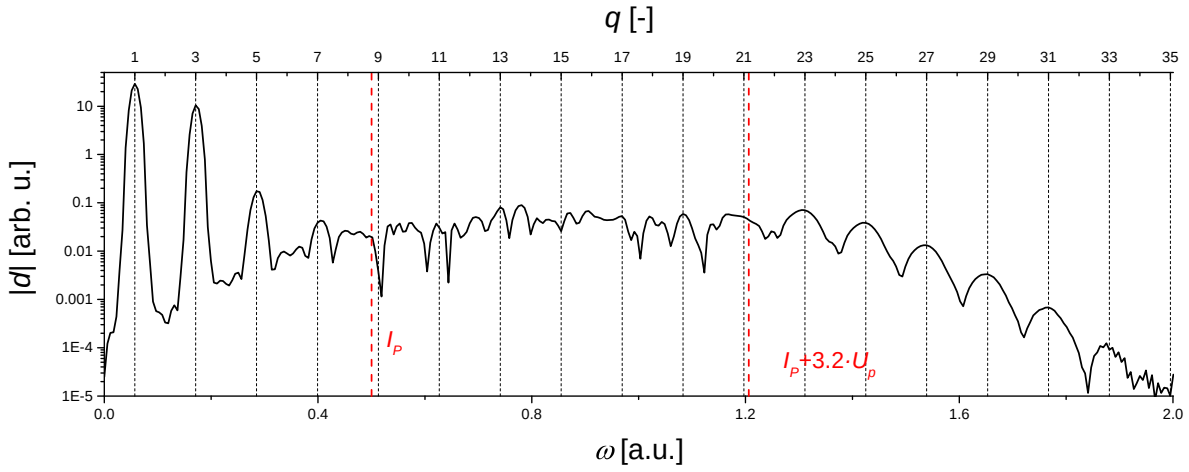

Fig. 2.1: A typical spectrum of high harmonics generated in a gas. This result is obtained from a simulation based on the results from the section 2.3.1. A Hydrogen atom has been used was used as a target with the transition dipole element (2.6), the peak-electric-field amplitude was $\mathcal{E}_0 = 0.053$ a.u. (10^{14} W $\cdot$ cm^{-2}).

the even coefficients, $a_{2\mathbb{Z}+1}$, vanish because

$$a_k = \frac{1}{T_0}\int_0^{T_0} f(t)\mathrm{e}^{-\mathbf{i}\frac{2\pi kt}{T_0}} f(t)\,\mathrm{d}t = \frac{1}{T_0}\left(\int_0^{\frac{T_0}{2}} f(t)\mathrm{e}^{-\mathbf{i}\frac{2\pi kt}{T_0}}\,\mathrm{d}t + \mathrm{e}^{-\mathbf{i}k\pi}\int_0^{\frac{T_0}{2}} f(t)\mathrm{e}^{-\mathbf{i}\frac{2\pi kt}{T_0}}\,\mathrm{d}t\right) = \\ = \frac{\left(1-\mathrm{e}^{-\mathbf{i}k\pi}\right)}{T_0}\int_0^{\frac{T_0}{2}} f(t)\mathrm{e}^{-\mathbf{i}\frac{2\pi kt}{T_0}}\,\mathrm{d}t\,. \quad (2.15)$$

This is fulfilled for a real physical field except in the plateau in Fig. 2.1. The complicated structure in this region is caused by an interference of short- and long-trajectories in an enveloped IR-field.

2.3 The Saddle point approximation

Computing Eqs. (2.11) and (2.12) requires the evaluation of a four- and five-dimensional integral, respectively, which is computationally demanding.

The purpose of this section is to show how to reduce the number of integrals. The general expression of the integrand is a slowly varying function multiplied by a fast-oscillating complex exponential that is cancelling out in average but at specific points where the argument of the exponential is stationary: the so-called *Saddle points*. The evolution of the integrals using the Saddle points is based on the so-called *Method of steepest descents*, [6]. This method will be used firstly only to reduce the k-space integrals and to eliminate all the integrals then.

2.3.1 The Saddle point approximation in k-space (KSPA)

The phases that are under consideration are the arguments of the exponentials defined in Eqs. (2.11) and (2.12), i.e. $-\mathcal{S}(t,t',\boldsymbol{k})$ and $\Phi_\omega(t,t',\boldsymbol{k}) = \omega t - \mathcal{S}(t,t',\boldsymbol{k})$. Considering the integration over momenta, ωt does not play a role and it leads to the following equation for the Saddle points:

$$\bigtriangledown_{\boldsymbol{k}}\Phi_\omega = -\bigtriangledown_{\boldsymbol{k}}\mathcal{S} = 0 \qquad \Rightarrow \qquad \boldsymbol{k}_{t,t'}^{(\mathrm{sp})} = -\frac{\int_{t'}^{t}\boldsymbol{A}(t'')\,\mathrm{d}t''}{(t-t')}\,. \quad (2.16)$$

The remaining integrals over temporal variables are performed numerically. The dipole in the temporal domain is then

$$\boldsymbol{d}(t) = -2\,\mathsf{Re}\;\mathbf{i}\int_0^t\left[\boldsymbol{\mathcal{E}}(t')\cdot\boldsymbol{d}(\boldsymbol{k}_{t,t'}^{(\mathrm{sp})}+\boldsymbol{A}(t'))\left(\frac{-2\pi\mathbf{i}}{(t-t')}\right)^{\frac{3}{2}}\mathrm{e}^{-\mathbf{i}\mathcal{S}(t',t,\boldsymbol{k}_{t,t'}^{(\mathrm{sp})})}\right]\boldsymbol{d}^*(\boldsymbol{k}_{t,t'}^{(\mathrm{sp})}+\boldsymbol{A}(t))\,\mathrm{d}t'\,, \quad (2.17)$$

which is a one-dimensional integral that can be evaluated numerically. The latter formulation will be called KSPA referring to the Saddle points in the k-space. The transformation of the dipole to the frequency domain is $\tilde{d}(\omega) = \mathscr{F}\left[d(t)\right](\omega)$.

A physical interpretation of the equation can be based on the three step model introduced at the beginning of the section 2.2. The variable t' can be seen as the time of the release of the active electron. The integral is then accounting all the contributions of the released electrons to the dipole evaluated in the time t. The terms in the integrand can be assigned to three processes in the three-step model. The ionisation is represented by the term $\boldsymbol{\mathcal{E}}(t')\cdot\boldsymbol{d}(\boldsymbol{k}_{t,t'}^{(\mathrm{sp})}+\boldsymbol{A}(t'))$, the propagation by $\left(\frac{-2\pi\mathbf{i}}{(t-t')}\right)^{\frac{3}{2}}\mathrm{e}^{-\mathbf{i}\mathcal{S}(t',t,\boldsymbol{k}_{t,t'}^{(\mathrm{sp})})}$, where $(t-t')^{-\frac{3}{2}}$ is the spreading of the wave packet, and finally the recombination $\boldsymbol{d}^*(\boldsymbol{k}_{t,t'}^{(\mathrm{sp})}+\boldsymbol{A}(t))$.

2.3.2 The limitations going from the SPA

It seems that there could be a problem when $t'\to t$ because of the term $(t-t')^{-3/2}$. In order to treat the problem, a general statement that

$$\lim_{\varepsilon\to 0}\frac{\frac{\int_0^\varepsilon f(x)\,\mathrm{d}x}{\varepsilon} - f(\xi)}{\varepsilon}\,, \qquad \xi\in\{0,\varepsilon\}\,, \quad (2.18)$$

is finite for a differentiable f is needed. It can be shown elementary. Let us consider $\xi = 0$. The first mean value theorem for definite integrals can be used, i.e. $\exists\alpha \in]0,1[$: $\int_0^\varepsilon f(x)\,\mathrm{d}x = \varepsilon f(\alpha\varepsilon)$. This leads to

$$\lim_{\varepsilon\to 0}\frac{\frac{\int_0^\varepsilon f(x)\,\mathrm{d}x}{\varepsilon} - f(0)}{\varepsilon} = \alpha\lim_{\varepsilon\to 0}\frac{f(\alpha\varepsilon)-f(0)}{\alpha\varepsilon} = \alpha f'(0)\,. \tag{2.19}$$

For a s-type orbital, the divergences are cancelled out by the transition dipole matrix elements, Eq. (2.6). Taking only the component in the direction of the electric field, one finds

$$\frac{d_z(\boldsymbol{k}^{(\mathrm{sp})}_{t,t'}+\boldsymbol{A}(t'))d_z^*(\boldsymbol{k}^{(\mathrm{sp})}_{t,t'}+\boldsymbol{A}(t))}{(t-t')^{\frac{3}{2}}} \sim \sqrt{t-t'}\left(\frac{\frac{\int_{t'}^t A_z(t'')\,\mathrm{d}t''}{t-t'} - A_z(t')}{t-t'}\right)\left(\frac{\frac{\int_{t'}^t A_z(t'')\,\mathrm{d}t''}{t-t'} - A_z(t)}{t-t'}\right)\,. \tag{2.20}$$

This expression is similar to the discussed limit, Eq. (2.18). Exactly the same procedure can be done for the Gaussian model of the ground state from Appendix B.6.2.1. However, the situation is different for a p-orbital. The Saddle Point Approximation can be used in that case either, but an extra treatment has to be done.

2.3.3 Dipole generated by a linear field from the p orbital

For the sake of simplicity, the treatment will start with a p_z-orbital. The corresponding state is

$$\langle\boldsymbol{p}|210\rangle = \tilde{\psi}_{210}(\boldsymbol{p}) = \frac{2^6 p_z}{\pi(1+4p^2)^3}\,. \tag{2.21}$$

The transition-matrix dipole element is then proportional to

$$\frac{\partial\tilde{\psi}_{210}(\boldsymbol{p})}{\partial p_z} = \frac{2^6(1+4p_x^2+4p_y^2-20p_z^2)}{\pi(1+4\boldsymbol{p}^2)^4} \tag{2.22}$$

and the corresponding dipole z-component

$$d_z^{(210)}(t) \propto \int\mathrm{d}t'\int\mathrm{d}^3k\;\mathcal{E}(t')\frac{\partial\tilde{\psi}_{210}(\boldsymbol{k}+\boldsymbol{A}(t'))}{\partial p_z}\mathrm{e}^{-\mathbf{i}\mathcal{S}(\boldsymbol{k},t,t')}\left(\frac{\partial\tilde{\psi}^*_{210}(\boldsymbol{k}+\boldsymbol{A}(t))}{\partial p_z}\right)\,. \tag{2.23}$$

The SPA can not be used directly because of the constant term in the denominator: $\frac{1}{(1+\boldsymbol{p}^2)^4}$. However, it could have been used if there had been $\tilde{\psi}_{210}$ instead of $\partial_{p_z}\tilde{\psi}_{210}$. It motivates us to apply integration by parts in the k-space. The result is

$$d_z^{(210)}(t) \propto -\int\mathrm{d}t'\int\mathrm{d}^3k\;\mathcal{E}(t')\left(\frac{\partial^2\tilde{\psi}_{210}(\boldsymbol{k}+\boldsymbol{A}(t'))}{\partial p_z^2} - \mathbf{i}\frac{\partial\mathcal{S}}{\partial p_z}\frac{\partial\psi_{210}}{\partial p_z}\right)\mathrm{e}^{-\mathbf{i}\mathcal{S}(\boldsymbol{k},t,t')}\tilde{\psi}^*_{210}(\boldsymbol{k}+\boldsymbol{A}(t))\,. \tag{2.24}$$

Now, there is not a problem for the application of the SPA, the term with $\partial_{p_z}\mathcal{S}$ does not contribute at all, because it is exactly zero for the stationary momentum. The resting terms contains already treated ψ^*_{210} and

$$\frac{\partial^2\tilde{\psi}_{210}(\boldsymbol{p})}{\partial p_z^2} = -\frac{1536p_z(3+12p_x^2+12p_y^2-20p_z^2)}{\pi(1+4\boldsymbol{p}^2)^5} \tag{2.25}$$

that does not contain a divergent term either. It means that the integral is not divergent any more and the procedure from the preceding section can be applied.

The generalisation for an arbitrary p-orbital and dipole component is straightforward Following the previous section, an arbitrary component in the direction x_i of the generated dipole is

$$d_i(t) \propto -\int\mathrm{d}t'\int\mathrm{d}^3k\;\partial_{p_i}(\boldsymbol{\mathcal{E}}\cdot\bigtriangledown_{\boldsymbol{p}}\tilde{\psi}(\boldsymbol{k}+\boldsymbol{A}(t')))\mathrm{e}^{-\mathbf{i}\mathcal{S}}\tilde{\psi}(\boldsymbol{k}+\boldsymbol{A}(t))\,,\qquad \tilde{\psi} = \tilde{\psi}_{21(-1)}+\tilde{\psi}_{210}+\tilde{\psi}_{211}\,. \tag{2.26}$$

The first term in the integrand is explicitly

$$\partial_{p_i}(\boldsymbol{\mathcal{E}}\cdot\bigtriangledown_{\boldsymbol{p}}\tilde{\psi}(\boldsymbol{k}+\boldsymbol{A}(t'))) = \mathcal{E}_x\partial_{p_ip_x}\tilde{\psi}+\mathcal{E}_y\partial_{p_ip_y}\tilde{\psi}+\mathcal{E}_z\partial_{p_ip_z}\tilde{\psi}\,. \tag{2.27}$$

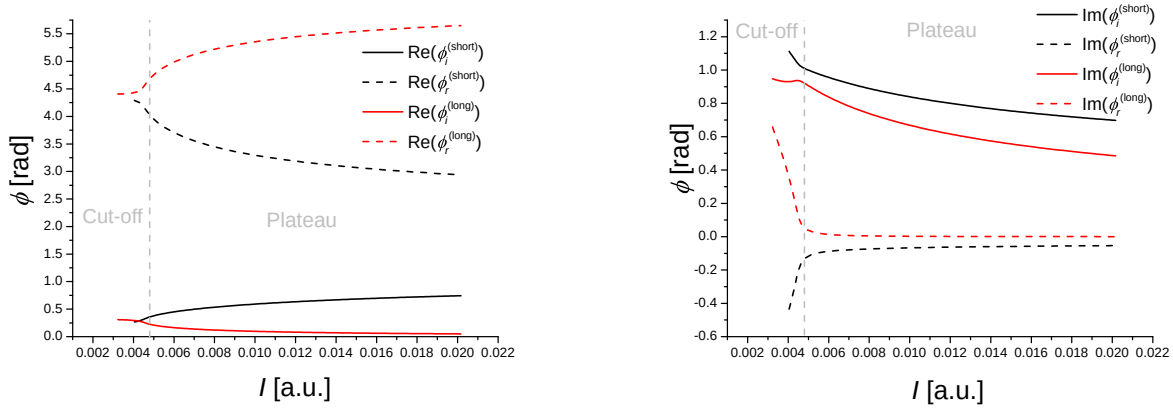

Fig. 2.2: The ionization and recombination time, expressed in the optical-field phase ($\phi = t\omega_0$), as a function of the IR-field intensity. The left figure shows its real part while the right one its imaginary part. This simulation has been done for H35 in Neon.

2.3.4 The Full-Saddle-point approximation (FSPA)

In the section 2.3.1, SPA has been used for the integration over momenta. In this section we will use the SPA for all variables involved in Eq. (2.12), as presented in [4, 7]. The new set of equations for the Saddle points is

$$\frac{\partial \Phi_\omega}{\partial t} = 0 \qquad \Rightarrow \qquad \omega = \frac{(\boldsymbol{k} + \boldsymbol{A}(t_r))^2}{2} - E_g \,, \tag{2.28}$$

$$\frac{\partial \Phi_\omega}{\partial t'} = 0 \qquad \Rightarrow \qquad E_g = \frac{(\boldsymbol{k} + \boldsymbol{A}(t_i))^2}{2} \,, \tag{2.29}$$

$$\bigtriangledown_{\boldsymbol{k}} \Phi_\omega = 0 \qquad \Rightarrow \qquad \boldsymbol{k} = -\frac{\int_{t_i}^{t_r} \boldsymbol{A}(t'')\,\mathrm{d}t''}{(t_r - t_i)} \,, \tag{2.30}$$

These equations have also a deep physical interpretation in the terms of integrals of motion [4]. The equation (2.28) is clearly attributed to conservation of energy at the recombination time t_r. At this time, the photon energy corresponds to the kinetic energy acquired in the field plus the ionization energy. The equation (2.30) refers to the conservation of the momentum between ionization (occurring at the time t_i) and recombination. Consequently, this equation also implies that ionization position coordinates $\boldsymbol{r}(t_i)$ are the same as the recombination position coordinates $\boldsymbol{r}(t_r)$ since $\bigtriangledown_{\boldsymbol{k}} \Phi_\omega = \boldsymbol{r}(t_r) - \boldsymbol{r}(t_i) = 0$. The equation (2.29) clearly refers to the ionization process. Since E_g is negative, only a complex time t_i can solve Eq. (2.29).[6] Consequently all the other variables are also becoming complex. The imaginary part of t_i has no classical equivalent, but it can be understood as a tunnelling time. The real part of t_i is associated the actual time of ionization which occurs close to the field maxima as shown in Fig. 2.2 (the ϕ-axis is the phase of the field, the cosine IR-field has been used). The real part of $(t_r - t_i)$ corresponds to the time spent in the continuum and two classes of trajectories can be distinguished (the so-called short- and long-trajectories respective short and long excursion times) as sketched in Fig. 2.2.

Numerical details of how to compute the solution is now presented. The substitution of the solution (2.30)

[6] Thus, one needs to define $\boldsymbol{A}$ as a function $\mathbb{C} \to \mathbb{C}$ and this function has to be holomorphic because of the proper definition of the complex integration.

into Eqs. (2.28) and (2.29) leads to a set of equations that can be recast as follows

$$\boldsymbol{F}(\boldsymbol{t}) = 0\,, \quad \boldsymbol{t} = (t_1, t_2) = (t, t')\,, \qquad \begin{aligned} F_1(t', t) &= \left.\frac{(\boldsymbol{k} + \boldsymbol{A}(t))^2}{2}\right|_{\boldsymbol{k}=\boldsymbol{k}^{(\mathrm{sp})}_{t,t'}} - E_g - \omega\,, \\ F_2(t', t) &= \left.\frac{(\boldsymbol{k} + \boldsymbol{A}(t'))^2}{2}\right|_{\boldsymbol{k}=\boldsymbol{k}^{(\mathrm{sp})}_{t,t'}} - E_g\,. \end{aligned} \tag{2.31}$$

In order to solve this set of equations numerically we use the Newton iterative method [8]. The algorithm is the following

$$\boldsymbol{t}_{k+1} = \boldsymbol{t}_k - (\mathbb{M}^{(k)})^{-1} \cdot \boldsymbol{F}(\boldsymbol{t}_k)\,, \qquad \mathbb{M}^{(k)}_{ij} = \frac{\partial F_j(\boldsymbol{t}_k)}{\partial t_i}\,, \tag{2.32}$$

where $\boldsymbol{t} = \lim_{n\to+\infty} \boldsymbol{t}_n$. A proper choice of the initial condition $\boldsymbol{t}_0$ allows to retrieve the solution within five to six iterations.

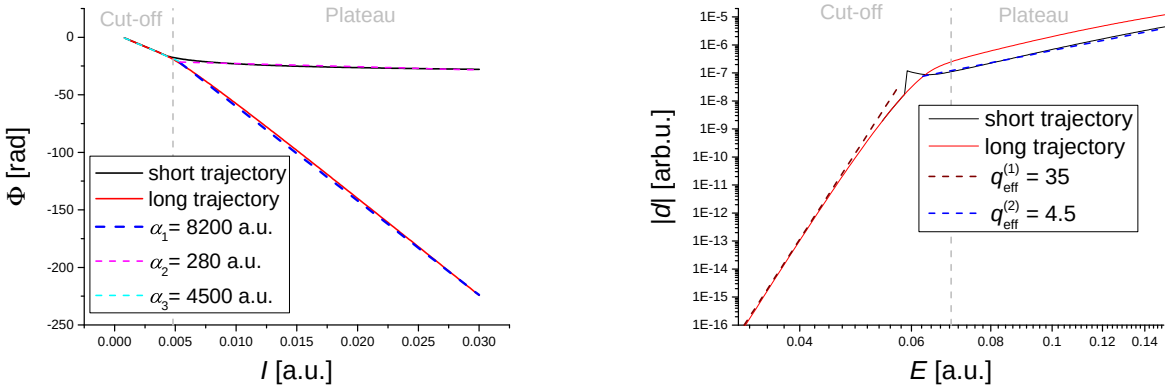

Fig. 2.3: The expression of the generated dipole in dependence on incident field amplitude. The left figure shows evolution of the phase, the right one shows evolution of the modulus. Estimated values of parameters are $\alpha_1 \approx 8200$ a.u., $\alpha_2 \approx 280$ a.u. and $\alpha_3 \approx 4500$ a.u.. This simulation has been done for H35 in Neon. In atomic units, the intensity is given by $I = \mathcal{E}^2$.

The distinction between short- and long-trajectories is completely valid in the plateau (see Fig. 2.2). In the cut-off region, the short and long-trajectories merge only defining one class of trajectory. Going continuously from the plateau to the cut-off region by decreasing intensity requires some carefulness. In particular, if one follows the evolution of the short trajectories as a function of intensity, the imaginary part of the action will become unphysical and the transition from the plateau to the cut-off needs a special treatment [9]. Its detail study exceeds the purpose of this work. Thus, we can run our iteration procedure and validate them a posteriori by substitution into the initial equation.

Once, t_r and t_i are obtained, one can calculate the dipole for short and long-trajectories. The final result is being the coherent sum of the two dipole contributions. The dipole for a given trajectory is written

$$\boldsymbol{d}(\omega) \approx -\frac{\mathbf{i}}{\sqrt{2\pi}} \left(\frac{-2\pi\mathbf{i}}{\sqrt{\det \Phi''_\omega}}\right)^{\frac{5}{2}} \left[\boldsymbol{\mathcal{E}}(t_i) \cdot \boldsymbol{d}(\boldsymbol{k}^{(0)}_{t_r,t_i} + \boldsymbol{A}(t_i)) \mathrm{e}^{\mathbf{i}\Phi_\omega(t_r,t_i,\boldsymbol{k}^{(0)}_{t_r,t_i})}\right] \boldsymbol{d}^*(\boldsymbol{k}^{(0)}_{t_r,t_i} + \boldsymbol{A}(t_r)) + \text{c.c.}\,, \tag{2.33}$$

$$(\Phi''_\omega)_{ij} = \left.\frac{\partial^2 \Phi_\omega}{\partial\xi_i \partial\xi_j}\right|_{\xi^{(0)}_i, \xi^{(0)}_j}\,, \quad \xi_k \in \{t, t', k_x, k_y, k_z\}\,. \tag{2.34}$$

Calculating the dipole Eq. (2.12) for various values of the field amplitude $\mathcal{E}$, one obtains the function $\boldsymbol{d}_\omega(\mathcal{E})$ for a given omega. This expression of the dipole can be written in terms of modulus and phase as given by

$$(d_\omega)_i(\boldsymbol{\mathcal{E}}) = |f_i(\boldsymbol{\mathcal{E}})|\mathrm{e}^{\mathbf{i}\Phi_i(\boldsymbol{\mathcal{E}})} \tag{2.35}$$

for each dipole component i. An illustration of the evolution of the phase and modulus is given in Fig. 2.3 for a linearly polarized field. For low values of intensities a given harmonic (or frequency) lies in the cut-off. For intensities higher than the cut-off limit defined by Eq. (2.13) the given harmonic enters in the plateau region.

In the linear-field case, the evolution of the phase as a function of intensity exhibits a linear behaviour $\Phi = -\alpha I_{\mathrm{IR}}$, where I_{IR} is the intensity of the driving field, with different values of α depending on the class of trajectories. Plotting the dipole modulus as a function of electric field amplitude in log-log scale one can see that the modulus can be expressed as $|d(\mathcal{E})| \propto |\mathcal{E}|^{q_{\mathrm{eff}}}$. q_{eff} is the same for long and short trajectories but differs at the cut-off and plateau. In general, the non-zero-dipole component will be written for a given class class of trajectory and for a given region

$$d_\omega(\mathcal{E}) \propto |\mathcal{E}|^{q_{\mathrm{eff}}}\mathrm{e}^{-\mathbf{i}\alpha I_{\mathrm{IR}}}\,. \tag{2.36}$$

We can see that Eq. (2.36) is generally a good approximation in the plateau and cut-off.

Finally, the presented result Eq. (2.36) has been found using an infinite field. In a real physical application, fields with an envelope in time are used. The way how to extend the result for this case is discussed in Appendix C.

3. CONTROL OF TIME AND FREQUENCY PROPERTIES OF GENERATED XUV

Aiming at practical applications, it is crucial to control the XUV generation. Generally, one can use two different ways. The first one is to use optical elements to modify an already-produced field. However, it is still very difficult to fabricate the optical elements for a XUV region and it is causing losses. The second possibility is to control directly the generation process. The both aspects–microscopic contribution from a single emitter and macroscopic one studying the coherent sum of the emitters in whole medium–are important. We will focus on the single emitter in elliptically polarised laser pulses in this chapter.

3.1 Theory

In the previous chapter, the microscopic response was presented for an arbitrary IR-field and infinite-plane-wave examples were used for an illustration. Now, the IR-field will be specified with more care. The goal is to provide the theory for the so-called *polarisation gating* that is using two delayed counter-rotating elliptical IR-pulses.

3.1.1 Elliptically polarized field

Before proceeding to the XUV-field, necessary definitions for the IR-field have to be recalled. The field is described through the vector potential defined by $\boldsymbol{A} = (A_x, 0, A_z)$. The electric field is then obtained from the vector potential by $\boldsymbol{\mathcal{E}}(t) = -\partial_t \boldsymbol{A}(t)$. The axis-notation is motived by the coordinate system of a microscopic target, where the z-axis is usually the quantization axis of the microscopic target in the direction of the external field. I.e. the field propagates in the y-direction. Keeping the standard notation for the target is more convenient than the use of standard notation for the propagation of the IR-field.

We use an intuitive description given by the vector potential $\boldsymbol{A}(t)$ encircling an ellipse which provides an important insight in our case.[1] First, let us study a situation when the major axis of the ellipse coincides with the z-axis. The light is then defined by

$$A_z(t) = \frac{A_0}{\sqrt{1+\varepsilon^2}} \cos\left(\omega_0 t + \varphi_0\right) = a_\varepsilon \cos\left(\omega_0 t + \delta_z\right) \tag{3.1}$$

$$A_x(t) = \frac{A_0 \varepsilon}{\sqrt{1+\varepsilon^2}} \cos\left(\omega_0 t + p\frac{\pi}{2} + \varphi_0\right) = b_\varepsilon \cos\left(\omega_0 t + \delta_x\right) , \tag{3.2}$$

$p \in \{\pm 1\}$ determines the direction of the circulation, i.e. the sense of the polarization, and the ellipticity ε is the fraction of the lengths of the major and minor axis. This notation allows a simple connection between the amplitude, average-electric-field strength and intensity

$$\sqrt{I} = \mathcal{E}_0 = \sqrt{\left\langle \boldsymbol{\mathcal{E}}^2 \right\rangle_{T_0}} = \sqrt{\left\langle \left(-\partial_t \boldsymbol{A}\right)^2 \right\rangle_{T_0}} = \omega_0 A_0 \,, \qquad\qquad T_0 = \frac{2\pi}{\omega_0} \,. \tag{3.3}$$

In the next step, any of all the possible states is obtained by a rotation of the ellipse by a given angle θ. Hence

$$\boldsymbol{A}'(t) = R_2(\theta)\boldsymbol{A}(t) \,. \tag{3.4}$$

[1] From the theoretical point of view, the all possible ellipticity states can be identified with the Ponicaré sphere that shows a similarity with two-level quantum systems.

The application of Eq. (B.1) gives

$$A_i'(t) = \mathcal{A}_i \cos\left(\omega_0 t + \phi_i\right) , \quad i \in \{z, x\} , \tag{3.5}$$

$$\mathcal{A}_z = \sqrt{a_\varepsilon^2 \cos^2(\theta) + b_\varepsilon^2 \sin^2(\theta)} , \tag{3.6}$$

$$\mathcal{A}_x = \sqrt{a_\varepsilon^2 \sin^2(\theta) + b_\varepsilon^2 \cos^2(\theta)} , \tag{3.7}$$

$$\phi_z = \operatorname{atan2}(a_\varepsilon \cos(\theta)\sin(\delta_z) - b_\varepsilon \sin(\theta)\sin(\delta_x), a_\varepsilon \cos(\theta)\cos(\delta_z) - b_\varepsilon \sin(\theta)\cos(\delta_x)) , \tag{3.8}$$

$$\phi_x = \operatorname{atan2}(a_\varepsilon \sin(\theta)\sin(\delta_z) + b_\varepsilon \cos(\theta)\sin(\delta_x), a_\varepsilon \sin(\theta)\cos(\delta_z) + b_\varepsilon \cos(\theta)\cos(\delta_x)) . \tag{3.9}$$

Thus, we have found the universal analytic form (3.5) of an arbitrary polarized field. The field is then completely defined by the six parameters ω_0, A_0, ε, p, φ_0 and θ.

3.1.2 Envelope of the field

A laser in a pulse regime is usually used for the HHG. In this case, the radiation is well described by the product of a fast oscillating harmonic part with a frequency ω_0 and a time-and-space dependent envelope. A realistic model can be reached by the substitution of the constant amplitude A_0 by the envelope $A_0(\boldsymbol{r}, t)$. The spatial profile refers to the macroscopic aspect and it will be treated in the following chapter. Considering the temporal evolution, the envelope is called *slowly varying* if $\left|\frac{\partial A_0(t)}{\partial t}\right| \ll \omega_0 A_0(t)$. If the condition is fulfilled, the left-hand-side term is neglected. This is called the *Slowly varying envelope approximation (SVEA)*.[2] The $\sin^2$-envelope is chosen:

$$A_0(t) = \begin{cases} \tilde{A}_0 \sin^2(\omega_c t) , & \text{if } t \in [0, T_c] \\ 0 , & \text{otherwise} \end{cases} , \qquad T_c \omega_c = \pi , \tag{3.10}$$

where $\tilde{A}_0$ is the peak-envelope amplitude.[3]

Now, the complete construction of a single IR-pulse is done. Simplifying the notation, the field is defined by

$$\boldsymbol{A}(t) = \begin{cases} A_0 \sin^2(\omega_c t)\boldsymbol{a}(t, \omega_0, \varepsilon, \theta) , & \text{if } t \in [0, T_c] \\ 0 , & \text{otherwise} \end{cases} , \qquad T_c \omega_c = \pi , \tag{3.11}$$

where $\boldsymbol{a}$ is given by (3.5) with the unit amplitude. Finally we have a single pulse fully defined by ω_0, ω_c, A_0, ε, p, φ_0 and θ.

3.1.3 Sum of two elliptical fields

The vector potentials of classical fields satisfy the superposition principle, it means that the sum-field of two fields $\boldsymbol{A}_1(t)$ and $\boldsymbol{A}_2(t)$ is given by $\boldsymbol{A}(t) = \boldsymbol{A}_1(t) + \boldsymbol{A}_2(t)$. An example is provided in Fig. 3.1. For all fields defined by a $\sin^2$ envelope, the resulting field is always written as a finite combination of goniometric functions and all necessary quantities involved in the dipole (e.g. $\int \boldsymbol{A}^2(t)\,\mathrm{d}t$) can be still resolved analytically.[4] The spectral components of the resulting field consist the sums and differences of the summed-fields frequencies and the spectral properties are also modified by the envelopes. Special cases for fields with a common fundamental frequency ω_0 will be treated in the following sections.

[2] For example, the possibility to define all quantities in the vector potential instead of the electric field, as it was stated in the first paragraph of this section, is exactly the case. In our case, the limit for the SVEA use is ~ 5 fs pulse for an 800-nm laser (The error for the 5-fs pulse (using the $t_{\mathrm{FWHM}} = 5$ fs, see Eq. (D.2)) is estimated by $\frac{2\omega_c}{\omega_0} = \frac{2\lambda_{800\,\mathrm{nm}} \arcsin\left(\frac{1}{4}\right)}{\pi c t_{\mathrm{FWHM}}} \approx 9\%$).

[3] Our choice is advantageous from the theoretical point of view. The reasons are that there are not difficulties in analytical calculations such as integrals needed in the following section. From the numerical point of view, the support of the envelope is finite therefore there are not problems in choosing proper finite grid in time. Regarding the correspondence with experiments, present-day techniques are still far enough to control the shape of the envelope with such a precision making the small differences to play a role.

[4] Namely, there is no inconvenience in our implementation of the microscopic response.

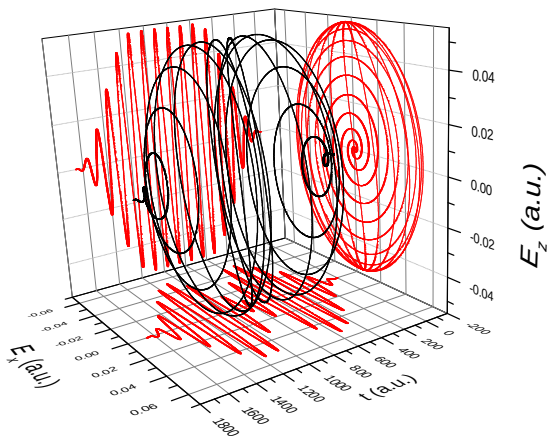

Fig. 3.1: The electric field given by the superposition of two circular pulses. The simulation parameters are: the delay case $\omega_c\tau = \frac{\pi}{2}$, 10-cycle pulses, $\varepsilon = 1$ and $\mathcal{E}_0 = 0.075$ a.u.

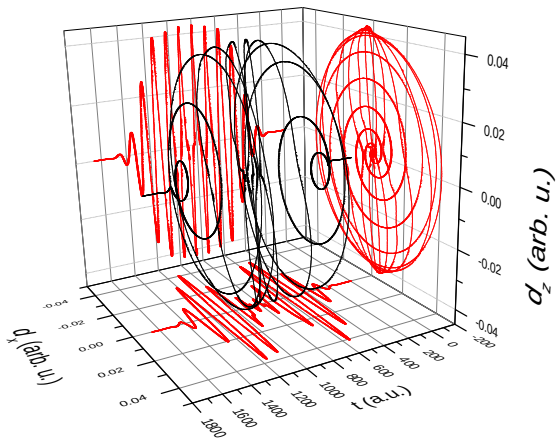

Fig. 3.2: The dipole generated under the polarisation gating by the field shown in Fig. 3.1. The typical structure of the XUV-generation can be seen around the time 800 a.u. on the projection in the $d_z t$-plane and the electron is not approaching the nucleus elsewhere.

3.1.4 Two pulses with common ω_0 and instantaneous ellipticity

In the case of a common fundamental frequency, the fields are both given by Eq. (3.5), explicitly

$$A_j^{(i)}(t) = \mathcal{A}_j^{(i)} \cos(\omega_0 t + \phi_j^{(i)})\,, \qquad i \in \{1,2\}\,, \qquad j \in \{z,x\}\,, \tag{3.12}$$

i numbers the field and j denotes its components. Using Eq. (B.1), the sum of two elliptical fields without considering envelopes is an elliptical field,

$$A_j(t) = A_j^{(1)}(t) + A_j^{(2)}(t) = \mathcal{A}_j \cos(\omega_0 t + \phi_j)\,, \qquad j \in \{z,x\}\,. \tag{3.13}$$

Next, the effects of the fields envelopes that have not been considered yet, are needed to be clarified. The envelopes are incorporated by the substitution $\mathcal{A}_j^{(i)} \to \mathcal{A}_j^{(i)}(t)$. Applying the same technique as in the previous section, we can see that it induces changes $\mathcal{A}_j \to \mathcal{A}_j(t)$ and $\phi_j \to \phi_j(t)$. The latter is very important because it generally introduces a time evolution of the phase shift and this effect has not been presented in our theory before. But also the effect for the amplitudes is partially new, they are now generally decoupled for each axis. Furthermore, if the envelopes of the fields $\boldsymbol{A}_1$ and $\boldsymbol{A}_2$ are slowly varying, also the phase shifts and the each-axis envelopes are slowly varying. In that case, all these parameters can be seen as the defining quantities of a slowly varying ellipticity throughout the sum-pulse duration.

3.1.5 Instantaneous ellipticity

When the SVEA is applied, the phase shifts and amplitudes can be supposed being constant in the range of a single optical cycle. Hence, the field has the form

$$A_z = \mathcal{A}_z \cos(\omega_0 t + \varphi_z)\,, \tag{3.14}$$

$$A_x = \mathcal{A}_x \cos(\omega_0 t + \varphi_x)\,. \tag{3.15}$$

in that range. Recalling the intuitive model of the field vector encircling an ellipse, the encircled ellipse is given in Cartesian coordinates by

$$\xi A_z^2 + 2\lambda A_x A_z + \eta A_x^2 = 1\,, \tag{3.16}$$

the only task is to find the defining parameters ξ, η and λ.[5] This is reached by comparison of both sides of the last equation, the result is

$$\xi = \frac{1}{\mathcal{A}_z^2 \sin^2(\Delta\varphi)}\,, \qquad \eta = \frac{1}{\mathcal{A}_x^2 \sin^2(\Delta\varphi)}\,, \qquad \lambda = \frac{-\cos(\Delta\varphi)}{\mathcal{A}_x \mathcal{A}_z \sin^2(\Delta\varphi)}\,, \qquad \Delta\varphi = \varphi_z - \varphi_x\,. \tag{3.17}$$

Using analytic geometry [10], one finds the major and minor axis of the ellipse

$$a' = \sqrt{\frac{2}{(\xi+\eta) - \sqrt{(\xi-\eta)^2 + 4\lambda^2}}}\,, \qquad b' = \sqrt{\frac{2}{(\xi+\eta) + \sqrt{(\xi-\eta)^2 + 4\lambda^2}}}\,, \tag{3.18}$$

respectively, and also the deviation of the main axis from the z-axis,

$$\theta = \begin{cases} 0\,, & \text{for } \lambda = 0 \text{ and } \xi < \eta \\ \frac{\pi}{2}\,, & \text{for } \lambda = 0 \text{ and } \xi > \eta \\ \frac{\operatorname{arccot}\left(\frac{\xi-\eta}{2\lambda}\right)}{2}\,, & \text{for } \lambda \neq 0 \text{ and } \xi > \eta \\ \frac{\pi + \operatorname{arccot}\left(\frac{\xi-\eta}{2\lambda}\right)}{2}\,, & \text{for } \lambda \neq 0 \text{ and } \xi < \eta \end{cases}\,. \tag{3.19}$$

The result ellipticity is given by

$$\varepsilon = \min\left\{\frac{a'}{b'}, \frac{b'}{a'}\right\} \tag{3.20}$$

and all needed quantities are obtained. The final instantaneous quantities are obtained by including time evolution into $\mathcal{A}_i$ and φ_i, $i \in \{z, x\}$. See attached Mathematica®worksheet, Appendix F. (Referring the SVAE assumption, the instantaneousness has to be taken always at least in the range of one optical cycle.)

3.1.6 Polarisation gating

.

Now, the microscopic response can be revisited. Starting with an elliptical IR-field, HHG is known to be sensitive on the degree of ellipticity of the IR-field. It can be simply reasoned from the intuitive three-step model, the electron returns to the core and recombines in a linear field while it misses the core due to the extra-spatial-dimension motion in the elliptical case. The mathematical form of the XUV yield as a function of the IR-field ellipticity, ε, originating from the quantum model [11] is $I_{\mathrm{XUV}} \propto \mathrm{e}^{-\beta\varepsilon^2}$. The parameter β increases with the harmonic order. The analysis corresponding to our conditions will be done in the section 3.2.1.

Furthermore, the previous section answers the question of how to produce a field that is linearly polarized only for a short interval (and it is elliptical elsewhere) of time where the XUV generation is possible. The interval where the XUV is produced is the so-called *gate*. Figures 3.1 and 3.2 illustrate polarisation gating respectively for the IR electric field and the resulting dipole.

Now, the formal definition is provided, the notation follows definitions in the vector potential following the previous sections. The field is in that case a sum of two oppositely elliptically polarized fields,

$$\boldsymbol{A}(t) = \boldsymbol{A}_{\circlearrowleft}(t) + \boldsymbol{A}_{\circlearrowright}(t) = A_0(\boldsymbol{A}_{\circlearrowleft}(t) + s\boldsymbol{A}_{\circlearrowright}(t))\,, \tag{3.21}$$

the fields on the right-hand side of the equation are defined by formulae (3.11), the polarization state is determined by the identification $\circlearrowleft$ and $\circlearrowright$ with $p \in \{\pm 1\}$. The definition of the polarisation gating is a common frequency ω_0 for both fields. Next parameters that are common in our particular case are ω_c, ε and θ that has opposite sign for each of the fields. The resting parameter is the delay τ. The second form is obtained by the identification $A_0 = A_{0,\circlearrowleft}$ and $s = \frac{A_{0,\circlearrowright}}{A_{0,\circlearrowleft}}$ and it is useful when polarisation-gating properties will be studied as a function of s (see Fig. 3.11 for an example of pulses with a different peak amplitude.). In the following sections, special conditions and properties of the XUV generation in the polarisation gating regime will be treated.

[5] In fact, it is only the inverse procedure to the elliptical field construction presented in the section 3.1.1.

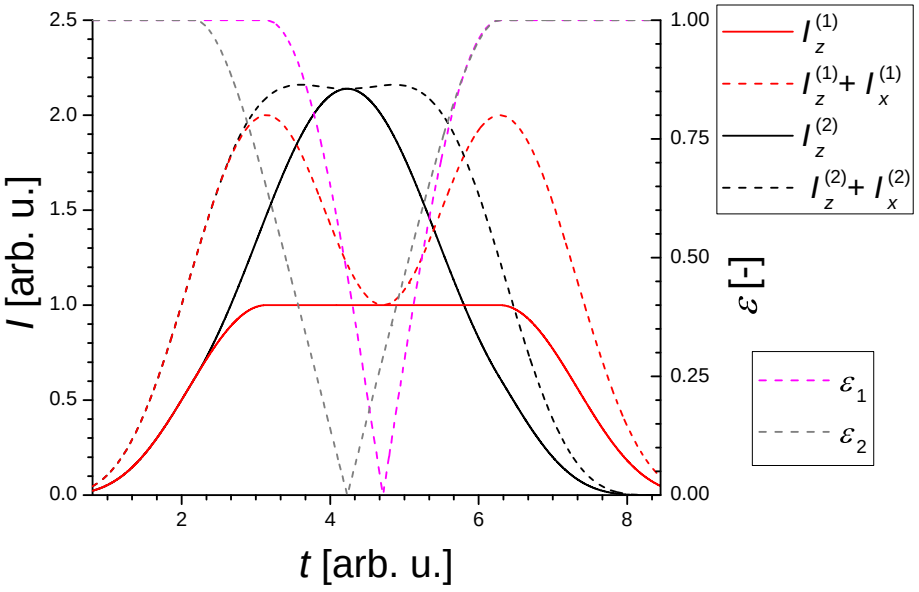

Fig. 3.3: The two special cases: gate-axis components (solid lines), sum-of-both-axis intensities (dash lines) and corresponding ellipticities. $\mathcal{E}_0 = 1$ is chosen as the common parameter of both plots. We can see that the gate-intensity is twice higher for the second case, however the gate is broader.

3.1.7 Efficiency of polarisation gating, two special cases

Now, the potency of the polarisation gating as a function of the delay τ need to be investigated. Basically, there are two effects to optimise. First, the efficiency of the generation is reached by maximising the intensity inside the gate, i.e. decreasing τ.[6] On the other hand, the delay τ is longer, a sharper ellipticity peak one has, i.e. the effectiveness of the polarisation gating increases as the gate becomes shorter. The task is to find an optimum between the two effects. It should be additionally noted, that the gate duration is relative to the pulse duration and the second property can be also optimised by the pulse shortening.

For the purposes of this work, two concrete values of τ have been chosen. The fist one is given by the condition that the amplitude of the z-component of the IR-field is a constant for $\omega_c t \in [\omega_c\tau, \pi]$, it leads to $\tau = \frac{\pi}{2\omega_c}$. The second one is found from the condition that the total field intensity $I = \boldsymbol{\mathcal{E}}^2$ is almost flat. We have identified the value $\omega_c\tau \approx 1.09$. These choices are illustrated in Fig. 3.3, there are shown normalized values of: total intensity I, its gate-major-axis component I_z and ellipticity, for each of the delays. For later references, these two delays are called as:

$$\omega_c\tau = \begin{cases} \frac{\pi}{2}\,, & \textit{the long-pulse delay} \\ 1.09\,, & \textit{the short-pulse delay} \end{cases} . \tag{3.22}$$

The chosen values can be also taken as representatives of the cases when the global-field maxima are reached far from the gate or near the gate, respectively. Furthermore, it is clear that the cut-off frequency as defined by Eq. (2.13) is pulse-duration independent while the delay is defined relatively to the envelope as it has been done in this work.

[6] One has the factor $\sin^4(\omega_c t_0)$ as will be shown in the Result section, Eq. (2.13). However, for $\tau = 0$ the field is linear and there is no gating at all.

3.2 Results

In this section, the results about the polarisation gating based on KSPA simulations for Hydrogen target are discussed. First, the principle of the polarisation gating is studied looking at harmonic generation by elliptical IR-fields. Then, the cut-off law using the polarisation gating is investigated. Next, we focus on a spectral feature that appears when the polarisation gating is involved in HHG. As it was shown in Fig. 2.1, harmonic spectra look blurry in the plateau region. In this work we will show that the use of the polarisation gating may clear out the harmonics spectra in this region. We will also study more carefully physical mechanisms leading to the spectral structure. Finally, the XUV-frequency control using the pulse-amplitude asymmetry is presented. From the experimental point of view the polarisation gating is obtained by using one circularly polarised IR pulse and its temporally delayed counter-rotating replica. For our study, the same configuration will be used. The variable that will be used is the amplitude of the replica as compared to the main pulse. The ratio between the main-pulse and the replica amplitudes is noted s.

Needed to mention, θ is always set to zero for both pulses (see Eq. (3.4)).

3.2.1 HHG in elliptical fields

We have applied the KSPA approximation and we have obtained the yield-ellipticity dependence shown in Fig. 3.4. The yield for a given harmonic q_0 is defined by $\eta(\varepsilon, q_0) = \frac{E_{\mathrm{XUV}}(\varepsilon,q_0)}{E_{\mathrm{XUV}}(\varepsilon=0,q_0)}$, where

$$E_{\mathrm{XUV}}(\varepsilon, q_0) = \int_{q_0-1}^{q_0+1} I_{\mathrm{XUV}}(\varepsilon, q)\,\mathrm{d}q \tag{3.23}$$

is used to retrieve the spectral contribution to the given harmonic q_0. The major- and minor-axis contributions are summed but Fig. 3.5 proves that the minor-axis contribution is negligible. The simulations have been performed for 10- and 20-cycle pulses (they are denoted by N specifying the number of cycles). The expected exponential dependence is fitted by $\mathrm{e}^{-\beta_q^{(N)}\varepsilon^2}$, x denotes the pulse duration and q the harmonic order. Several issues should be emphasised in the results.

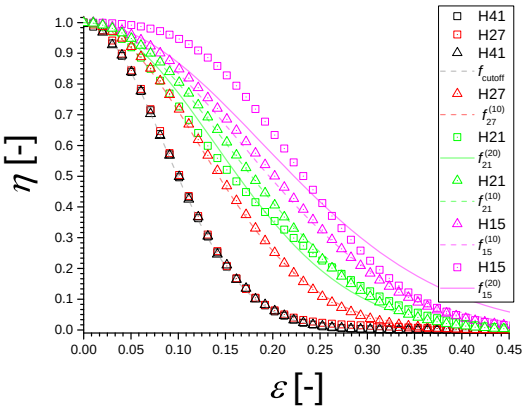

Fig. 3.4: The XUV yield for several harmonics compared with the theoretical forms $f_q^{(N)}$. The corresponding parameters are $\beta_{\mathrm{cutoff}} = 70$, $\beta_{15}^{(10)} = 18$, $\beta_{21}^{(10)} = 22$, $\beta_{27}^{(10)} = 34$, $\beta_{15}^{(20)} = 14$ and $\beta_{21}^{(20)} = 26$. The triangles and squares denote, respectively, 10- and 20-cycle pulses.

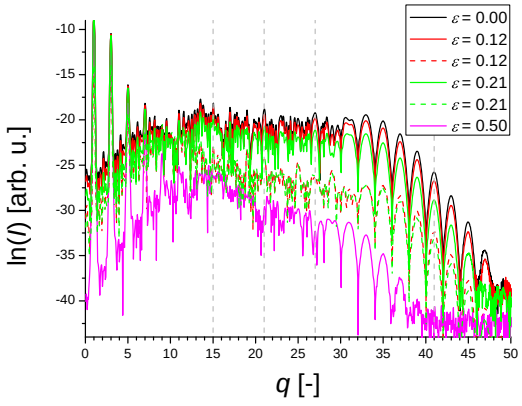

Fig. 3.5: The spectra obtained by the SFA model for the elliptical IR-field for the given ellipticities ε. The solid lines show the major-axis spectra, dashed lines the minor-axis ones. The vertical grey lines correspond to the harmonics in Fig. 3.4.

First, let us look at the expected decrease $\mathrm{e}^{-\beta\varepsilon^2}$. It is definitely obeyed better by the short-pulse yields. It may look surprising, that results for a short pulse correspond better to the theory developed for an infinite-plane-wave IR-field than long-pulse ones. However in the short-pulse case, all the harmonics are generated in the same regime for a very short pulse while they traverse through different regions because the IR-field envelope spans a larger field amplitude range in the generating region for a long pulse. In conclusion, it shows that very short pulses can be closer to an infinite-plane-wave theory than longer ones in particular cases.

In addition, the yield is both N- and q-dependent. The results confirm that β increases with the harmonic order. Next, the dependence of β on the pulse duration is not so clear, e.g. for the H21 $\beta_{21}^{(20)} > \beta_{21}^{(10)}$ while for H15 $\beta_{15}^{(20)} < \beta_{15}^{(10)}$ and they are both in the plateau region.

In summary, the expected exponential XUV-yield dependence on the IR-field ellipticity, ε, has been proven. In particular, increasing ε can effectively prevent from the XUV generation. This is exactly the property leading to the polarisation gating as mentioned in the section 3.1.6. The polarisation gating will be now investigated more in detail.

3.2.2 Polarisation gating: Cut-off law

One of the most important characteristics of the XUV spectrum is its cut-off. The larger, the shorter XUV pulses can be produced. It is given by $E_{\mathrm{cutoff}} = I_P + 3.17 \cdot U_p$ for a linear field. Now, we will estimate the cut-off using the polarisation gating. A symmetrical case of two counter-rotating elliptical fields is considered. In addition, the axis where the linearity of the IR field is reached is set on the major axis of the ellipse.[7]

The field is written

$$A_z(t) = \frac{A_0}{\sqrt{1+\varepsilon^2}} \left[\sin^2(\omega_c t) + \sin^2(\omega_c (t-\tau))\right] \cos(\omega_0 t)\,, \quad A_x(t) = \frac{\varepsilon A_0}{\sqrt{1+\varepsilon^2}} \left[\sin^2(\omega_c t) - \sin^2(\omega_c (t-\tau))\right] \sin(\omega_0 t)\,. \tag{3.24}$$

This expression allows to find the time t_0 when $\boldsymbol{A}(t_0)$ is linearly polarized. This time is given by the root of the x-component envelope. This condition has a solution obtained by solving

$$\sin^2(\omega_c t) = \sin^2(\omega_c (t-\tau)) \qquad \Rightarrow \qquad t_0 = \frac{\tau + \frac{\pi}{\omega_c}}{2}\,. \tag{3.25}$$

The linear component of the IR-field is then $A_z(t) = \frac{2A_0}{\sqrt{1+\varepsilon^2}} \sin^2(\omega_c t_0) \cos(\omega_0 t)$, (the SVEA fulfilment is assumed). Applying the cut-off law for this vector-potential amplitude, the polarisation-gating cut-off is

$$E_{\mathrm{cutoff}} = I_P + 3.17 \cdot A_0^2 \frac{\sin^4(\omega_c t_0)}{1+\varepsilon^2} = I_P + 3.17 \cdot \left(\frac{4\sin^4(\omega_c t_0)}{1+\varepsilon^2}\right) \tilde{U}_p\,, \tag{3.26}$$

where $\tilde{U}_p = \frac{A_0^2}{4}$ is the ponderomotive energy at the maximum of each IR-pulse.[8]

Our derivation lies on a very simple idea that the XUV-radiation is generated only in the gate, when the field is linear. However this is not true in all cases. E.g. the intensity in the gate as a function of the delay is either higher or lower then the global maximum or maxima of the field. It may cause that the XUV generation is non-negligible outside the gate for low ellipticities.

The proposed cut-off law has been investigated using KSPA-based simulations. Its validity as a function of the electric-field amplitude and ellipticity is shown respectively in Figs. 3.6 and 3.7. One can see that Eq. (3.26) estimates qualitatively well the cut-off position.

Let us discuss closer the cases where the cut-off law, Eq. (3.26), could fail. Needed to emphasise, it is connected with a XUV production outside the gate or its cancellation thus it also limits the utility of the polarisation gating itself. This is reached when the gate-intensity is too low (a long pulse delay) and the

[7] It means that the phase shifts of both fundamental fields are the same. Their possible mismatch causes angular deviation of the resulting field. This is particularly important for non-circular pulses. If the gate is reached on the minor axis, the sum-fields amplitude is ε-times lower, i.e. the intensity is ε^2-times lower, then if it is reached on the major one.

[8] It means that $\tilde{U}_p$ does not have a strictly connected sense in terms of local field in t_0, but with the defining parameter A_0.

generation outside the gate is non-negligible even in an elliptical field. Equivalently, the small values of the ellipticity parameter ε leads to the same result under similar conditions. Thereafter, the importance of the CEP-phase difference has to be reminded, it controls only the deviation angle of the gate for circular pulses. However, it can lead to gate on the minor axis for elliptical pulses and thus prevents XUV generation (the intensity corresponding to the gate reached on minor axis is ε^2-lower than if it is reached on the major one). This effect is illustrated in Fig. 3.8.

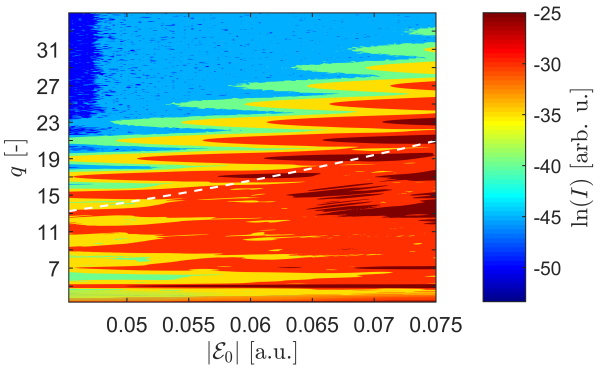

Fig. 3.6: The XUV-yield in the polarisation gating setup. The white dashed line shows expected cutoff (3.26) as a function of $|\mathcal{E}_0|$. The simulation has been done done for the delay $\omega_c\tau = \frac{\pi}{2}$, 20-cycle pulses and $\varepsilon = 1$.

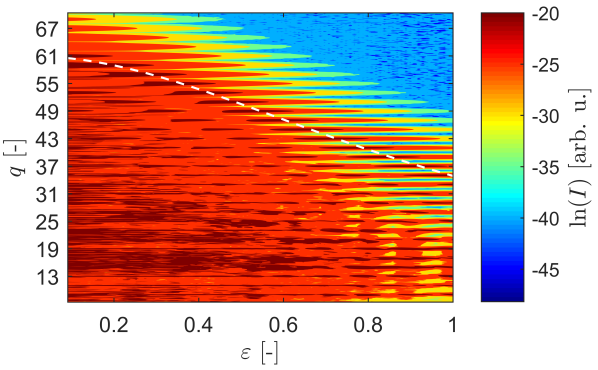

Fig. 3.7: The XUV-yield in the polarisation gating setup. The white dashed line shows expected cutoff (3.26) as a function of ε. The *purified* spectrum can be observed around $\varepsilon = 1$. The simulation has been done done for the delay $\omega_c\tau = 1.09$, 20-cycle pulses and $\mathcal{E}_0 = 0.075$ a.u.

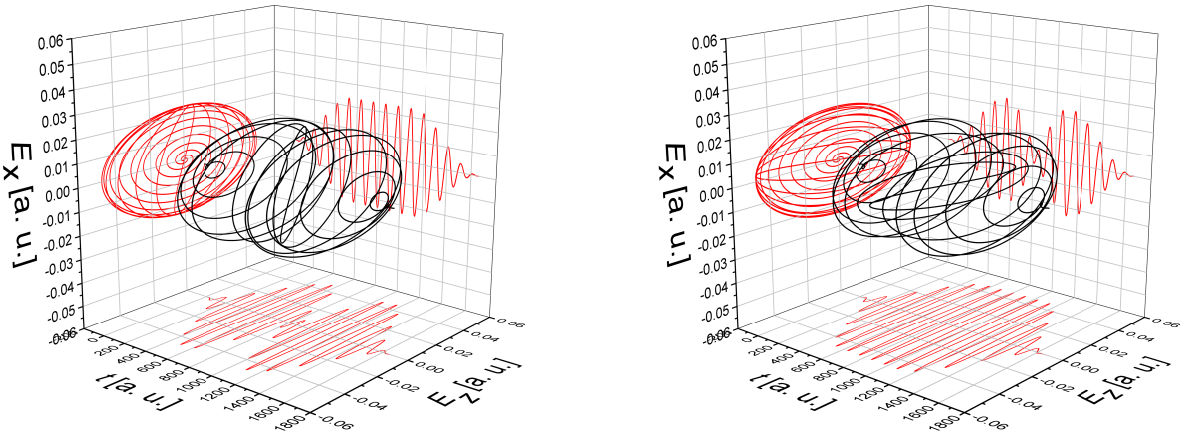

Fig. 3.8: These plots show two limit cases of the resulting field obtained by the superposition of two delayed elliptical counter-rotating pulses. The left plot shows the gate reached on the minor axis of the ellipse while the right plot shows the gate reached on the major axis. The fields are chosen the following way: $A_z(t) = \frac{a^{(\mp)}(t)}{\sqrt{1+\varepsilon^2}}\cos(\omega_0 t)$, $A_x(t) = \frac{\varepsilon a^{(\pm)}(t)}{\sqrt{1+\varepsilon^2}}\sin(\omega_0 t)$, the envelope $a^{(-)}$ in A_z is used for the left plot and it is defined by $a^{(\pm)}(t) = A_0[\sin^2(\omega_c t) \pm \sin^2(\omega_c(t-\tau))]$. The field parameters are $\mathcal{E}_0 = 0.075$ a.u., 10-cycle pulses, $\varepsilon = \frac{1}{2}$ and the delay is 5 cycles.

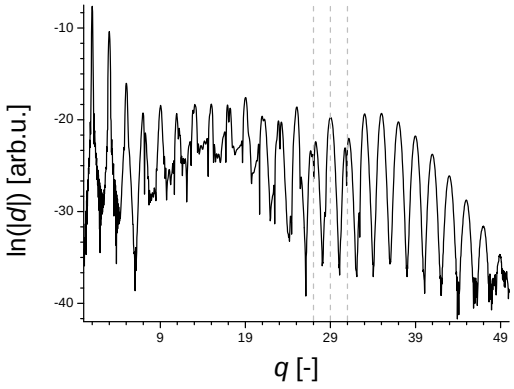

Fig. 3.9: The spectrum generated using the polarisation gating for $\varepsilon = 1$, showing that harmonics $q \in [23, 35]$ are in the plateau.

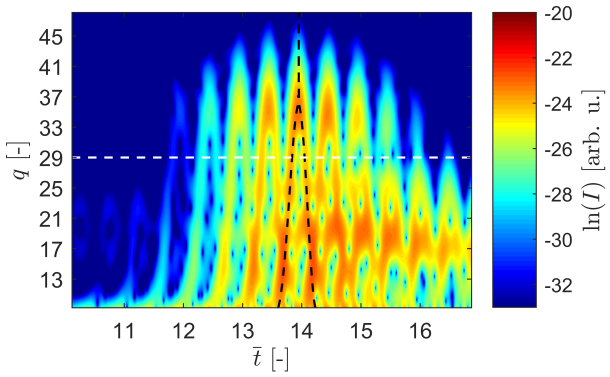

Fig. 3.10: The Gabor analysis of the spectrum shown in Fig. 3.9. It represents generated XUV-photon energy in the terms of the harmonic order q as a function of normalised time $\bar{t} = \frac{t}{T_0}$, where $T_0 = \frac{2\pi}{\omega_0}$. The trajectory classes can be easily identified in the figure. There is also the solution originating from the FSPA (black dashed line) obtained from the plane-wave-based simulation. White lines shows the position of H29.

3.2.3 Polarisation gating: Plateau purification

There is another notable property emerging from Fig. 3.7. Focusing in the region of harmonics $q \in [23, 25]$ and ellipticity ε in the vicinity of one. The harmonics are well separated also in the discussed region while they are usually merged in all the plateau range in SFA simulations (see the spectrum in Fig. 2.1). This property will be called *the plateau purification*. Before starting further analysis, we verify that these harmonics are really in the plateau, as presented in Fig. 3.9.

A further analysis is provided by the so-called *Gabor transform*, which resolve frequencies generated by the dipole as functions of time (see Appendix E), that is given in Fig. 3.10. In fact, high response corresponds to times when the given spectral component is born. These times have exactly the same meaning as the recombination times in the FSPA that are also traced in Fig. 3.10 by the black dashed lines. Let us focus on the situation around H29 in the purified region. According to the Gabor transform, this harmonic is generated always in the plateau regime. The generation on the edges of the plot is suppressed by the ellipticity, it means H29 is generated only by the field with flat amplitude envelope, especially it is never generated efficiently in the cut-off regime. This is the difference between the polarisation-gating and single-linear-pulse generation and it is the origin of the purification.

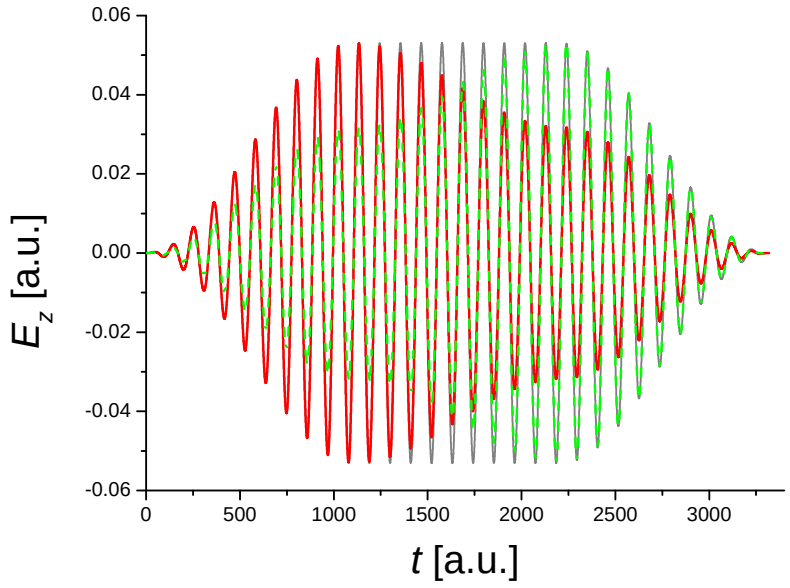

Fig. 3.11: Three examples of the gate-axis electric fields for different values of $\tilde{s}$ parameters. The grey line shows symmetrical case with $\tilde{s} = 1$, the red line $\tilde{s} = 0.6$ and the green line $\tilde{s} = 1.4$. Corresponding configurations defined by s are respectively: $s = 1$; $s = 0.6$, $\mathcal{E}_1 > \mathcal{E}_2$ and $s = 0.6$, $\mathcal{E}_1 < \mathcal{E}_2$.

3.2.4 XUV-frequency shift induced by temporal evolution of IR-intensity

Finally, a practical application of the polarisation gating can be discussed. One of the important goals of the HHG is to control the XUV frequency. For the derivation purposes, let us assume that the XUV-phase-shift temporal control is available. It allows us to write the complete phase and instantaneous frequency for a given harmonic q, i.e.

$$\phi_q(t) = q\omega_0 t + \varphi_q(t) \qquad \Rightarrow \qquad \omega_q(t) = \frac{\partial \phi_q(t)}{\partial t} = q\omega_0 + \frac{\partial \varphi_q(t)}{\partial t}\,. \tag{3.27}$$

The fundamental frequency, $q\omega_0$, is now modified by the factor $\partial_t \varphi_q(t)$. Recalling Eq. (2.36), the XUV phase shift, φ_q, depends linearly on the IR-intensity. Allowing its variation in time, the last term in Eq. (3.27) reads

$$\frac{\partial \varphi_q(t)}{\partial t} = \alpha_q \frac{\mathrm{d}I_{\mathrm{IR}}(t)}{\mathrm{d}t}\,. \tag{3.28}$$

The estimation of α_q is provided by the microscopic response (2.36). The last question is the way to control the temporal profile of the intensity, $I_{\mathrm{IR}}(t)$, in the gate. The discussed possibility is being the peak-electric-field asymmetry between the pulses, i.e. the variation of the s parameter.

3.2.5 Polarisation gating: control of the generated frequency

A theoretical prediction of the frequency-shift s-dependence is obtained by the estimation of the IR-field-intensity variation. Next, the analytic form of the IR-field is chosen in the symmetrical case, $s = 1$, as

$$\mathcal{E}_z(t) = \frac{1}{\sqrt{2}}\left(\mathcal{E}_1 \sin^2(\omega_c t) + \mathcal{E}_2 \sin^2(\omega_c (t-\tau))\right)\cos(\omega_0 t)\,, \tag{3.29}$$

the shift law will be studied as a function of $s = \min\left\{\frac{\mathcal{E}_1}{\mathcal{E}_2}, \frac{\mathcal{E}_2}{\mathcal{E}_1}\right\}$ and $\mathcal{E}_0 = \max\{\mathcal{E}_1, \mathcal{E}_2\}$.[9] The physical meaning of these new variables is clear, $\mathcal{E}_0$ is the electric-field amplitude at the peak of the most intense pulse, the second pulse amplitude is then decreased by the factor s. The case when $\mathcal{E}_1 > \mathcal{E}_2$ is presented in the following. The opposite situation is analogous.

In the vicinity of the gate, where $t = t_0$, the x-electric-field component is negligible and the intensity is given only by its z-component,

$$I_z(t) = \frac{\mathcal{E}_0^2}{2}\left(\sin^2(\omega_c t) + s\sin^2(\omega_c(t-\tau))\right)^2 , \tag{3.30}$$

$$\frac{\mathrm{d}I_z(t)}{\mathrm{d}t} = \omega_c\mathcal{E}_0^2\left(\sin^2(\omega_c t) + s\sin^2(\omega_c(t-\tau))\right)\left(\sin(2\omega_c t) + s\sin(2\omega_c(t-\tau))\right) . \tag{3.31}$$

The slope of the intensity is then estimated by the evaluation of $\left.\frac{\mathrm{d}I_z(t)}{\mathrm{d}t}\right|_{t=t_0}$. The first order in s in the vicinity of the symmetrical case ($s = 1$) gives

$$\frac{\mathrm{d}I_z(t)}{\mathrm{d}t} \approx \begin{cases} \frac{3}{2}\mathcal{E}_0^2\omega_c(s-1)\,, & \text{for } \omega_c\tau = \frac{\pi}{2} \\ 1.345\cdot\mathcal{E}_0^2\omega_c(s-1)\,, & \text{for } \omega_c\tau = 1.09 \end{cases} , \tag{3.32}$$

where two special pulse-delays from the section 3.1.7 have been used. One can see the result is also determined by the values of $\mathcal{E}_0$ and ω_c. Considering $\omega_c \propto \frac{1}{T_c}$ (where T_c is the pulse duration), the slope is controlled by changing the pulse duration. Similarly, it is modified by the peak IR-field intensity $I_{\mathrm{IR}} = \mathcal{E}_0^2$.

Performing the same calculation for $\mathcal{E}_2 > \mathcal{E}_1$, one obtains only the opposite sign. For practical purposes, these two cases can be connected by the definition of

$$\tilde{s} = \begin{cases} (s-1)\,, & \text{for } \mathcal{E}_1 > \mathcal{E}_2 \\ (2-s)\,, & \text{for } \mathcal{E}_1 < \mathcal{E}_2 \end{cases} . \tag{3.33}$$

All the situations where two pulses are presented are then described by $\tilde{s} \in]0, 2[$. The practical example of the definition of $\tilde{s}$ is given in Fig. 3.11.

[9] In agreement with the SVEA, the notation has been adapted for $\boldsymbol{\mathcal{E}}(t)$ instead of $\boldsymbol{A}(t)$.

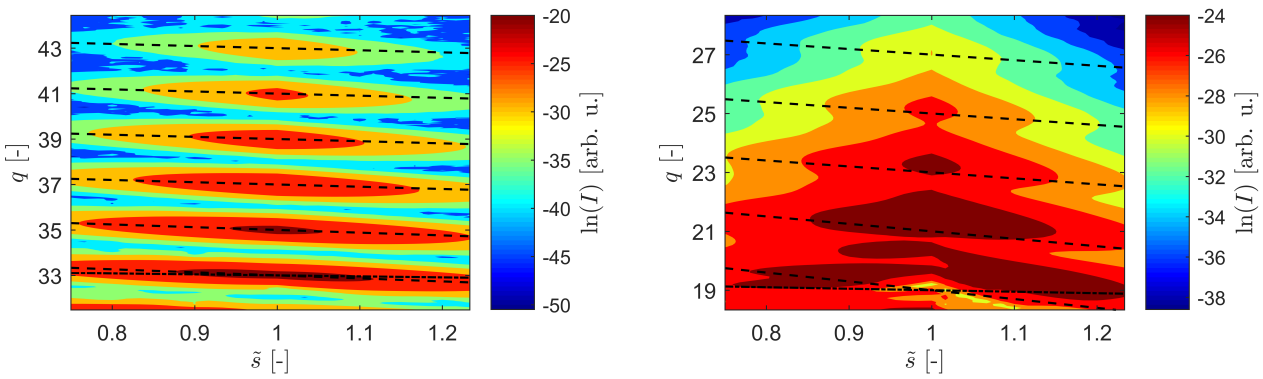

Fig. 3.12: The frequency shifts as functions of $\tilde{s}$ values. The right figure shows results from 20-cycle-pulse and short-pulse-delay simulation and the right one 10-cycle-pulse and long-pulse-delay simulation (as defined by Eq. (3.22)). The dash-dot line shows the short-trajectory contribution in the region, where the distinction of the trajectory class is meaningful. The values of α_q are in atomic units (computed for the intensities for which $\tilde{s} = 1$): $\alpha_{19}^{(\mathrm{short})} = 1200$, $\alpha_{19}^{(\mathrm{long})} = 7100$, $\alpha_{21} = 6000$, $\alpha_{23} = 4800$, $\alpha_{25} = 4500$, $\alpha_{27} = 4400$, $\alpha_{33}^{(\mathrm{short})} = 2100$, $\alpha_{33}^{(\mathrm{long})} = 6300$, $\alpha_{35} = 5700$, $\alpha_{37} = 4700$, $\alpha_{39} = 4500$, $\alpha_{41} = 4400$, $\alpha_{43} = 4400$. These values have been found by the procedure described in the section 2.3.4. The simulation has been done for $\mathcal{E}_0 = 0.075$ au and the Hydrogen atom.

3.2.6 Polarisation gating: numerical simulations on on the generated-frequency control

The presented mechanism leading to the frequency control will be now studied by numerical simulations. The results are summarised in Fig. 3.12. They compare the simple analytical model, Eq. (3.32), with spectra obtained by the KSPA-based simulations. These two methods agree well in the cut-off regions. Two trajectory classes are occurring in the plateau. However, the value of the α coefficient is different for each of them, thus clear shifts are not reached in the plateau and this region is not investigated for our purposes. Because both simulations are done for different pulse delays, which means also different gate intensity, the role of the factor $\omega_c \mathcal{E}_0^2$ is also verified.

Finally, we have shown that the proposed mechanism can be a way to control the frequency of the generated harmonics.

3.3 Conclusion on the temporal-control model

Firstly, basic characteristics of the polarisation gating have been investigated and the proposed cut-off law, Eq. (3.26), has been verified. The original idea of the polarisation gating lies on the study of HHG in elliptical fields that had been precedently discussed in the section 3.2.1. Next, an example of a more-advanced-PG application has been shown–the way of the XUV-frequency control. This shows that our model is able to provide an advanced study of the microscopic response.

In addition, we have seen the Gabor transform may be a very useful for investigating details about the XUV generation process.

4. SPATIAL-PROFILE CONTROL–MACROSCOPIC MODEL

The macroscopic aspects of HHG will be investigated in this chapter. This part of the HHG theory studies the macroscopic XUV field found by summing all the microscopic responses in a generating medium. In general, it demands for: 1–computing the propagation of the IR-field in the medium, 2–the microscopic response is calculated in every point in the medium, 3–the responses are the source terms for propagation equations describing the XUV-field. It is difficult to include all these steps for an arbitrary medium and IR-field.

Our work is inspired by the experimental observations that were made at the CELIA laboratory in 2016. The HHG in a *thin target* was studied as a function of the target position with respect to the focus of the IR-beam. The schematic of this experiment is presented in Fig. 4.1. We will try to make a model based on this special configuration that simplifies the general procedure described in the paragraph above.[1]

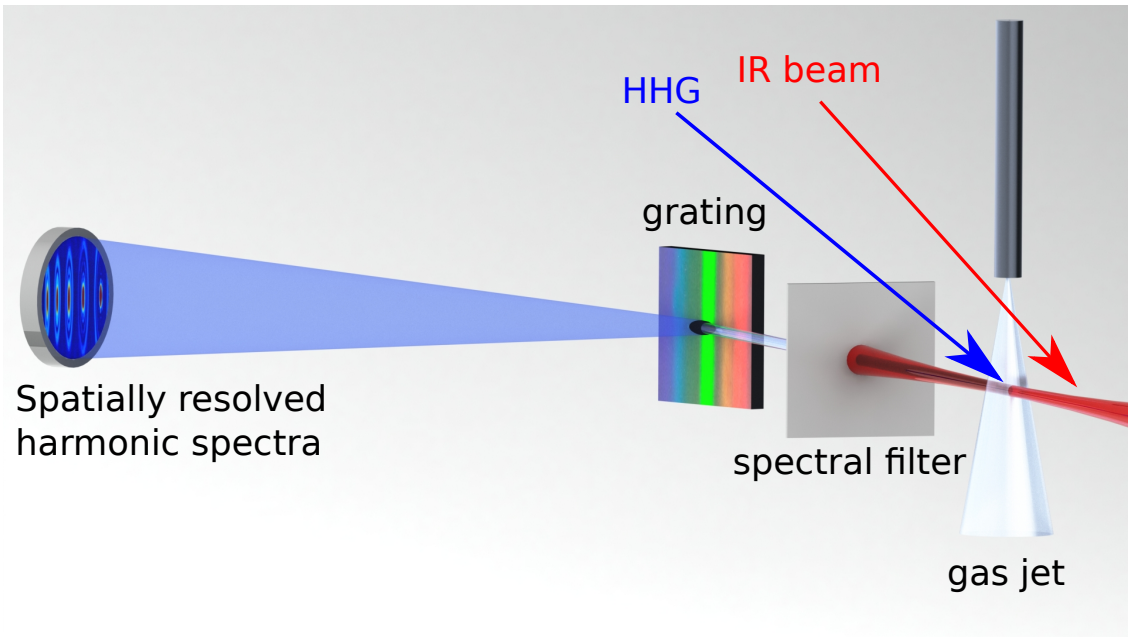

Fig. 4.1: The experimental schematic. The IR-beam on the right side passes through a gas jet that is represented by the semi-transparent cone. The harmonic beam is generated there and both beams propagates together since the spectral filter (the grey plate) that absorbs the IR-radiation. Next, individual harmonics are separated from the harmonic beam on the grating and they are scattered on the observational screen. The author kindly thanks Fabrice Catoire for the figure.

[1] Concretely, it will be shown that the thin target allows to contract its longitudinal dimension and most features are explained only considering it as a radiating plane. The longitudinal problem for thick targets is still a very challenging one nowadays. It is especially the case for growing laser facilities such as ELI-Beamlines and ELI-ALPS. This problem is called the *longitudinal phase-matching*. One case is the *perfect phase-matching* if all the microscopic responses contribute with the same phase and thus interfere constructively in the best possible way. It is called the *quasi-phase-matching* if they just interfere constructively. This issue is not treated in this work at all. An overview is provided in the References [12, 13, 14, 15, 16].

The organisation of this chapter is the following: the theory needed to explain the phenomenon is introduced. Next, created mathematical models are presented and their results are compared with experimental data.

4.1 Theoretical description

In this section we present how the modelling of the spatial evolution of HHG is performed. This evolution is imposed by the macroscopic properties of the IR-field which has to be specified. The IR-laser beam is described by a Gaussian beam. The defining parameters are the pulse duration τ, the beam waist at focus w_0 and the peak-electric field amplitude $\mathcal{E}_0$. We use the standard notation for the envelope

$$\mathcal{E}^{(0)}_{\mathrm{IR}}(\boldsymbol{r},t) = \mathcal{E}_0(t)\frac{w_0}{w(z)}\mathrm{e}^{\left(\frac{\mathbf{i}k}{2R(z)}-\frac{1}{w^2(z)}\right)\rho^2-\mathbf{i}\phi_G(z)}, \qquad \begin{aligned} w(z) &= w_0\sqrt{1+\left(\frac{z}{z_R}\right)^2}, \quad R(z) = z+\frac{z_R^2}{z}, \\ \phi_G(z) &= \arctan\left(\frac{z}{z_R}\right), \qquad z_R = \frac{\pi w_0^2}{\lambda}, \end{aligned} \tag{4.1}$$

k is the wave-number, $\mathcal{E}_0(t)$ is the envelope in time. The full field is then by $\mathcal{E}_{\mathrm{IR}}(\boldsymbol{r},t) = \mathcal{E}^{(0)}_{\mathrm{IR}}(\boldsymbol{r},t)\mathrm{e}^{-\mathbf{i}(\omega_0 t-kz)}$.[2] An example of a Gaussian-beam-waist evolution as a function of z is provided in Fig. 4.2. An important beam characteristic is the Rayleigh length, z_R, where the intensity, I, reaches one half of the maximal intensity, the waist of the beam is $\sqrt{2}w_0$ there and the radius of curvature, $R(z_R)$, is minimal.

The origin of the coordinate system is chosen as the focus of the beam. A gas jet considered as a thin target is placed at z_0 with respect to the focus point of the IR-beam. The IR-laser beam is interacting with the gas jet and generates harmonics that are analysed on a screen placed at a distance D from the thin target. The next step is to account for the spatial distribution of the generated harmonic field.

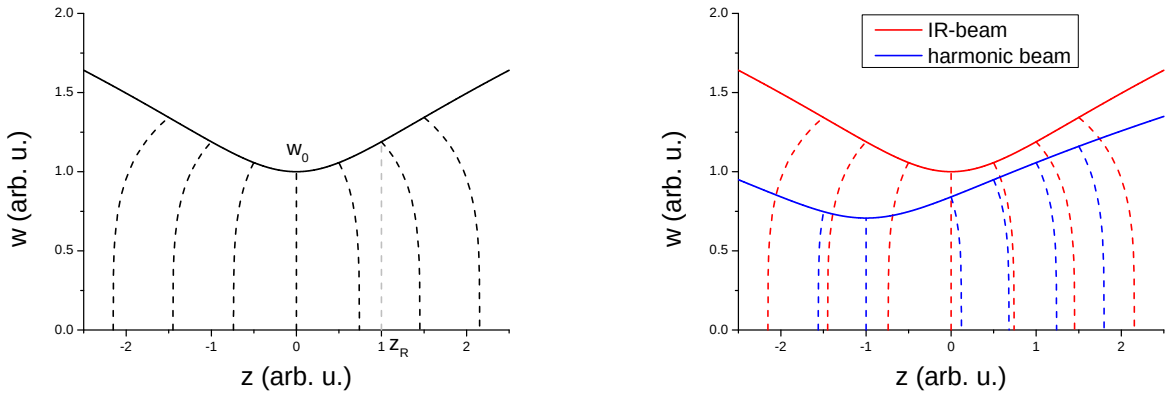

Fig. 4.2: The left figure shows a general Gaussian beam. An important characteristic is the Rayleigh length, where $w(z_R) = \sqrt{2}w_0$, and the curvature reaches its maximum. The left figure shows the harmonic beam in the case where the right-hand side of Eq. (4.17) is zero in z_0. The divergence of the generated field is smaller in that configuration.

[2] Only a linearly polarised field is considered in this section. But there is no difficulty in adding a polarised light using the same procedure as in the previous chapter.

4.1.1 HHG in thin media

Having introduced all the theoretical tools for the XUV generation from the microscopical point of view in the chapter 2, the free-space propagation of the XUV field is the next step. The description directly follows [17] and references therein. The generated XUV field is given by (see [18], Eq. (9.3))

$$\mathcal{E}_g(\omega,\boldsymbol{r}') = (k_\omega^{(0)})^2 \int_{\Delta_\mathrm{T}} \frac{\mathrm{e}^{\mathbf{i}k_\omega\|\boldsymbol{r}-\boldsymbol{r}'\|}}{\|\boldsymbol{r}-\boldsymbol{r}'\|} P(\omega,\boldsymbol{r})\,\mathrm{d}^3x\,, \qquad P(\omega,\boldsymbol{r}) = 2N_0(\boldsymbol{r})d_\omega(\boldsymbol{r})\mathrm{e}^{-\mathbf{i}\frac{\omega}{\omega_0}\varphi_\mathrm{IR}(\boldsymbol{r})}\,, \tag{4.2}$$

where ω_0 is the frequency of the fundamental field, φ_IR is the spatial distribution of the IR-phase, N_0 the density of the gas and Δ_T is the volume defined by the interaction region. $d_\omega(\boldsymbol{r})$ is the elementary dipole in the frequency domain as defined by Eq. (2.12). The dipole is computed for a single active electron, however, there are two in the valence orbital of the target under our consideration. The generation is supposed to be weak enough so that both fields can be taken independently and it gives the factor 2 in the expression for P. Due to the cylindrical symmetry of the IR-beam spatial distribution, we will be using also cylindrical coordinates (ρ,θ,z). The notation is chosen in the following way: primed coordinates describe points on the observation screen and the unprimed ones in the target. Since the distance between the screen and the interaction region is large ($|x-x'|$ and $|y-y'|$ are much smaller than $|z-z'|$ in Cartesian coordinates), the norm can be approximated:

$$\begin{aligned}\|\boldsymbol{r}-\boldsymbol{r}'\| = \sqrt{(x-x')^2+(y-y')^2+(z-z')^2} = |z-z'|\sqrt{1+\frac{(x-x')^2+(y-y')^2}{(z-z')^2}} \approx \\ \approx |z-z'|\left(1+\frac{(x-x')^2+(y-y')^2}{2(z-z')^2}\right)\,.\end{aligned} \tag{4.3}$$

The problem is cylindrically symmetric. The coordinate system can be chosen in order to have $\boldsymbol{r}' = (\rho',0,z')$ and $\boldsymbol{r} = (\rho\cos\theta,\rho\sin\theta,z)$, components are in the Cartesian coordinates. In these coordinates, the norm is[3]

$$\|\boldsymbol{r}-\boldsymbol{r}'\| \approx z'-z+\frac{2\rho\rho'\cos\theta}{z'-z}-\frac{(\rho')^2+\rho^2}{2(z'-z)}\,. \tag{4.4}$$

Then, the term $\frac{\rho^2}{2(z'-z)}$ is discarded because also the radial dimension of the source is much smaller than its distance from the observation plane. However the same is not true for ρ'. This is exactly the *Fraunhofer diffraction* used for finding the field in the far-field region, see [19]. The exponential is then

$$\mathrm{e}^{\mathbf{i}k_\omega\|\boldsymbol{r}-\boldsymbol{r}'\|} \approx \mathrm{e}^{\mathbf{i}k_\omega(z'-z)}\mathrm{e}^{-\mathbf{i}k_\omega\frac{(\rho')^2}{z'-z}}\mathrm{e}^{\mathbf{i}\frac{k_\omega\rho\rho'\cos\theta}{z'-z}}\,. \tag{4.5}$$

Inserting this expansion, using also the expansion in the zeroth order in the denominators and assuming thin target, i.e. $(z'-z)=D$, the generated field is

$$\mathcal{E}_g(\boldsymbol{r}') \approx \frac{\mathrm{e}^{\mathbf{i}k_\omega z'}\mathrm{e}^{\mathbf{i}\frac{k_\omega(\rho')^2}{D}}(k_\omega^{(0)})^2}{D}\int_{\Delta_\mathrm{T}} \mathrm{e}^{-\mathbf{i}k_\omega z}P(\omega,\boldsymbol{r})\mathrm{e}^{\mathbf{i}\frac{k_\omega r r'\cos\theta}{D}}\rho\,\mathrm{d}\theta\,\mathrm{d}\rho\,\mathrm{d}z\,. \tag{4.6}$$

The polarisation of the medium P is cylindrically symmetric and thus θ-independent, i.e. $P(\omega,\boldsymbol{r}) = P(\omega,\rho,z)$. Assuming moreover a thin medium and uniform gas density N_0, the evolution of the elementary dipole, d_ω, as a function of z is negligible and the polarisation is then $P = 2N_0 d_\omega(\rho)\mathrm{e}^{\mathbf{i}(k_\omega^{(0)}z-\frac{\omega}{\omega_0}\varphi_\mathrm{IR}(z,r))}$. Using the Gaussian beam, Eq. (4.1), the IR-phase,

$$\varphi_\mathrm{IR}(\rho,z) = \varphi_\mathrm{IR}^\perp(\rho,z)+\varphi_\mathrm{IR}^\parallel(z)\,, \qquad \begin{aligned}\varphi_\mathrm{IR}^\perp(\rho,z) &= \frac{k_0\rho^2}{2R(z)}\,,\\ \varphi_\mathrm{IR}^\parallel(z) &= \phi_G(z)\end{aligned} \tag{4.7}$$

[3] The observation plane is placed in the direction of the z-axis in our coordinate system, i.e. $z' > z$.

is decomposed to its longitudinal, $\varphi_{\mathrm{IR}}^{\parallel}$, and radial component, $\varphi_{\mathrm{IR}}^{\perp}$. Under our conditions, the evolution in z of $\varphi_{\mathrm{IR}}^{\perp}$ is negligible and it can be approximated by $\varphi_{\mathrm{IR}}^{\perp}(\rho, z_0)$ where z_0 is the position of the target. See [17] for a detailed discussion. Next, the integral over θ in Eq. (4.6) can be carried out using Eq. (B.11). Finally, the generated field is given by

$$\mathcal{E}_g(\rho') \approx \frac{4\pi N_0 \mathrm{e}^{\mathbf{i}\frac{k_\omega(\rho')^2}{D}} \mathrm{e}^{\mathbf{i}k_\omega z'} (k_\omega^{(0)})^2}{D} \int_{\Delta_{\mathrm{T}}^{(z)}} \mathrm{e}^{\mathbf{i}\left(\Delta k_\omega z + \frac{\omega}{\omega_0}\varphi_{\mathrm{IR}}^{\parallel}(z)\right)} \,\mathrm{d}z \cdot \int_{\Delta_{\mathrm{T}}^{(r)}} d_\omega(\rho) \mathrm{e}^{-\mathbf{i}\frac{\omega}{\omega_0}\varphi_{\mathrm{IR}}^{\perp}(\rho, z_0)} J_0\left(\frac{k_\omega \rho \rho'}{D}\right) \rho \,\mathrm{d}\rho =$$

$$= \mathscr{P}(\omega, \Delta_{\mathrm{T}}, D) \int_0^{+\infty} d_\omega(\rho) \mathrm{e}^{-\mathbf{i}\frac{\omega}{\omega_0}\varphi_{\mathrm{IR}}^{\perp}(\rho, z_0)} J_0\left(\frac{k_\omega \rho \rho'}{D}\right) \rho \,\mathrm{d}\rho\,, \tag{4.8}$$

where J_0 is the Bessel function of the first kind, $\Delta k_\omega = k_\omega^{(0)}(n-1)$ with n being the index of refraction of the medium at frequency ω. The separation in the radial and longitudinal component allows to define the pre-factor $\mathscr{P}$, accounting for longitudinal phase-matching, that has no influence on the spatial distribution of a given harmonic on the observation screen. $\Delta_{\mathrm{T}}^{(z)}$ and $\Delta_{\mathrm{T}}^{(\rho)}$ stand for longitudinal and radial dimension, respectively, of the target Δ_{T}. The model uses $\left\|\Delta_{\mathrm{T}}^{(\rho)}\right\| = +\infty$, but the limit of radial integration does not play role if the driving beam is smaller than the target. Then, the integral is nothing but the zeroth order Hankel transform of P (see Eq. (B.10)). The thinness of the target is compared with the parameters of the beam, namely the longitudinal dimension of the target of the target is $\left\|\Delta_{\mathrm{T}}^{(z)}\right\| \ll z_R$.

Having the elementary dipoles computed for each value of the field amplitude $\mathcal{E}$, i.e. $d_\omega = d_\omega(\mathcal{E})$. The integration over r is strictly equivalent to integrate over values of the electric field since for a Gaussian beam $\mathcal{E}(\rho) = \mathcal{E}_0 \mathrm{e}^{-\zeta\rho^2}$. A simple transformation of Eq. (4.8) leads to

$$\mathcal{E}_g(\rho') = \mathscr{P}(\omega, \Delta_{\mathrm{T}}, D) \int_0^{\mathcal{E}_0} \frac{N_0}{\zeta} d_\omega(\mathcal{E}) \mathrm{e}^{-\mathbf{i}\frac{\omega}{\omega_0}\varphi_{\mathrm{IR}}(r(\mathcal{E}), z_0)} J_0\left(\frac{k_\omega \rho' \rho(\mathcal{E})}{D}\right) \frac{\mathrm{d}\mathcal{E}}{\mathcal{E}}\,, \quad \rho(\mathcal{E}) = \sqrt{\frac{1}{\zeta}\ln\left(\frac{\mathcal{E}_0}{\mathcal{E}}\right)}\,. \tag{4.9}$$

Let us consider a simplified case where the dipole $d_\omega = d_\omega(q, \mathcal{E}_0)$ can be expressed analytically using Eq. (2.36) for a given harmonic order q. This formula has been obtained assuming a constant infinite envelope in time. Assuming a diabatic evolution of the dipole with the envelope, i.e. the envelope varies slowly enough that the dipole as a function of the amplitude follows the envelope and the response in every cycle can be taken as the response for a field with the same constant constant amplitude. The time-dependent dipole becomes $d = d(q, \mathcal{E}_0(t))$ for the given harmonic order q and class of trajectory. The frequency dependence of this dipole is then obtained by

$$d_\omega \propto \int_{-\infty}^{+\infty} \mathrm{e}^{\mathbf{i}\omega t} d(q; \mathcal{E}_0(t)) \,\mathrm{d}t\,, \tag{4.10}$$

see Appendix C. It has to be noticed that ω is defined for values centred on the harmonic order. The spatial distribution of the corresponding harmonic field is obtained by calculating Eq. (4.8).

An advantage of this method is that it distinguishes far-field contributions from different trajectories and thus we can obtain an insight into physical processes. However, a completely coherent solution is prevented by the inapplicability of the full SPA in the intermediate region between the cut-off and plateau region. The dipole $d(q; \mathcal{E}_0(t))$ as a function of t always goes through the intermediate region if the studied harmonic q is generated in the plateau in the maximum of $\mathcal{E}_0(t)$. This is usually the case interesting for applications. One can try to construct a model anyway by a smooth connection of valid solutions. This issue will be discussed in the Result section.

4.1.2 Gaussian model of the high harmonics spatial distribution

Complementary to the previous model. A qualitative analysis of the phenomenon will be done using Gaussian beams for both the IR and generated field. First, a general theory of the propagation of Gaussian beams will be introduced and applied to our problem then.

4.1.2.1 The ABCD propagation of Gaussian beams

A full information about a Gaussian beam in one plane perpendicular to its propagation direction at the point z can be obtained from the complex parameter $\mathscr{Q}$ [20],[4] that is defined by

$$\frac{1}{\mathscr{Q}_z} = \frac{1}{R(z)} - \mathbf{i}\frac{\lambda}{\pi w^2(z)}\,. \tag{4.11}$$

R is the radius of curvature of the beam wavefront, w is the beam waist, i.e. the radius where the intensity is equal to $\frac{1}{\mathrm{e}^2}$ of the on-axis intensity. The advantage of this formalism is that the evolution of $\mathscr{Q}$ from an initial state, $\mathscr{Q}^{(i)}$, to a final state, $\mathscr{Q}^{(f)}$, is given by

$$\mathscr{Q}^{(f)} = \frac{A\mathscr{Q}^{(i)} + B}{C\mathscr{Q}^{(i)} + D} \tag{4.12}$$

for a linear optical system described by the matrix $\left(\begin{smallmatrix} A & B \\ C & D \end{smallmatrix}\right)$. The indices i and f denote the initial and final values, respectively. The free propagation matrix is $\left(\begin{smallmatrix} 1 & d \\ 0 & 1 \end{smallmatrix}\right)$, where d is the propagation distance. We find the formula

$$\mathscr{Q}_{z_0+d} = \mathscr{Q}_{z_0} + d \tag{4.13}$$

for propagation from z_0 to $z_0 + d$.

As stated above, a Gaussian beam is fully defined by the parameter $\mathscr{Q}_{z_0}$ at a given point z_0 (Eq. (4.11)). For the analysis, the parameters of the Gaussian beam (w_0, z_R and the position of the focal point) are needed. Using Eqs. (4.11) and (4.13), one obtains

$$w^2(z_0+d) = \frac{\pi^2 w^4(z_0)\left(R(z_0)+d\right)^2 + d^2\lambda^2 R^2(z_0)}{\pi^2 R^2(z_0) w^2(z_0)}\,. \tag{4.14}$$

The minimization of that function with respect to d gives the focal point in the position $z_0 + d_f$. Next, we use the definition of the Gaussian beam, Eq. (4.1), and we find the waist and Rayleigh length. All these results are

$$d_f = -\frac{R(z_0)}{1+\left(\frac{\lambda R(z_0)}{\pi w^2(z_0)}\right)^2}\,, \quad w_0^2 = w_0^2(z_0+d_f) = \frac{w^2(z_0)}{1+\left(\frac{\pi w^2(z_0)}{\lambda R(z_0)}\right)^2}\,, \quad z_R = \frac{\pi\lambda R^2(z_0) w^2(z_0)}{\lambda^2 R^2(z_0) + \pi^2 w^4(z_0)}\,. \tag{4.15}$$

4.1.2.2 The generated field as a Gaussian beam

The qualitative insight into the origin of the spatial distribution can be obtained from the theory of Gaussian-beam propagation and from Eq. (2.36). We are analysing the generated field for a given harmonic order q. Let us look at the radial distribution of the field modulus and phase, that defines the beam radius and curvature, respectively. The field modulus follows the law $|\mathcal{E}_q| \propto |\mathcal{E}_{\mathrm{IR}}|^{q_{\mathrm{eff}}}$, thus the beam waist of the harmonic q is $w_q(z_0) = w(z_0)/\sqrt{2q_{\mathrm{eff}}}$. The spatial distribution of the phase is the sum of the IR-beam phase and the additional intensity dependent phase ($-\alpha I_{\mathrm{IR}}$). The intensity distribution in the first order expansion is

$$I_{\mathrm{IR}}(\rho) = \left(\frac{w_0}{w(z_0)}\right)^2 I_0 \mathrm{e}^{-\frac{2\rho^2}{w^2(z_0)}} \approx \left(\frac{w_0}{w(z_0)}\right)^2 I_0 - \frac{2w_0^2 I_0 \rho^2}{w^4(z_0)}\,, \tag{4.16}$$

[4] We denote the parameter by the calligraphic $\mathscr{Q}$ because we already use q for the harmonic order.

the intensity profile has been obtained from Eq. (4.1). Substituting this expansion in Eq. (2.36) and adding the IR-beam phase, we find the effective curvature, R_q, of the harmonic q as a solution of

$$\frac{k_q\rho^2}{2R_q(z_0)} = \frac{k_q\rho^2}{2R(z_0)} - \alpha I_{\mathrm{IR}}(\rho) \approx \frac{k_q}{2}\left(\frac{1}{R(z_0)} + \frac{4\alpha w_0^2 I_0}{k_q w^4(z_0)}\right)\rho^2 \quad \Rightarrow \quad \frac{1}{R_q(z_0)} \approx \frac{1}{R(z_0)} + \frac{4\alpha w_0^2 I_0}{k_q w^4(z_0)}\,. \tag{4.17}$$

Finally, the waist, w_q, of the harmonic q is found inserting the proper curvature and waist in Eq. (4.14):

$$w_q^2(z_0+d) = \frac{\pi^2 w_q^4(z_0)\left(R_q(z_0)+d\right)^2 + d^2\lambda_q^2 R_q^2(z_0)}{\pi^2 R_q^2(z_0) w_q^2(z_0)}\,, \tag{4.18}$$

where λ_q and R_q are the wavelength of the harmonic field and radius of curvature respectively and d is the distance from the studied plane.

The physics coming from that model, so as an analytical implementation in Mathematica® and comparison with experiments will be discussed in the result section 4.2.1.

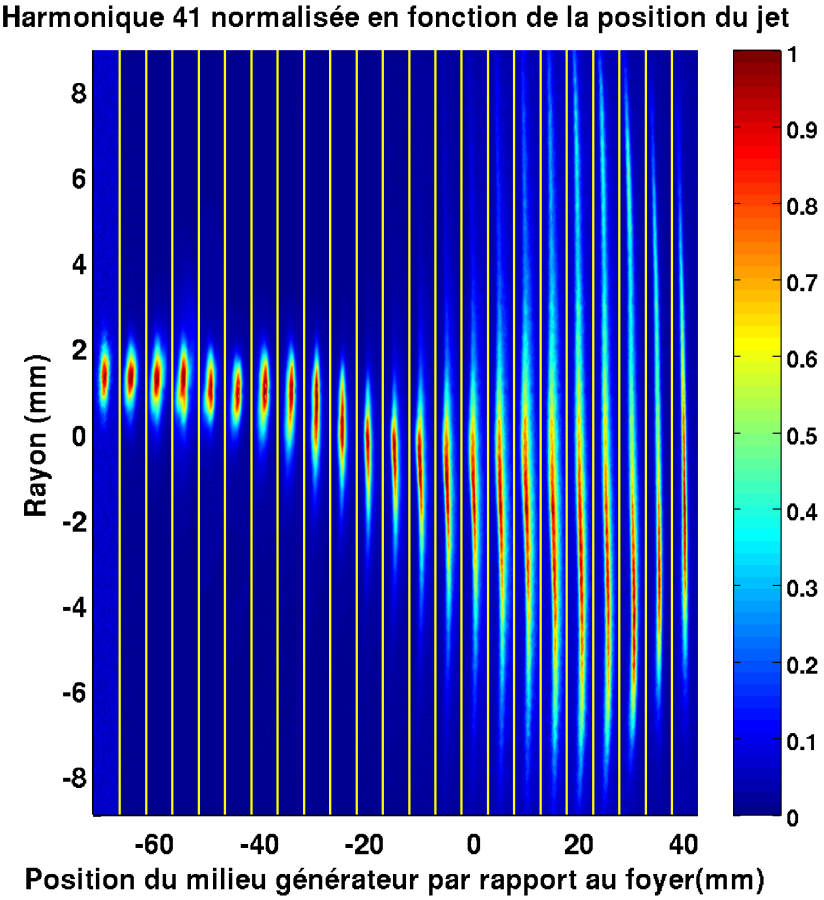

Fig. 4.3: The experimental results of the spatial distribution of the harmonic 41 generated in a thin target. The graph represents normalised spot-sizes (the y-axis represents spatial coordinate on the screen in mm) as a function of the jet position with respect to the IR-beam focus placed in zero. The spots are not centred around zero due to experimental issues. One sees that the minimum of the divergence is reached for the jet placed before focus. See text for the experimental parameters. The author kindly thanks Ludovic Quintard for the figure.

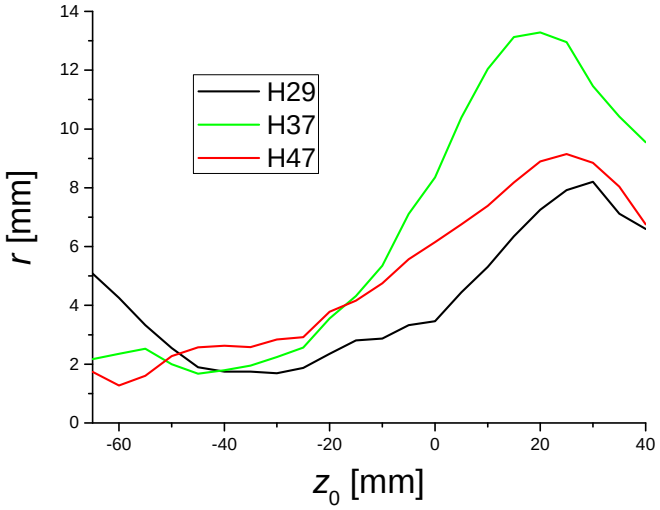

Fig. 4.4: Experimental results of the FWHM as a function of the jet position z_0. The experiment was done in the Neon target. The author kindly thanks Ludovic Quintard who has provided the experimental data.

4.2 Results

Before proceeding to our mathematical analysis, the experimentally measured data from CELIA will be presented. A thin-target-IR-laser interaction was studied as a function of the target position with respect to the focus of the IR-beam (see the schematic in Fig. 4.1). The target was a Neon jet for this set of experiments. The dependence of the FWHM on the jet position is traced in Fig. 4.4 for harmonics 29, 37 and 49. Figure 4.3 shows a more detailed scan for the harmonic 41. The results show that the divergence of the generated beam is smaller for negative z_0 and also that the position of the jet for the minimal divergence, $z_{\min}$, is farther from the focus for higher harmonics. The value of $z_{\min}$ is an important characteristic of the experiment because a reduction of the XUV-beam divergence increases its peak intensity, thus also the number of photons.

In our work, we have developed a model both for the physical understanding of the process and for its quantitative simulation. Additionally, we would also like to find the optimal position of $z_{\min}$. We start the study with the qualitative Gaussian model (section 4.1.2.2) and it will continue by the Hankel transform (introduced by Eq. (4.8)) with various dipoles, namely Eqs. (2.36), (2.33) and (2.17). For all the simulations, the parameters $w_0 = 96$ μm, $\mathcal{E}_0 = 0.125$ a.u. and $\tau = 40$ fs were used, as it was measured in the experimental setup supposing the IR-field with a Gaussian profile.

The microscopic model for Ne atoms is required according to the experiment. The target potential is modelled by the Gaussian model introduced in the Appendix B.6.2.1. Needed to mention that we have confirmed that the action, Eq. (2.10), has the leading role in the dipole calculations and the exact form of the transition-dipole matrix elements, Eq. (2.5), is not so important in our conditions.

In this point, we need to explain the notation. All the results are studied on the observation plane that was placed 3 m after the focus in the experiment. A plane placed in the same distance from the source is used to evaluate the field in our simulations and the radial distance from the z-axis on that plane is denoted by r. This way allows an easy comparison with the experimental data. However, it is placed in the far-field region in the used model and the divergence can be more meaningful from the theoretical point of view. The conversion is given by $\theta = \arctan\left(\frac{r[\mathrm{m}]}{3}\right)$ for a divergence angle θ.

4.2.1 *Gaussian model*

The Gaussian model, section 4.1.2.2, provides a basic physical explanation of the mechanism. Let us focus on Eq. (4.17). The IR-beam curvature, $R(z)$, is positive for $z_0 > 0$, as well as the contribution from the microscopic dipole. For opposite value of z_0, the geometrical phase due to the IR beam is negative but the contribution from the dipole remains positive. It is easy to show that the curvature of the generated beam is always greater for $z_0 > 0$. This explains why the spot in the far-field is smaller if the jet is placed in $z_0 < 0$.[5]

In order to obtain a focusing XUV beam (or more precisely a beam with the minimal divergence), the contributions for the microscopic dipole and geometrical phase have to compensate each other. An analytical model was built up in Mathematica®. It is based directly on Eq. (4.18). Results for chosen values of model parameters are shown in Fig. 4.5. The Mathematica® worksheet containing the model is also attached to this work. The found dependencies show, consistently with the expectations from the previous paragraph, that the harmonic beam is less divergent if the jet is placed before the IR-focus. As it is illustrated in Fig. 4.2, the opposite effect is observed on the other side of the IR-focus.

A further study proved that changing the parameters q and α have the opposite effect for the position of $z_{\min}$, i.e. an increment of q moves $z_{\min}$ closer to zero so as a decrement of α, and vice versa. This exactly corresponds to the additional-curvature contribution that is given by the last term in Eq. (4.17), since it behaves like $\frac{\alpha}{q}$, $(k_q = qk_0)$. The experiment demonstrates that $z_{\min}$ is farther from zero for higher harmonic which indicates that the effect of α (and of the phase in general) is dominant.

Despite the fact the model uses many oversimplifications and it is not applicable at all to describe the intermediate region in the spectrum between the plateau and cut-off, it provides the recognition of the roles of different terms.

4.2.2 *FSPA dipole*

All the approaches until this point uses the numerical evaluation of the Hankel transform, Eq. (4.9). First, the dipole computed by the FSPA, Eq. (2.33), has been used. However, as it was discussed in the section 2.3.4, the transition between the plateau and cut-off in the spectrum is not treated well using the proposed model because the presented FSPA is not valid there. In order to avoid this problem, we assumed a smooth transition

[5] A further classification for different harmonic orders is not straightforward, because α is harmonic-order dependent.

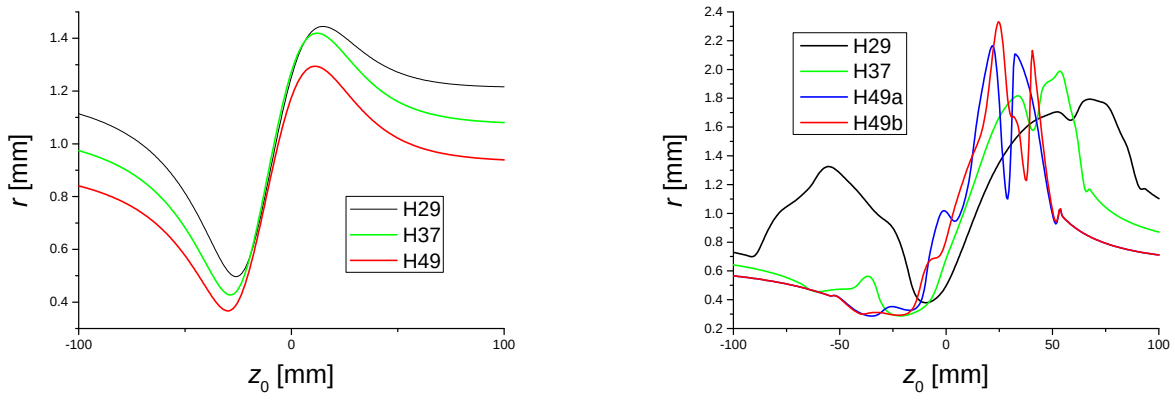

Fig. 4.5: Values of the FWHM obtained from our models. The results from the Gaussian model are in the left figure, chosen parameters are $\alpha_{29} = 2.3 \cdot 10^{-14}$ cm$^2 \cdot$ W^{-1}, $q_{\text{eff}}{}^{(29)} = 7$, $\alpha_{37} = 3.5 \cdot 10^{-14}$ cm$^2 \cdot$ W^{-1}, $q_{\text{eff}}{}^{(37)} = 9$ and $\alpha_{49} = 5 \cdot 10^{-14}$ cm$^2 \cdot$ W^{-1}, $q_{\text{eff}}{}^{(49)} = 12$. The FSPA results are shown on the right one. The H49a shows the result with the interpolated phase and the H49b shows the original one.

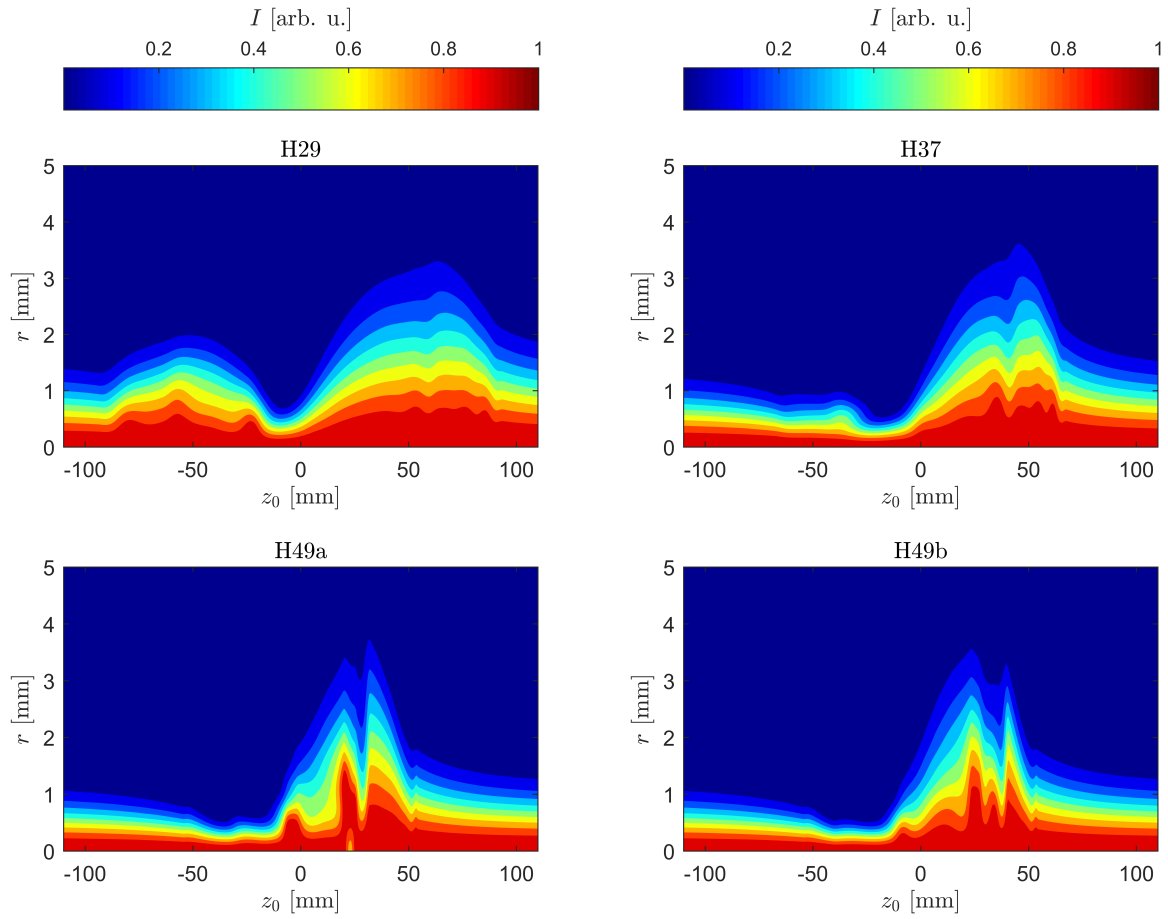

Fig. 4.6: The evolution of the waist of the harmonics in far-field as a function of the jet position z. H49a shows distribution with the phase interpolated by a Lagrange polynomial while H49b uses the formal solutions in the whole region.

between the plateau and cut-off therefore we have employed an interpolation by a Lagrange polynomial using points on both sides of the intermediate region.

Next, the contributions coming from the short- and long-trajectories are separated in that model. Both classes have been studied separately and the short-trajectories have been recognised as the higher contribution. The explanation is the following: the fast oscillating phase evolution as a function of the IR-field intensity (see Fig. 2.3) causes spatial diffraction of the long-trajectory contribution of the harmonic radiation. Due to this reason, only the short-trajectories results are discussed in this section thereafter.

Our results for harmonics 29, 37 and 49 are summarized in Figs. 4.5, 4.6 and 4.7. There is also traced H49b in Fig. 4.6 that uses the phase without the Lagrange polynomial. This two-phase difference is traced in Fig. 4.8. Even though we can hardly see the difference in the figure and there is only a small deviation around $I = 0.008$ a.u., the change is notable in Fig. 4.6 and especially in the case of FWHM, the effects are almost opposite in the region $z_0 \in]30, 40[$ mm (Fig. 4.7). This shows an extreme sensitivity of the model on the proper description of the dipole phase.[6] The latter figure also proves a perfect coincidence outside the region $z_0 \in]-50, 50[$ mm as it is expected, because the amplitude of the field is not high enough to reach the critical region around $I = 0.008$ a.u. even on the beam axis.

[6] The accuracy in the phase calculations is very important because one has to consider always the phase modulo 2π since it is inserted in a goniometric function.

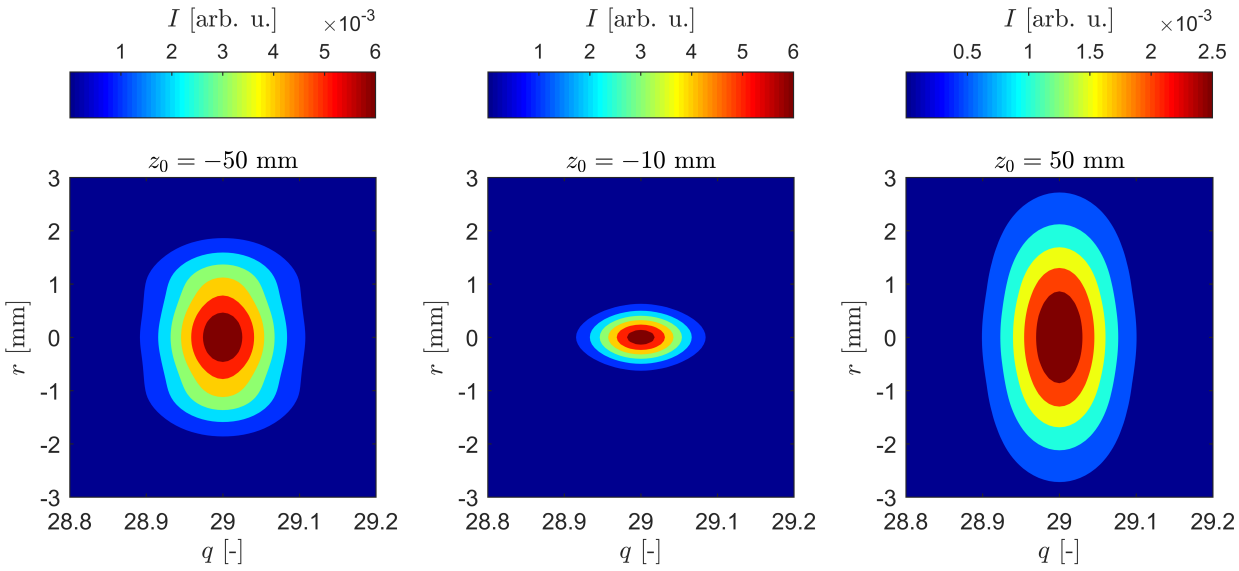

Fig. 4.7: The spatial distribution of the intensity on the observation screen around the 29th harmonic (see Fig. 4.6, H29). z_0 is the position of the gas jet. The scales clearly show that the intensity is the highest for the smallest spot, compare with the non-normalised intensity in Fig. 4.9.

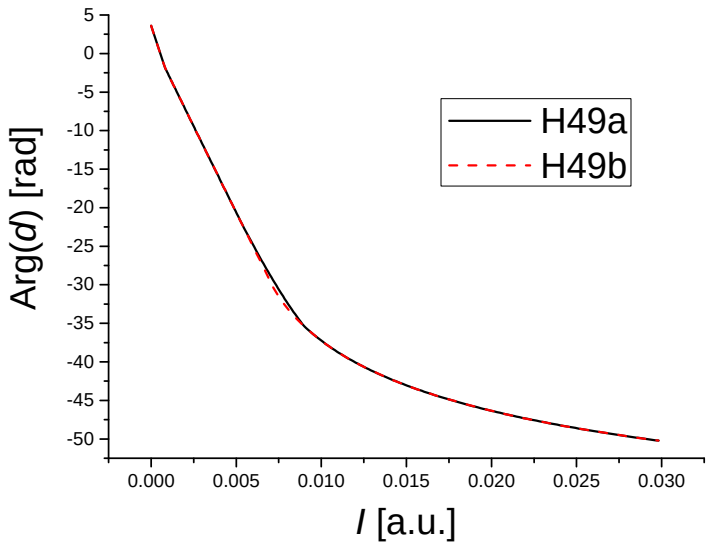

Fig. 4.8: The difference between the phase interpolated by the Lagrange polynomial, H49a, and phase obtained by connection of the long- and short-trajectory solution in their intersection, H49b.

The last presented results are spatial distributions of the harmonic-field intensity (Fig. 4.7). The minimization of the divergence of the harmonic beam for the jet position $z_0 = -10$ mm is showed there for 29th harmonic. The result indicates that there are no significant changes in a spectral width for the parameters under investigation.

Up to now, it is not easy to provide a more sufficient theoretical analysis of the results because we can not distinguish effects caused by numerics and approximations from real ones.[7] It leads us to the necessity of a model that will sufficiently cover the phase evolution in the whole intensity range. To conclude this section, these results have verified that the importance of different classes of trajectories and they have provided a background to the methodology for using more advanced models. The methodology will be discussed before proceeding to the final KSPA model.

4.2.3 Methodology for result processing

Although, a qualitative agreement between the presented simulations and the experiment have been obtained, the retrieved results are still not covering the experimental results completely. The following three factors are considered as a possible limitation:

1. The experimental observations are obtained as the result of many laser shots. The conditions may not be strictly the same throughout the experiments. An important factor may be the IR-intensity variation.

2. The methodology for retrieving the spot-size may play an important role for non-Gaussian spots.

3. The previous models were developed for only one class of trajectory for each IR-field intensity.

The third one is solved automatically in the KSPA, because this theory is not using trajectories at all. In order to solve the others:

1. Focusing on the intensity, let us formally assume that the intensity of the IR-field, I_{IR}, for every shot is a random variable with a probability-distribution function $f_{I_{\mathrm{IR}}}$. The XUV-field, Eq. (4.8) is then a function of that random variable and its value is obtained as the expected value

$$\langle \mathcal{E}_g \rangle = \frac{\int_{-\infty}^{+\infty} \mathcal{E}_g(I_{\mathrm{IR}}) f_{I_{\mathrm{IR}}}(I_{\mathrm{IR}})\,\mathrm{d}I_{\mathrm{IR}}}{\int_{-\infty}^{+\infty} f_{I_{\mathrm{IR}}}(I_{\mathrm{IR}})\,\mathrm{d}I_{\mathrm{IR}}}\,. \tag{4.19}$$

   Practically, the simulations can be run for several intensities around I_0 and the result is their average.

2. Various common definitions of the spot-size are introduced in the appendix D and they will be applied on our results.

[7] For example, the local maximum around $z_0 = -50$ mm for H29 that is not presented for higher harmonic orders.

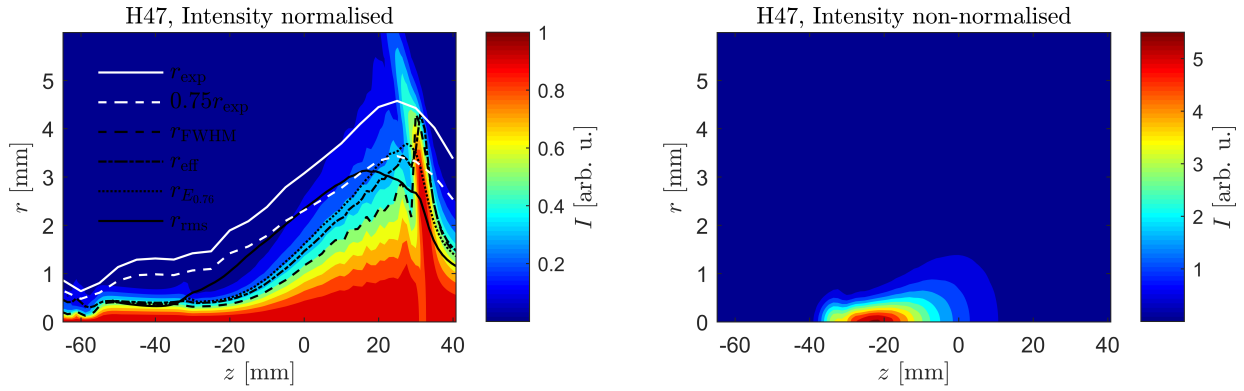

Fig. 4.9: The evolution of the waist of H47 in far-field as a function of the jet position z_0. The left figure shows normalised values for each value of z_0 and the right one non-normalised. Various definitions of the beam-waist are added (black lines) and putted into comparison with the experimental data $r_{\rm exp}$ (see text for further details).

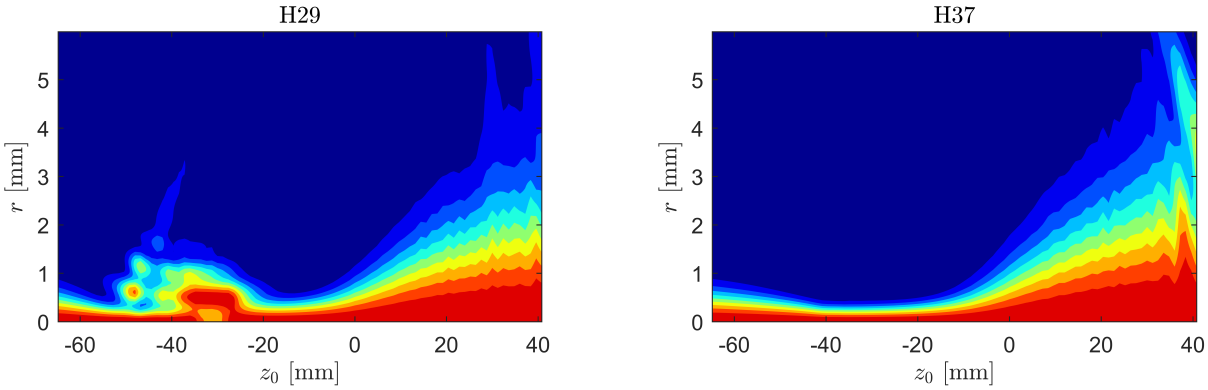

Fig. 4.10: The evolution of the waists for H29 and H37 in far-field as a function of the jet position z_0. The normalisation and scale are the same as in Fig. 4.9.

.

4.2.4 KSPA dipole

Incorporating the previous methodology, the results presenting the beam-spot size as a function of the jet position are shown in Figs. 4.9 and 4.10. The first one focuses on methods for retrieving the spot size putted in a comparison with the experimental data. The best match has been found for the definition $r_{\rm rms}$ and $r_{E_{0.76}}$. Although the experimental data have been processed by a FWHM-based method on the measured intensity, the two mentioned methods may correspond better because they are less sensitive to the fast evolving complex structures present in the distribution obtained by our simulations.

Needed to mention, the effort of the spatial-distribution model is primary to maximise intensity of the produced XUV. Basically, it is affected by two factors: the IR-field intensity in the target and the XUV-beam divergence. For this purpose, Figure 4.9 shows both normalised and non-normalised intensity on the observation screen as a function of the jet position. The global XUV-intensity maximum is reached in the region where the spot-size is almost constant closer to the IR-focus as expected. These results also show that despite of the theoretical importance of the spatial structures for $z_0 > 0$, there are not in the range of our interest for maximising XUV intensity.

Finally, the spot sizes as a function of harmonic order for the jet placed at $z_0 = -30$ mm is in Fig. 4.11. We can see a typical ring structure for long-trajectories (compare as in the results of [17]). The contribution of the long-trajectories is much smaller in intensity than the short-trajectories one (the logarithmic scale is used) but it can play a role, especially for the higher harmonics where these two contributions merge. Next, the rings can be large enough to interfere with neighbouring harmonics and eventually if the interference is constructive, a response in the proper even harmonic can be observed.

4.3 Conclusion on spatially resolved harmonic spectra

In this section, the results from different models have been presented (namely: The Gaussian model, The Hankel transform using the constant values of α and q_{eff}, The Hankel transform using FSPA dipole with interpolation in the intermediate region between the cut-off and plateau, The Hankel transform of the KSPA dipole). We can conclude that basic mechanisms can be understood from very simple ideas (Gaussian model). On the other hand, a very precise analysis is needed for a quantitative models that can be extremely sensitive to input parameters (compare Fig. 4.6 with the phase evolution in Fig. 4.8). By the KSPA model, the experimental results have been approached.

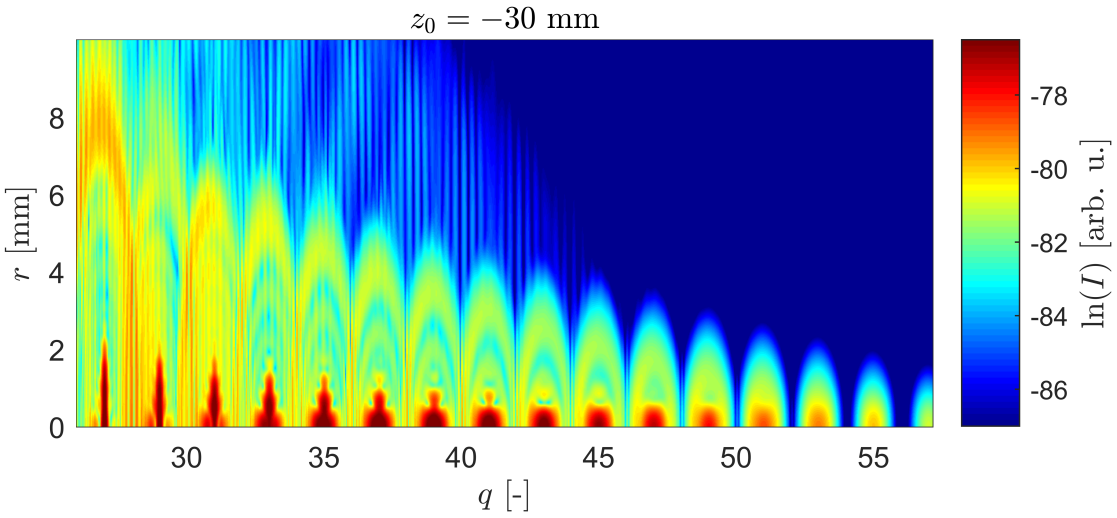

Fig. 4.11: Spatial distribution of the intensity for the jet placed in $z_0 = -30$ mm obtained by the KSPA model.

5. CONCLUSION

This work was dedicated to the study of spatially resolved harmonic spectra generated in thin gaseous media and to the study of the temporal and frequency control of the generated harmonics using the so-called polarisation-gating technique. In connection with experiments performed at CELIA, the control of the spatial and temporal distribution of the harmonics has been studied.

The temporal control has been performed using the superposition of two elliptical delayed counter-rotating short IR pulses. We have shown that controlling the ellipticity of the two IR pulses allows for defining a new cut-off law. We have also presented the influence of the relative amplitude ratio of the two IR fields on the harmonics spectra. In particular the central frequency of the XUV comb is performed by properly choosing the amplitude ratio of the two IR pulses. These results are of prime interest in particular in the context of tomography where controlling the cut-off of harmonics spectra allows for defining a good spatial resolution of the molecular orbitals [2, 21]. Being able to tune the central frequency of the XUV comb will allow for studying the orbitals of large molecules. For this study, the microscopic model has been used which means that only the temporal profile has been considered.

We have also developed a model to take into account the spatial distribution of harmonic spectra. This study has been done for a single linearly polarised IR field in Neon. We have shown that changing the position of the focus point of the IR beam with respect to the gaseous target presents a minimum of divergence in the far-field in agreement with experimental observations. This minimum of divergence has been clearly attributed to a focusing of the XUV beam after the generating medium. This study opens a way for finding configurations where the fluence of the XUV beam can be increased. This beam can then be, in principle, used for studying XUV non-linear processes in gaseous media.

This work studied the problem from the theoretical point of view. The common part for both models is the microscopic dipole. The author developed his own FORTRAN90 code for computing the dipole in KSPA for an IR-field given by two elliptically polarised pulses. This allowed the study of the polarisation gating. Then he has extended codes developed at CELIA for solving the FSPA and Hankel transform used for the spatially resolved harmonic spectra. Finally, he has also created the analytical Gaussian model in Mathematica®. The results obtained by these models have been discussed in the sections 3.2 and 4.2. The figures and graphs were processed in OriginLab, MATLAB®and Mathematica®.

BIBLIOGRAPHY

[1] K. Zhao, Q. Zhang, M. Chini, Y. Wu, X. Wang, and Z. Chang, "Tailoring a 67 attosecond pulse through advantageous phase-mismatch," *Opt. Lett.*, vol. 37, pp. 3891–3893, Sep 2012.

[2] J. Itatani, J. Levesque, D. Zeidler, H. Niikura, H. Pépin, J. C. Kieffer, P. B. Corkum, and D. M. Villeneuve, "Tomographic imaging of molecular orbitals," *Nature*, vol. 432, pp. 867–871, dec 2004.

[3] P. B. Corkum, "Plasma perspective on strong field multiphoton ionization," *Phys. Rev. Lett.*, vol. 71, pp. 1994–1997, Sep 1993.

[4] M. Lewenstein, P. Balcou, M. Y. Ivanov, A. L'Huillier, and P. B. Corkum, "Theory of high-harmonic generation by low-frequency laser fields," *Phys. Rev. A*, vol. 49, pp. 2117–2132, Mar 1994.

[5] M. Ivanov and K. Rzążewski, "Are free-free transitions a good basis for nonlinear optics?," *Journal of Modern Optics*, vol. 39, no. 12, pp. 2377–2381, 1992.

[6] G. B. Arfken, H. J. Weber, and F. E. Harris, *Mathematical Methods for Physicists, Sixth Edition: A Comprehensive Guide*, ch. 7.3. Academic Press, 6 ed., July 2005.

[7] T. Auguste, F. Catoire, P. Agostini, L. F. DiMauro, C. C. Chirila, V. S. Yakovlev, and P. Salières, "Driving-frequency scaling of high-harmonic quantum paths," *New Journal of Physics*, vol. 14, no. 10, p. 103014, 2012.

[8] J.-F. Bonnans, J. C. Gilbert, C. Lemarechal, and C. A. Sagastizábal, *Numerical Optimization: Theoretical and Practical Aspects*, ch. Background, pp. 157–168. Berlin, Heidelberg: Springer Berlin Heidelberg, 2006.

[9] C. Figueira de Morisson Faria, H. Schomerus, and W. Becker, "High-order above-threshold ionization: The uniform approximation and the effect of the binding potential," *Phys. Rev. A*, vol. 66, p. 043413, Oct 2002.

[10] E. W. Weisstein, "Ellipse.," *From MathWorld–A Wolfram Web Resource.*

[11] M. Möller, Y. Cheng, S. D. Khan, B. Zhao, K. Zhao, M. Chini, G. G. Paulus, and Z. Chang, "Dependence of high-order-harmonic-generation yield on driving-laser ellipticity," *Phys. Rev. A*, vol. 86, p. 011401, Jul 2012.

[12] E. Constant, D. Garzella, P. Breger, E. Mével, C. Dorrer, C. Le Blanc, F. Salin, and P. Agostini, "Optimizing high harmonic generation in absorbing gases: Model and experiment," *Phys. Rev. Lett.*, vol. 82, pp. 1668–1671, Feb 1999.

[13] M. Geissler, G. Tempea, A. Scrinzi, M. Schnürer, F. Krausz, and T. Brabec, "Light propagation in field-ionizing media: Extreme nonlinear optics," *Phys. Rev. Lett.*, vol. 83, pp. 2930–2933, Oct 1999.

[14] M. B. Gaarde, J. L. Tate, and K. J. Schafer, "Macroscopic aspects of attosecond pulse generation," *Journal of Physics B: Atomic, Molecular and Optical Physics*, vol. 41, no. 13, p. 132001, 2008.

[15] C. Hernández-García, J. A. Pérez-Hernández, J. Ramos, E. C. Jarque, L. Roso, and L. Plaja, "High-order harmonic propagation in gases within the discrete dipole approximation," *Phys. Rev. A*, vol. 82, p. 033432, Sep 2010.

[16] C. Jin, *Theory of Nonlinear Propagation of High Harmonics Generated in a Gaseous Medium*. Springer Verlag, 2013.

[17] F. Catoire, A. Ferré, O. Hort, A. Dubrouil, L. Quintard, D. Descamps, S. Petit, F. Burgy, E. Mével, Y. Mairesse, and E. Constant, "Complex structure of spatially resolved high-order-harmonic spectra," *Phys. Rev. A*, vol. 94, p. 063401, Dec 2016.

[18] J. D. Jackson, *Classical electrodynamics*. New York, NY: Wiley, 3rd ed. ed., 1999.

[19] E. Hecht, *Optics*, ch. 10.2. Pearson education, Addison-Wesley, 2002.

[20] A. Gerrard and J. M. Burch, *Introduction to Matrix Methods in Optics*, ch. III.6, pp. 116–122. New York: Dover Publications, Inc, 1975.

[21] Z. Diveki, R. Guichard, J. Caillat, A. Camper, S. Haessler, T. Auguste, T. Ruchon, B. Carré, A. Maquet, R. Taïeb, and P. Salières, "Molecular orbital tomography from multi-channel harmonic emission in {N2}," *Chemical Physics*, vol. 414, pp. 121 – 129, 2013. Attosecond spectroscopy.

[22] J. Sakurai and J. Napolitano, *Modern Quantum Mechanics*. —, Addison-Wesley, 2011.

[23] M. Pinsky, *Introduction to Fourier Analysis and Wavelets*, ch. 2.4.3. Brooks/Cole series in advanced mathematics, Brooks/Cole, 2002.

[24] E. W. Weisstein, "Harmonic addition theorem.," *From MathWorld–A Wolfram Web Resource.*

[25] M. Abramowitz and I. Stegun, *Handbook of Mathematical Functions: With Formulas, Graphs, and Mathematical Tables*. Applied mathematics series, Dover Publications, 1964.

[26] A. Messiah, *Quantum Mechanics*, ch. XI. No. v. 1 in Quantum Mechanics, North-Holland, 1981.

[27] C. Bunge, J. Barrientos, and A. Bunge, "Roothaan-hartree-fock ground-state atomic wave functions: Slater-type orbital expansions and expectation values for z = 2-54," *Atomic Data and Nuclear Data Tables*, vol. 53, no. 1, pp. 113 – 162, 1993.

[28] ISO, "Lasers and laser-related equipment – test methods for laser beam widths, divergence angles and beam propagation ratios," ISO 11146-2:2005, International Organization for Standardization, Geneva, Switzerland, 2005.

APPENDIX

A. CONVENTIONS AND DEFINITIONS

There is a review of the physical conventions used in this text. Moreover, some physical consequences are pointed out there.

A.1 Fourier transform

We use the Fourier transform

$$f(\boldsymbol{\xi}) = \mathscr{F}\left[f(\boldsymbol{x})\right](\boldsymbol{\xi}) = \frac{1}{(2\pi)^{\frac{n}{2}}} \int_{\mathbb{R}^n} f(\boldsymbol{x}) \mathrm{e}^{\mathbf{i}\boldsymbol{\xi}\cdot\boldsymbol{x}} \,\mathrm{d}^n x \tag{A.1}$$

for $\boldsymbol{x}, \boldsymbol{\xi} \in \mathbb{R}^n$.

A.2 QM notation, normalization of plane waves

A.2.1 Stationary states

We are using the Dirac braket notation for the description of states in QM. This means that $|\psi\rangle$ is a vector from an abstract space and it is specified by the choice of a representation. We work in the x-representation or p-representation, wave functions in these representations are

$$\psi(\boldsymbol{r}) = \langle \boldsymbol{r}|\psi\rangle \ , \tag{A.2}$$
$$\psi(\boldsymbol{p}) = \langle \boldsymbol{p}|\psi\rangle \ . \tag{A.3}$$

See ([22], chapter 1.7) for a further discussion about the representations.

Under the plane wave is understood the state with a momentum $\boldsymbol{p}$ and it is defined as

$$\psi_{\boldsymbol{p}}(\boldsymbol{r}) = \langle \boldsymbol{r}|\boldsymbol{p}\rangle = \frac{1}{(2\pi)^{\frac{3}{2}}} \mathrm{e}^{\mathbf{i}\boldsymbol{p}\cdot\boldsymbol{r}} \,. \tag{A.4}$$

This choice is the only one consistent with the usual definition of the momentum operator $\hat{\boldsymbol{p}} = -\mathbf{i}\bigtriangledown$. It is because

$$-\mathbf{i} \bigtriangledown \psi_{\boldsymbol{p}}(\boldsymbol{r}) = -\mathbf{i}^2 \boldsymbol{p} \psi_{\boldsymbol{p}}(\boldsymbol{r}) = \boldsymbol{p}\psi_{\boldsymbol{p}}(\boldsymbol{r}) \,. \tag{A.5}$$

Together with the decomposition of the unity it leads to the transformation between the x- and p-representation:

$$\psi(\boldsymbol{p}) = \int_{\mathbb{R}^3} \langle \boldsymbol{p}|\boldsymbol{r}\rangle \langle \boldsymbol{r}|\psi\rangle \ \mathrm{d}^3 x = \frac{1}{(2\pi)^{\frac{3}{2}}} \int_{\mathbb{R}^3} \mathrm{e}^{-\mathbf{i}\boldsymbol{p}\cdot\boldsymbol{r}} \psi(\boldsymbol{r}) \,\mathrm{d}^3 x = \mathscr{F}^{-1}\left[\psi(\boldsymbol{r})\right](\boldsymbol{p}) \,, \tag{A.6}$$

i.e. the representation is changed by the inverse Fourier transform. It also implies the natural expression of the momentum operator in the p-representation: $\hat{\boldsymbol{p}} = \boldsymbol{p}$.

The definition of the plane wave, Eq. (A.4), also defines the normalisation of the momentum eigenfunctions:

$$\langle \boldsymbol{p}|\boldsymbol{p}'\rangle = \delta(\boldsymbol{p} - \boldsymbol{p}') \,. \tag{A.7}$$

A.2.2 Time evolution

In the QM, the evolution in time is driven by the Schrödinger equation,

$$\mathbf{i}\partial_t \left|\psi(t)\right\rangle = \hat{H} \left|\psi(t)\right\rangle \,, \tag{A.8}$$

where $\hat{H}$ is the Hamiltonian describing the system under considerations and it is assumed to be constant in time. The general solution $\left|\psi(t)\right\rangle = \mathrm{e}^{-\mathbf{i}(t-t_0)\hat{H}} \left|\psi(t_0)\right\rangle$ is simple for eigenstates of $\hat{H}$:

$$\left|\psi_E(t)\right\rangle = \mathrm{e}^{-\mathbf{i}(t-t_0)E} \left|\psi_E(t_0)\right\rangle \,, \qquad \hat{H} \left|\psi_E(t_0)\right\rangle = E \left|\psi_E(t_0)\right\rangle \,. \tag{A.9}$$

The plane wave, Eq. (A.4), is such a state for the free-particle Hamiltonian $\hat{H}_F = -\frac{\triangle}{2}$ because it fulfils $\hat{H}_F \psi_{\boldsymbol{p}}(\boldsymbol{r}) = \frac{\boldsymbol{p}^2}{2}\psi_{\boldsymbol{p}}(\boldsymbol{r})$. The free particle is then fully described in space and time by

$$\psi_{\boldsymbol{p}}(\boldsymbol{r}, t) = \frac{1}{(2\pi)^{\frac{3}{2}}} \mathrm{e}^{-\mathbf{i}(\omega_{\boldsymbol{p}} t - \boldsymbol{p}\cdot\boldsymbol{r})} \,, \qquad \frac{\boldsymbol{p}^2}{2} = E_{\boldsymbol{p}} = \omega_{\boldsymbol{p}} \,. \tag{A.10}$$

We have identified the energy with the frequency of the wave.[1] In the light of this identification, one would like to employ the Fourier transform in order to find the spectrum, i.e. the energies contained in a signal. Let us look on

$$\tilde{\psi}_{\boldsymbol{p}}(\boldsymbol{r}, \omega) = \int_{-\infty}^{+\infty} \mathrm{e}^{\mathbf{i}\omega t} \psi_{\boldsymbol{p}}(\boldsymbol{r}, t)\, \mathrm{d}t = \frac{\mathrm{e}^{\mathbf{i}\boldsymbol{p}\cdot\boldsymbol{r}}}{(2\pi)^{\frac{3}{2}}} \int_{-\infty}^{+\infty} \mathrm{e}^{\mathbf{i}(\omega-\omega_{\boldsymbol{p}})t}\, \mathrm{d}t = \frac{\mathrm{e}^{\mathbf{i}\boldsymbol{p}\cdot\boldsymbol{r}}}{2\pi} \delta(\omega - \omega_{\boldsymbol{p}}) \,. \tag{A.11}$$

The function $\tilde{\psi}_{\boldsymbol{p}}(\boldsymbol{r}, \omega)$ exactly does the job because it is centred at $\omega_{\boldsymbol{p}}$. One can see that it is the Fourier transform and the above equation explains the reason to choose the proper sign (i.e. the transformation from time to frequency is given by the Fourier transform while coordinates to momenta are transformed by the inverse Fourier transform).

A.2.3 Natural way to define the Fourier transform in physics

The preceding analysis based on the foundations of QM gives natural way how to use the Fourier transform between coordinate space and momentum space and/or between temporal and frequency domain. These are[2]

$$f_1(\boldsymbol{p}) = \mathscr{F}^{-1}\left[f_1(\boldsymbol{r})\right](\boldsymbol{p}) \,, \qquad \tilde{f}_2(\omega) = \mathscr{F}\left[f_2(t)\right](\omega) \,. \tag{A.12}$$

The tilde usually stands for the Fourier transform in time. In this work, the domain is usually specified only by the proper variable. A more precise notation is adopted if there is a possibility of a confusion.

A.3 The incertitude principle in Fourier transformation

The incertitude principle coming from the properties of the Fourier transform will be briefly explained and its implications in signal analysis and QM will be discussed.

In QM, Heisenberg incertitude principle for the measurement of observables is known. This principle lies on the fact that the operators corresponding to these observables do not commute. It is sometimes extended also for the incertitude between time and frequency by a multiplication of the position-momentum inequality by a physical constants with proper dimension.

[1] The conversion factor providing the correct physical dimension is the reduced Planck constant $\hbar$. But its numeric value is equal to 1 in our units.

[2] We can use this this formal definition for both cases, because we have $\hbar = 1$ which allows to set a proper dimension both in the space and also in the time.

A much more general viewpoint is reached using the inequality

$$\Delta_f t \Delta_{\tilde{f}} \omega \geq \frac{1}{16\pi^2}\,, \qquad \Delta_g \xi = \frac{\int\limits_{-\infty}^{\infty} \xi^2 g(\xi)\,\mathrm{d}\xi}{\int\limits_{-\infty}^{\infty} g(\xi)\,\mathrm{d}\xi}\,, \qquad \tilde{f} = \mathscr{F}[f]\,, \tag{A.13}$$

valid for any function $f \in L^2(\mathbb{R})$ (see [23] for a proof and further details). This explains the incertitude between the variation of the signal f and its spectrum. Moreover it has no connection to QM and it is valid for any signal in mathematical sense. Especially, it provides a fundamental limit for the generation of ultra-short light pulses where one needs the spectrum broad enough to form such a pulse. Referring the Heisenberg relations, the position and momentum are Fourier-conjugated, Eq. (A.6), thus the same argument holds also for them.[3]

[3] The derivation in QM usually lies on the commutator algebra of the operators and the incertitude comes from the Schwartz inequality in Hilbert spaces. The proof of (A.13) uses the same inequality. Hence both are the same in their nature despite it may not seem so at a first look.

B. USEFUL MATHEMATICAL FORMULAE

B.1 Basic identities

The harmonic addition theorem [24]

$$\begin{aligned} A\cos(x+\delta_1)+B\cos(x+\delta_2) &= \sqrt{A^2+B^2+2AB\cos(\delta_1-\delta_2)}\cos(x+\delta)\,, \\ \delta &= \operatorname{atan2}\Big(A\sin(\delta_1)+B\sin(\delta_2), A\cos(\delta_1)+B\cos(\delta_2)\Big)\,. \end{aligned} \tag{B.1}$$

The rotation matrices:

$$R_1(\theta)=\begin{pmatrix}1 & 0 & 0\\ 0 & \cos(\theta) & -\sin(\theta)\\ 0 & \sin(\theta) & \cos(\theta)\end{pmatrix}\,,\quad R_2(\theta)=\begin{pmatrix}\cos(\theta) & 0 & -\sin(\theta)\\ 0 & 1 & 0\\ \sin(\theta) & 0 & \cos(\theta)\end{pmatrix}\,,\quad R_3(\theta)=\begin{pmatrix}\cos(\theta) & -\sin(\theta) & 0\\ \sin(\theta) & \cos(\theta) & 0\\ 0 & 0 & 1\end{pmatrix}\,. \tag{B.2}$$

The error function:

$$\operatorname{erf}(x)=\int_0^x \mathrm{e}^{-t^2}\,\mathrm{d}t\,. \tag{B.3}$$

The atan2 function:

$$\operatorname{atan2}(y,x)=\begin{cases}\arctan\left(\frac{y}{x}\right) & \text{if } x>0,\\ \arctan\left(\frac{y}{x}\right)+\pi & \text{if } x<0 \text{ and } y\geq 0,\\ \arctan\left(\frac{y}{x}\right)-\pi & \text{if } x<0 \text{ and } y<0,\\ \frac{\pi}{2} & \text{if } x=0 \text{ and } y>0,\\ -\frac{\pi}{2} & \text{if } x=0 \text{ and } y<0,\\ \text{undefined} & \text{if } x=0 \text{ and } y=0.\end{cases} \tag{B.4}$$

B.2 Fourier transform

The definition of the Fourier transform, Eq. (A.1), implies the following identities

$$\mathscr{F}\left[f(\boldsymbol{x}+\boldsymbol{a})\right](\boldsymbol{\xi})=\mathrm{e}^{-\mathbf{i}\boldsymbol{\xi}\cdot\boldsymbol{a}}\mathscr{F}\left[f(\boldsymbol{x})\right](\boldsymbol{\xi})\,,\qquad \mathscr{F}\left[f(\boldsymbol{x})\right](\boldsymbol{\xi}+\boldsymbol{a})=\mathscr{F}\left[\mathrm{e}^{\mathbf{i}\boldsymbol{a}\cdot\boldsymbol{x}}f(\boldsymbol{x})\right](\boldsymbol{\xi})\,, \tag{B.5}$$

$$\mathscr{F}\left[\partial_{x_i}f(\boldsymbol{x})\right](\boldsymbol{\xi})=-\mathbf{i}\xi_i\mathscr{F}\left[f(\boldsymbol{x})\right](\boldsymbol{\xi})\,,\qquad \partial_{\xi_i}\mathscr{F}\left[f(\boldsymbol{x})\right](\boldsymbol{\xi})=\mathscr{F}\left[(\mathbf{i}x_i)f(\boldsymbol{x})\right](\boldsymbol{\xi})\,, \tag{B.6}$$

$$\mathscr{F}\left[f(c\boldsymbol{x})\right](\boldsymbol{\xi})=\frac{1}{|c|^n}\mathscr{F}\left[f(\boldsymbol{x})\right]\left(\frac{\boldsymbol{\xi}}{c}\right)\,,\qquad \mathscr{F}^{-1}\left[f(\boldsymbol{x})\right](\boldsymbol{\xi})=\mathscr{F}\left[f(\boldsymbol{x})\right](-\boldsymbol{\xi})\,. \tag{B.7}$$

The Fourier transform is often use to analyse real-valued functions, i.e. $f(t)\in\mathbb{R}$, $\forall t\in\mathbb{R}$. Denoting $\tilde{f}(\omega)=\mathscr{F}\left[f(t)\right](\omega)$, one obtains

$$\tilde{f}(\omega)=\tilde{f}^*(-\omega)\,,\forall\omega\in\mathbb{R}\,,\qquad f(t)=\sqrt{\frac{2}{\pi}}\,\mathsf{Re}\left(\int_0^{+\infty}\mathrm{e}^{-\mathbf{i}\omega t}\tilde{f}(\omega)\,\mathrm{d}\omega\right)\,. \tag{B.8}$$

Moreover for a real even function f_1, i.e. $f_1(-t) = f_1(t)$, $\forall t \in \mathbb{R}$, and a real odd function f_2, i.e. $f_2(-t) = -f_2(t)$, $\forall t \in \mathbb{R}$, one has

$$\mathsf{Im}\left(\tilde{f}_1\right) = 0\,, \qquad\qquad \mathsf{Re}\left(\tilde{f}_2\right) = 0\,. \tag{B.9}$$

B.3 The Hankel transform

The Hankel transform, F, of a function f is given by

$$F(\xi) = \int_0^{+\infty} f(x) J_0(\xi x) x \,\mathrm{d}x\,, \tag{B.10}$$

where J_0 is the Bessel function of the first kind of zeroth order. It satisfies the identity ([25], identity 9.1.21):

$$J_0(z) = \frac{1}{\pi}\int_0^{\pi} \mathrm{e}^{\mathbf{i}z\cos(\theta)}\,\mathrm{d}\theta\,. \tag{B.11}$$

B.4 The spherical harmonics

The Spherical harmonics satisfies the orthogonality relations

$$\int_\Omega \left(Y_l^m\right)^* (\Omega_{\boldsymbol{r}})\, Y_{l'}^{m'}(\Omega_{\boldsymbol{r}})\; \mathrm{d}\Omega_{\boldsymbol{r}} = \delta_{ll'}\delta_{mm'}\,. \tag{B.12}$$

The Cartesian coordinates can be written in the spherical coordinates as

$$x = \sqrt{\frac{8\pi}{3}} r \frac{Y_1^1(\Omega_{\boldsymbol{r}}) + Y_1^{-1}(\Omega_{\boldsymbol{r}})}{2}\,, \qquad y = \sqrt{\frac{8\pi}{3}} r \frac{Y_1^1(\Omega_{\boldsymbol{r}}) - Y_1^{-1}(\Omega_{\boldsymbol{r}})}{2\mathbf{i}}\,, \qquad z = \sqrt{\frac{4\pi}{3}} r Y_1^0(\Omega_{\boldsymbol{r}})\,. \tag{B.13}$$

Various expansion in spherical harmonics

$$\mathrm{e}^{\mathbf{i}\boldsymbol{p}\cdot\boldsymbol{r}} = 4\pi \sum_{\substack{l\in\mathbb{N}_0 \\ m\in\{-l,\ldots,l\}}} \mathbf{i}^l j_l(pr) Y_l^m(\Omega_{\boldsymbol{r}}) \left(Y_l^m\right)^*(\Omega_{\boldsymbol{p}})\,, \tag{B.14}$$

j_l is the spherical Bessel function of the first kind.

$$Y_{l_1}^{m_1}(\Omega_{\boldsymbol{r}})\, Y_{l_2}^{m_2}(\Omega_{\boldsymbol{r}}) \;=\; \sum_{\substack{l\in\mathbb{N}_0 \\ m\in\{-l,\ldots,l\}}} (-1)^m \sqrt{\frac{(2l_1+1)(2l_2+1)(2l+1)}{4\pi}} \begin{pmatrix} l_1 & l_2 & l \\ 0 & 0 & 0 \end{pmatrix} \begin{pmatrix} l_1 & l_2 & l \\ m_1 & m_2 & m \end{pmatrix} Y_l^m(\Omega_{\boldsymbol{r}})\,, \tag{B.15}$$

$\begin{pmatrix} j_1 & j_2 & j_3 \\ m_1 & m_2 & m_3 \end{pmatrix}$ is the Wigner 3-j symbol.

B.5 p-representation for Hydrogen-like orbitals

The treatment of the classical Hydrogen atom (i.e. the Hamiltonian $\hat{H}(\boldsymbol{r}) = -\frac{\triangle}{2} - \frac{1}{r}$) is a class-room problem for introductory courses of Quantum Mechanics, see [26] for instant. The eigenfunctions are a superposition of states having the form

$$\langle \boldsymbol{r} | nlm, \varepsilon\rangle = r^{n-1}\mathrm{e}^{-\varepsilon r} Y_l^m(\Omega_{\boldsymbol{r}})\,, \tag{B.16}$$

see the reference for the exact coefficients in the superpositions and the values of ε. This solution is important because it is a good basis for Coulombic problems and a lot of microscopic targets can be described by an expansion in this basis [27].

The task is now to write $|nlm,\varepsilon\rangle$ in the p-representation. The transform is (see Eq. (A.6)):

$$\begin{aligned}\langle \boldsymbol{p}|nlm,\varepsilon\rangle &= \frac{1}{(2\pi)^{\frac{3}{2}}}\int \mathrm{d}^3x\ \mathrm{e}^{-\mathbf{i}\boldsymbol{p}\cdot\boldsymbol{r}}\, r^{n-1}\mathrm{e}^{-r}Y_l^m\left(\Omega_{\boldsymbol{r}}\right) = \\ &= \frac{4\pi}{(2\pi)^{\frac{3}{2}}}\sum_{\substack{l'\in\mathbb{N}_0\\ m'\in\{-l',\dots,l'\}}} \mathbf{i}^{-l'}Y_{l'}^{m'}\left(\Omega_{\boldsymbol{p}}\right)\left(\int_0^{+\infty} j_{l'}(pr)\mathrm{e}^{-r}r^{n+1}\,\mathrm{d}r\right)\left(\int_\Omega \left(Y_{l'}^{m'}\right)^*\left(\Omega_{\boldsymbol{r}}\right)Y_l^m\left(\Omega_{\boldsymbol{r}}\right)\,\mathrm{d}\Omega_{\boldsymbol{r}}\right) = \\ &= \frac{4\pi}{(2\pi)^{\frac{3}{2}}}\sum_{\substack{l'\in\mathbb{N}_0\\ m'\in\{-l',\dots,l'\}}} \mathbf{i}^{-l'}Y_{l'}^{m'}\left(\Omega_{\boldsymbol{p}}\right)I(p,n,l',\varepsilon)\delta_{ll'}\delta_{mm'} = \sqrt{\frac{2}{\pi}}\mathbf{i}^{-l}I(p,n,l,\varepsilon)Y_l^m\left(\Omega_{\boldsymbol{p}}\right)\,. \end{aligned} \tag{B.17}$$

The computation may become cumbersome if there is a lot of terms in the expansion. However, it can be done easily in an analytical software such as Mathematica®, see Appendix F. It also allows to find the integral:

$$I(p,n,l,\varepsilon) = \frac{n!\sin\left((n+1)\arctan\left(\frac{p}{\varepsilon}\right)\right)}{\left(1+\frac{p^2}{\varepsilon^2}\right)^{\frac{n+1}{2}}\varepsilon^{n+1}(n+1)p}\,. \tag{B.18}$$

Finally, one has for the Hydrogen s-state $\langle \boldsymbol{r}|g\rangle = 2\mathrm{e}^{-r}Y_0^0\left(\Omega_{\boldsymbol{r}}\right)$ thus $\langle \boldsymbol{p}|g\rangle = \frac{2\sqrt{2}}{\pi}\frac{1}{(1+p^2)^2}$.

B.6 Matrix elements

Various matrix elements are needed in the SFA model. Their forms are summarized in that section.

B.6.1 Continuum-continuum elements

First, we will introduce plane-waves transition elements. The position operator element is given by

$$\langle \boldsymbol{p}'\,|\,\hat{\boldsymbol{r}}\,|\,\boldsymbol{p}\rangle = \int \mathrm{d}^3x\ \langle \boldsymbol{p}'\,|\,\boldsymbol{r}\rangle\langle \boldsymbol{r}\,|\,\boldsymbol{x}\,|\,\boldsymbol{p}\rangle = \frac{1}{(2\pi)^3}\int \mathrm{d}^3x\ \mathrm{e}^{\mathbf{i}(\boldsymbol{p}-\boldsymbol{p}')\boldsymbol{r}}\boldsymbol{r} = \mathbf{i}\bigtriangledown_{\boldsymbol{p}}\,\delta(\boldsymbol{p}-\boldsymbol{p}')\,, \tag{B.19}$$

where we used the decomposition of unity $1 = \int \mathrm{d}^3r\,|\boldsymbol{r}\rangle\langle\boldsymbol{r}|$. The regularized value of the $\frac{1}{r}$-type element is

$$\left\langle \boldsymbol{p}'\left|\frac{1}{r}\right|\boldsymbol{p}\right\rangle = \frac{1}{(2\pi)^3}\int \mathrm{d}^3x\ \frac{\mathrm{e}^{\mathbf{i}(\boldsymbol{p}'-\boldsymbol{p})\boldsymbol{r}}}{r} = \frac{1}{2\pi^2}\lim_{\varepsilon\to 0}\frac{1}{(\boldsymbol{p}-\boldsymbol{p}')^2+\varepsilon^2}\,. \tag{B.20}$$

B.6.2 Bound-continuum elements

The calculations of ionisations and recombination of microscopic targets (i.e. atoms and molecules) with the ground state, $|g\rangle$, requires to compute so-called *transition-dipole matrix elements* $\boldsymbol{d}(\boldsymbol{p}) = \langle \boldsymbol{p}|\hat{\boldsymbol{r}}|g\rangle$. $|\boldsymbol{p}\rangle$ describes the continuum state defined by its momentum $\boldsymbol{p}$. If a plane wave is considered as the continuum state, the result is given by Eq. (2.5). The exact result for the Hydrogen atom is provided by Eq. (2.6). For a more complex targets, such as Neon in our case, the so-called *Gaussian model* can be used, see [4].

B.6.2.1 Gaussian model

The potential of the target is approximated by a truncated quadratic potential

$$V(\boldsymbol{r}) = \begin{cases}\frac{\alpha^2\boldsymbol{r}^2}{2}-\beta\,, & \text{if } \|\boldsymbol{r}\|\le\sqrt{\frac{2\beta}{\alpha^2}}\\ 0\,, & \text{otherwise}\end{cases}\,. \tag{B.21}$$

The parameters α and β are in the magnitude of the ionisation potential I_P of the target. The parameter β has to be chosen large enough that the ground state $|g\rangle$ can be considered as the eigenstate of the non-truncated potential $V'(\boldsymbol{r}) = \frac{\alpha^2 \boldsymbol{r}^2}{2} - \beta$. It gives

$$\hat{H}' = \left(-\frac{\triangle}{2} + V'(\boldsymbol{r})\right)\psi_g(\boldsymbol{r}) = \left(\frac{3\alpha}{2} - \beta\right)\psi_g(\boldsymbol{r})\,, \qquad \psi_g(\boldsymbol{r}) = \langle \boldsymbol{r}|g\rangle = \left(\frac{\alpha}{\pi}\right)^{\frac{3}{4}} \mathrm{e}^{-\frac{\alpha \boldsymbol{r}^2}{2}}\,. \tag{B.22}$$

The model potential is matched with the target by the value of the ground-state energy, E_g. It imposes $\left(\frac{3\alpha}{2} - \beta\right) = E_g = -I_P$. The required transition-dipole matrix element for the Gaussian model is

$$\boldsymbol{d}_G(\boldsymbol{p}) = \mathbf{i} \bigtriangledown_{\boldsymbol{p}} \psi_g(\boldsymbol{p}) = \mathbf{i}\,(\alpha\pi)^{-\frac{3}{4}}\,\frac{\boldsymbol{p}}{\alpha}\mathrm{e}^{-\frac{\boldsymbol{p}^2}{2\alpha}}\,. \tag{B.23}$$

C. THE FSPA APPLIED ON AN ENVELOPED FIELD

This Appendix discusses the applicability of the FSPA result obtained for an infinite field for real physical fields with slowly varying envelopes. It is particularly used in Eq. (4.10) that may seem not completely clear by a first look because the Fourier transform is formally applied on an already transformed dipole response.

C.1 Relation between the Fourier transform and Fourier series

First of all, we remind the Fourier transform of a functions that is periodic and thus it can be expanded in the Fourier series:

$$f(t) = \sum_{n\in\mathbb{Z}} a_n \mathrm{e}^{\mathbf{i}n\omega_0 t} \qquad \Rightarrow \qquad f(\omega) = \sqrt{2\pi}\sum_{n\in\mathbb{Z}} a_n \delta(\omega - n\omega_0)\,. \tag{C.1}$$

Now, let us consider the function $g = f\chi_{]-\frac{T}{2},\frac{T}{2}[}$ and compute its Fourier transform,

$$\int_{\mathbb{R}} g(t)\mathrm{e}^{\mathbf{i}\omega t}\,\mathrm{d}t = \int_{-\frac{T}{2}}^{\frac{T}{2}} f(t)\mathrm{e}^{\mathbf{i}\omega t}\,\mathrm{d}t\,, \tag{C.2}$$

it is the same expression as for Fourier the coefficients of the periodic extension of g, hence $g(n\omega_0) = a_n$.

C.2 Approximation of an enveloped signal

Let us consider a signal

$$f(t) = E(t)\sin(t)\,, \tag{C.3}$$

where $E(t)$ is an envelope and we assume $E(t) = 0$, $(\forall t \leq 0) \wedge (\forall t \geq T_E)$, T_E is the duration of the signal. For the sake of simplicity, $\omega_0 = 1$ has been chosen.

The adiabatic approximation lies on the fact that the evolution of the envelope is much slower than oscillations of the fundamental signal. The signal can be then well approximated using

$$f(t) \approx f_a(t) = \sum_{k=0}^{N} e_k \chi_{]2k\pi,2(k+1)\pi]}(t)\sin(t)\,, \qquad e_k = E(\tau)\,, \tau \in]2k\pi, 2(k+1)\pi]\,. \tag{C.4}$$

The Fourier transform is then given by

$$\tilde{f}_a(\omega) = \sum_{k=0}^{N} e_k \mathrm{e}^{2\pi\mathbf{i}k\omega} F_1(\omega)\,, \qquad F_1(\omega) = \mathscr{F}\left[\chi_{]0,2\pi]}(t)\sin(t)\right](\omega)\,. \tag{C.5}$$

C.3 Using the result in the ω-domain calculated for an infinite signal

Now, the two previous parts will be connected. Using similar notation as in the previous section, we consider the problem that a fundamental signal $f^{(f)}(t) = E^{(f)}(t)\sin(\omega_f t)$ generates signal $f^{(g)}(t) = E^{(g)}(t)\sin(t)$ (we set $\omega_g = 1$ for simplicity). This is exactly what is done in the FSPA (see section 2.3.4). The result is

calculated in the ω-domain for an infinite fundamental field, i.e. $E(t) = E_0$. However, it can be considered also as a response to a single cycle. Applying also the phase shift, the response is computed in the k-th cycle as

$$\tilde{f}_k^{(g)}(\omega) = e_k^{(g)} \mathrm{e}^{2\pi \mathbf{i} k\omega} F_1(\omega)\,. \tag{C.6}$$

The coefficient $e_k^{(g)}$ is given only by the amplitude of the fundamental field in that interval that is equal to $e_k^{(f)}$. The inverse Fourier transform leads to

$$f_a^{(g)}(t) = \sum_{k=1}^{N} f_k^{(g)}(t) = \sum_{k=1}^{N} e_k^{(g)} \chi_{]2k\pi,2(k+1)\pi]}(t) \sin(t) = E_a^{(g)}(t)\sin(t)\,, \quad E_a^{(g)}(t) = \sum_{k=1}^{N} e_k^{(g)} \chi_{]2k\pi,2(k+1)\pi]}(t)\,. \tag{C.7}$$

We assume that the coefficients of the generated signal, $e_k^{(g)}$, depends on the coefficients of the fundamental signal, $e_k^{(f)}$, as a continuous function. The envelope of the generated signal, $E^{(g)}$, could be then computed as

$$E^{(g)}(t) \approx e^{(g)}(E_f(t))\,. \tag{C.8}$$

This can be transformed back to the ω-domain, the result is

$$\tilde{f}^{(g)}(\omega) = \tilde{E}^{(g)}(\omega) * \mathscr{F}\left[\sin(t)\right](\omega)\,. \tag{C.9}$$

The Fourier transform of sinus only shifts the function and $\tilde{E}^{(g)}(\omega)$ is the desired result.

The theory wad explained for special signal where the fast oscillating part was in the form of sinus. However an arbitrary case is simply reached by the substitution $\sin(t) \to \mathrm{e}^{\mathbf{i}t}$ and inclusion of the phase-shift in the envelope.[1] This is exactly the result Eq. (4.10).

[1] The complex conjugated signal is added to keep it real.

D. VARIOUS DEFINITIONS OF THE PULSE DURATION/SPOT SIZE

Various definitions of the spot-size or the pulse duration are introduced in the following text together with their physical interpretation. For the sake of simplicity, only the coordinate ξ is used. It describes a one-dimensional distribution if not stated otherwise. The definitions are based on the intensity profile $I(\xi)$ and the spot is assumed as symmetric with respect to the $\xi = 0$.

D.1 Effective spot size

The first possibility is *the effective large*

$$\xi_{\text{eff}} = \frac{\int_{-\infty}^{+\infty} I(\xi)\,\mathrm{d}\xi}{I(0)}\,, \tag{D.1}$$

i.e. ξ_{eff} is a side of a rectangle with the same area as the area under $I(\xi)$.

D.2 FWHM

The second and one of the most popular possibilities is ξ in the *Full width at half maximum (FWHM)*, that is defined by

$$I\left(\frac{\xi_{\text{FWHM}}}{2}\right) = \frac{I(0)}{2}. \tag{D.2}$$

This definition describes the position where the intensity decreases to one half of its maximum.[1]

D.3 Area where is $\alpha \cdot 100\%$ of total energy deposed

A next option is to define an area A, where is deposed $\alpha \cdot 100$ % of total energy. It is given by

$$\int_0^{\xi_{E_\alpha}} I(\xi)\mathcal{J}(\xi)\,\mathrm{d}\xi = \alpha \int_0^{+\infty} I(\xi)\,\mathrm{d}\xi\,, \qquad \mathcal{J}(\xi) = \begin{cases} 1 & \text{for Cartesian coordinates} \\ 4\pi\xi & \text{for cylindrical coordinates} \end{cases}. \tag{D.3}$$

The area A is then the interval $]-\xi_{E_\alpha}, \xi_{E_\alpha}[$ in the Cartesian coordinates and a disc with the diameter ξ_{E_α} in the cylindrical coordinates.

D.4 Statistical definition

The last *statistical* definition is *the root mean square*,

$$\xi_{\text{rms}} = \Delta\xi = \sqrt{\frac{\int_{-\infty}^{+\infty} \xi^2 I(\xi)\,\mathrm{d}\xi}{\int_{-\infty}^{+\infty} I(\xi)\,\mathrm{d}\xi}}\,. \tag{D.4}$$

[1] The value $\frac{I(0)}{\mathrm{e}}$ or $\frac{I(0)}{\mathrm{e}^2}$ is sometimes used instead of $\frac{I(0)}{2}$ in that type of definition (especially in the spatial domain).

The intensity is taken, in fact, as a distribution function in that case. This definition looks the less intuitive. However it has very important meaning, because the uncertainty principle, Eq. (A.13), is formulated using this quantity.

Finally, this methodology is also the recommended one by ISO 11146-2:2005 [28].

D.5 Example for Gaussian distribution

Very common distributions for modelling the intensity profile are Gaussian ones. The relations between the previous definitions will be shown for a Cartesian-intensity profile $I(\xi) = I_0 \mathrm{e}^{-\left(\frac{\xi}{\xi_0}\right)^2}$. All quantities, putted in a comparison by ξ_0, are

$$\xi_0 = \frac{\xi_{\mathrm{eff}}}{\sqrt{\pi}} = \frac{\xi_{\mathrm{FWHM}}}{2\sqrt{\ln(2)}} = \frac{\xi_{E_\alpha}}{\mathrm{erf}^{(-1)}\left(\frac{\sqrt{\pi}}{2}\alpha\right)} = \sqrt{2}\xi_{\mathrm{rms}}\,. \tag{D.5}$$

(for example, $\xi_{E_{0.5}} \approx 0.415\xi_0$). It means that all the definitions are proportional in that case, but this is not true for every distribution. Finally, we can find the value of α, for which $\xi_{\mathrm{FWHM}} = \xi_{E_\alpha}$, it is $\alpha = \frac{2}{\sqrt{\pi}}\,\mathrm{erf}\left(2\sqrt{2\ln(2)}\right) \approx 0.76$. It is useful for two things. First, we can see how much energy is inside the region given by ξ_{FWHM}. Second, we have a tool for measuring Gaussian-like spots with a complex inner structure (e.g. interference fringes), where the rigid definition of ξ_{FWHM} has no relevant sense.[2]

[2] The interference pattern can be also destroyed by a convolution. The convolution using a rectangular window,

$$f_a(x) = \frac{1}{2a}\int_{-a}^{a} f(x+t)\,\mathrm{d}t\,, \tag{D.6}$$

is given as an example for the instant. The parameter a is chosen large enough in comparison with the dimension of an interference fringe. This choice also preserves the total area under the curve, i.e. $\int_{-\infty}^{+\infty} f(x)\,\mathrm{d}x = \int_{-\infty}^{+\infty} f_a(x)\,\mathrm{d}x$.

E. GABOR TRANSFORM

E.1 Theory

This transform allows further frequency analysis of a signal. Let us take a signal $f(t)$. The spectrum obtained by the Fourier transform, $|\mathscr{F}[f(t)](\omega)|$, shows the frequencies presented in the signal, however it does not show when they are generated. The idea is to use a narrow window in the t-domain centred around t_0 in order to see frequencies generated in this window. This is the main idea of the so-called *Gabor transform*. We define the Gabor transform as

$$G_f^{(\alpha)}(\omega, t_0) = \mathscr{F}_t\left[w_\alpha(t_0, t) f(t)\right](\omega)\,, \qquad w_\alpha(t_0, t) = \mathrm{e}^{-\left(\frac{t-t_0}{\alpha}\right)^2}. \tag{E.1}$$

The window, w, is specified by the parameter α that defines the narrowness of the window. The frequency-temporal analysis of the signal is then $|G_f^{(\alpha)}(\omega, t)|$.

It also allows for a distinction between two processes leading to similar results when a given frequency is not presented in the spectrum: 1) the given frequency is not generated at all; 2) the frequency component is suppressed by a destructive interference. For the first one, the frequency is not in the Gabor analysis anywhere, where there are some sources in the second case.

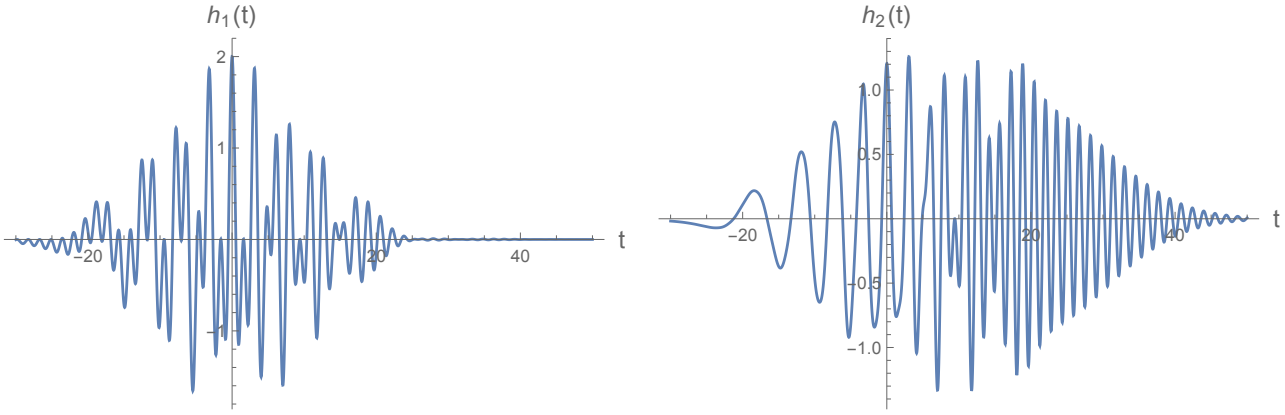

Fig. E.1: The signals h_1 and h_2 in the t-domain. The parameters are $\omega_0 = 2$, $a = 15$, $\tau = 6\pi$ and $\beta = 0.035$.

E.2 Example

The given theory will be illustrated by an example. We choose two signals:

$$h_1(t) = \mathrm{e}^{-\left(\frac{t}{a}\right)^2}\cos(\omega_0 t + \beta t^2) + \mathrm{e}^{-\left(\frac{t}{a}\right)^2}\cos(2\omega_0 t)\,, \tag{E.2}$$

$$h_2(t) = \mathrm{e}^{-\left(\frac{t}{a}\right)^2}\cos(\omega_0 t + \beta t^2) + \mathrm{e}^{-\left(\frac{t-\tau}{a}\right)^2}\cos(2\omega_0 t)\,. \tag{E.3}$$

Both signals are a sum of two pulses with the same Gaussian envelopes but different central frequencies. One of the pulses is chirped while the second is delayed with respect to the first one. The different value of the

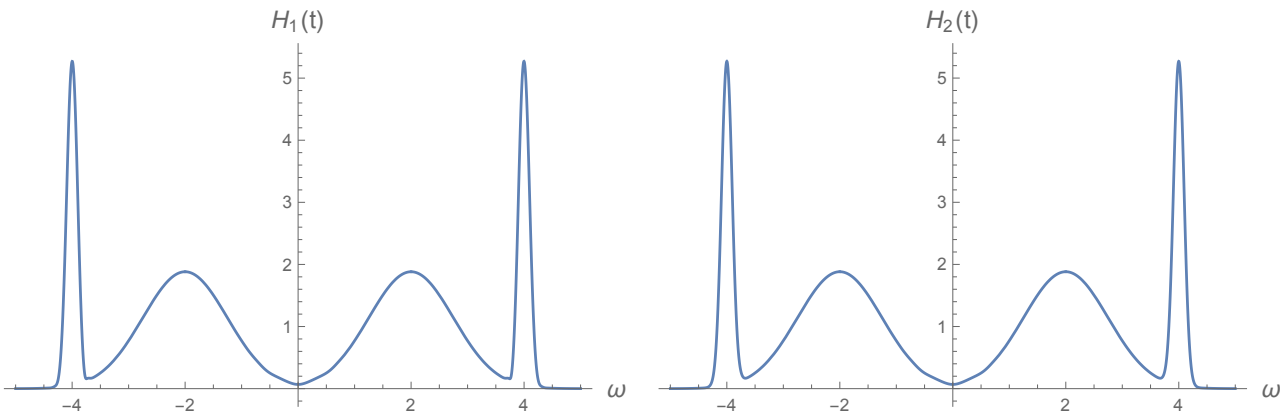

Fig. E.2: The spectra of the signals h_1 and h_2, $H_1 = |\mathscr{F}[h_1]|$ and $H_2 = |\mathscr{F}[h_2]|$.

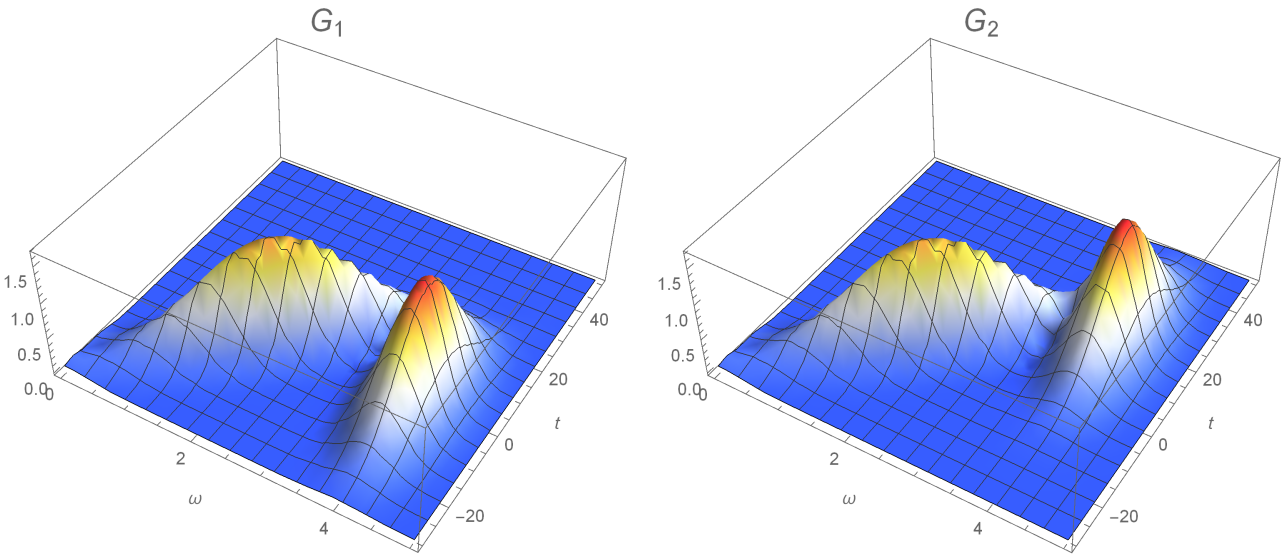

Fig. E.3: The left plot shows $G_1 = |G_{h_1}(\omega, t)|$ and the right one $G_2 = |G_{h_2}(\omega, t)|$. The parameter of the Gabor transform is $\alpha = 5$.

delay is the only difference between these two signals. The signals and their spectra are shown in Figs. E.1 and E.2, respectively. We can see that the spectra are nearly the same. Figure E.3 represents their Gabor transforms. The two signals can be easily distinguished there together with their temporal properties (the chirp and the delay). Moreover, the instantaneous frequency of the chirped signal is also easily recognisable.

E.3 Applications in the study of HHG

This transform is useful to provide an insight into the HHG process. Applying it on the dipole, one can find times when a given frequency is generated. This information provides a more detail physical insight in the generation process. Furthermore, it allows to compare a posteriori a simple model, as it is done in Fig. 3.10.

The same procedure applied to analyse experimental results is often called the *spectrogram*.

F. Mathematica® WORKSHEETS

This works contains attached three interactive Mathematica® worksheets presenting two analytic models and an example of the p-representation:

- `Gaussian.nb` shows the waist of harmonic beam that is supposed to be Gaussian as a function of the jet position with respect to the IR-beam focus.
- `Ellipticity.nb` shows the ellipticity of the field composed from two arbitrary polarised delayed light pulses with a $\sin^2$-envelope. It also shows the intensity profile on the polarisation-gate axis.
- `p-representation.nb` is presenting a way how to find the analytic form of the Hydrogen-like states in p-representation. This procedure has been used to find the p_z-orbital, Eq. (2.21). This orbital is represented in interactive plots. One can scan the known shape of the p_z-orbital in the planes given by $x = \text{const.}$ and $z = \text{const.}$ in the coordinate space. The other scans are the same in the momentum space and the same is repeated for the 2s orbital.